

**DESIGN, CONSTRUCTION, AND USE OF THE
NEUTRON WALL ARRAY IN MEASURING THE
 ${}^8\text{Li}(n,\gamma){}^9\text{Li}$ ASTROPHYSICS REACTION**

By

Philip David Zecher

A DISSERTATION

Submitted to
Michigan State University
in partial fulfillment of the requirements
for the degree of

DOCTOR OF PHILOSOPHY

Department of Physics and Astronomy

November, 1996

Abstract

PART I: A MEASUREMENT OF THE ${}^8\text{Li}(n,\gamma){}^9\text{Li}$ CROSS SECTION AT ASTROPHYSICAL ENERGIES BY REVERSE KINEMATICS.

We have made the first attempt to determine the ${}^8\text{Li}(n,\gamma){}^9\text{Li}$ cross section at astrophysical energies. This reaction competes with the ${}^8\text{Li}(\alpha,n){}^{11}\text{B}$ reaction in the inhomogeneous big bang model, and its reaction rate may affect the primordial abundance of $A > 12$ nuclei. Using a radioactive beam of ${}^9\text{Li}$ and the coulomb dissociation method it is possible to measure the cross section of the inverse reaction ${}^9\text{Li}(\gamma,n){}^8\text{Li}$. The cross section of interest, ${}^8\text{Li}(n,\gamma){}^9\text{Li}$, can then be determined with the detailed balance theorem. With a neutron separation energy of 4 MeV for ${}^9\text{Li}$, nuclear dissociation into $n+{}^8\text{Li}$ competes strongly with coulomb dissociation. Therefore, to separate the nuclear from the coulomb contribution we attempted to measure the cross-section for 6 different targets with Z ranging from 6 to 92.

PART II: A LARGE-AREA, POSITION-SENSITIVE NEUTRON DETECTOR WITH NEUTRON/ γ -RAY DISCRIMINATION CAPABILITIES.

To further study neutron-rich halo nuclei, we have constructed a neutron detector array. The array consists of two separate banks of detectors, each 2×2 meters² and containing 250 liters of liquid scintillator. Each bank is position sensitive to better than 10 cm. For neutron time-of-flight measurements, the time resolution of the detector has been demonstrated to be about 1 ns. By using the scintillator NE-213, we are able distinguish between neutron and γ -ray signals above 1 MeV electron equivalent energy. Although the detector array was constructed for a particular experiment, it has been used in a number of other experiments and will be a part of future experiments.

To my parents.

*I fear from the experiences of the last twenty-five years that morals do not
of necessity advance hand in hand with the sciences.*

Thomas Jefferson



*I fear that machines are ahead of morals by some centuries and when
morals catch up perhaps there'll be no reason for it.*

Harry S. Truman

Table of Contents

Abstract	ii
List of Figures	vii
Part I	1
A Measurement of the ${}^8\text{Li}(n,\gamma){}^9\text{Li}$ Reaction Cross Section at Astrophysical Energies by Reverse Kinematics.	1
1 Introduction	1
1.1 Purpose	1
1.2 Procedure.....	3
1.3 Design	6
2 Experimental Setup.....	7
2.1 Fragment Telescope	10
2.2 Neutron Wall Array.....	17
2.3 Data Acquisition.....	24
3 Data Analysis.....	26
3.1 ${}^8\text{Li}$ Particle Identification.....	27
3.2 Relative Energy Distribution.....	37
3.3 Geometry and Efficiency Considerations.....	39
3.4 Virtual Photon Spectrum.....	42
4 Results and Conclusions.....	44
5 Discussion for Future Experiments	49
Part II	53
A Large-Area, Position-Sensitive Neutron Detector with Neutron/ γ -ray Discrimination Abilities.....	53
6 Motivation	53
6.1 Radioactive Nuclear Beam Advances	53
6.2 The ${}^{11}\text{Li}(\gamma,2n){}^9\text{Li}$ Experiment.....	54
7 Neutron Detection at Intermediate Energies	60
7.1 Scintillation Detection.....	61
7.2 Efficiency	62
7.3 Time-Of-Flight Resolution	65
7.4 Pulse Shape Discrimination.....	68
8 <i>Neutron Wall Array</i> Characteristics	72
8.1 Size, Configuration and Construction.....	72

8.2 Time-Of-Flight Energy Resolution	80
8.3 Position Sensitivity.....	80
8.4 Pulse Shape Discrimination	83
9 Operation.....	87
9.1 Electronics.....	87
9.2 Calibrations	97
9.2.1 Pulse-Height Calibration.....	97
9.2.2 Time Calibrations	100
9.2.3 Cross-Talk.....	101
10 The <i>Neutron Wall Array</i> in Recent Experiments	104
10.1 Measuring the ${}^8\text{Li}(n,\gamma){}^9\text{Li}$ Neutron Capture Cross Section (Zecher, et al.)	105
10.2 Two-Neutron Correlations from Heavy Ion Collisions (Gaff, et al.)	105
10.3 Futher Halo-Nuclei Structure Experiments (Kruse, et al.)	106
Bibliography.....	106

List of Tables

Table 1 - A list of the targets, their thicknesses, and the energy loss for 28.53 MeV/nucleon ${}^9\text{Li}$ particles.....	8
Table 2 - Particle Identification (PID) values and variances (σ_{PID}) for ${}^9\text{Li}$ and for its heavier dissociation products.....	29
Table 3 - The radiative capture cross section calculated from the detailed balance theorem.....	46
Table 4 - Reaction rates for the four theoretical estimates and our data.....	47

List of Figures

- Figure 1 - The primary reaction chain for $A > 12$ nucleosynthesis in a neutron rich region. The solid lines indicate the primary production chain, and the dashed line indicates a destructive chain leading to ${}^4\text{He}$ production. 4
- Figure 2 - Schematic drawing of the coulomb dissociation method..... 5
- Figure 3 - A Schematic drawing showing the arrangement of the equipment. The Si-CsI telescope is 11.5 cm downstream from the target, and the center of the *Neutron Wall Array* is 5 meters downstream from the target. 9
- Figure 4 - An exploded view of the fragment telescope. The beam is incident from the right, and passes through a $300\ \mu\text{m}$ Si strip detector, followed by a $300\ \mu\text{m}$ Si PIN diode detector and stops in a 0.5 cm thick CsI crystal. The CsI crystal is viewed by 4 independent Si PIN diode detectors optically coupled to the backside of the CsI crystal. 11
- Figure 5 Energy spectra from the Si-CsI telescope for a 24.43 MeV/nucleon ${}^9\text{Li}$ calibration beam. The beam had an energy spread of $\frac{1}{2}\%$ 14
- Figure 6 - The particle-identification spectrum for one Pb-target run. This spectrum shows all events in the Si-CsI telescope that were in coincidence with an event in the Neutron Wall Array, without a neutron gate..... 15
- Figure 7 - The particle-identification spectrum for one Pb-target run. This spectrum is the same as for Figure 6, except the signal in the Neutron Wall Array is passed through a neutron filter. 16
- Figure 8 - A low energy pulse-shape-discrimination spectrum for a cell in the Neutron Wall Array. The square root of the product of the integrated charge from the two PMT signals is plotted on the abscissa and the square root of the product of the PSD signals on the ordinate. 20
- Figure 9 - A low energy pulse-shape-discrimination spectrum for a cell in the Neutron Wall Array. The integrated charge of the PMT signal is plotted on the abscissa and PSD signal is plotted on the ordinate. 21
- Figure 10 - A high energy pulse-shape-discrimination spectrum for a cell in the Neutron Wall Array. The attenuated integrated charge of PMT signals is plotted on the abscissa and the PSD signal is plotted on the ordinate..... 22

Figure 11 - Time-Of-Flight (TOF) spectra for the Neutron Wall Array. The upper pane shows the TOF without a neutron PSD filter applied to the data, the lower pane shows the TOF with a neutron PSD filter.	23
Figure 12 - Schematic drawing of the primary trigger logic. The boxes with the dark outlines indicate the electronics set-up for each of the two primary detectors. The modules labeled with fractions are down-scale units; they produce a logic output for every $1/n$ or $1-(1/n)$ logic input signal.....	26
Figure 13 - The PID spectra for a U target. The upper pane shows the target in/target out data; the lower pane shows the difference of the two.	31
Figure 14 - The PID spectra for a Pb target. The upper pane shows the target in/target out data; the lower pane shows the difference of the two.	32
Figure 15 - The PID spectra for a Sn target. The upper pane shows the target in/target out data; the lower pane shows the difference of the two.	33
Figure 16 - The PID spectra for a Cu target. The upper pane shows the target in/target out data; the lower pane shows the difference of the two.	34
Figure 17 - The PID spectra for an Al target. The upper pane shows the target in/target out data; the lower pane shows the difference of the two.	35
Figure 18 - The PID spectra for a C target. The upper pane shows the target in/target out data; the lower pane shows the difference of the two.	36
Figure 19 - Relative energy distributions for the four largest-Z targets. The solid circles represent the target-in data and the open circles represent the target-out data.	38
Figure 20 - Neutron energy distribution for the Pb target. The dashed curve represents the detection efficiency for neutrons in a detector with the approximate characteristics of a cell in the <i>Neutron Wall Array</i>	40
Figure 21 - The detector acceptance and efficiency. The dip at 0.5 MeV is from the asymmetric distribution of active cells in the <i>Neutron Wall Array</i>	41
Figure 22 - The virtual photon number n_{E1} , as calculated by the commercial software package, <i>Mathematica</i>	43
Figure 23 - Radiative capture cross sections for ${}^8\text{Li}(n,\gamma){}^9\text{Li}$. The data points are upper limits measured using the coulomb dissociation method with a U target. All curves are for direct capture to the ground state, except Malaney & Fowler, which is for direct capture to the ground state and first excited state.	48

Figure 24 - The neutron energy distribution for neutrons in coincidence with ${}^7\text{Li}$ fragments from the C and Al targets. This shows the results from a target-in/target-out background subtraction. The narrow energy distribution near the beam velocity is indicative of a peripheral collision.....	52
Figure 25 - Experimental setup to measure the complete kinematics of ${}^{11}\text{Li} \rightarrow {}^9\text{Li} + 2n$ events (Sackett <i>et al.</i> , 1991).	56
Figure 26 - A cutaway diagram of a neutron detector used by Sackett <i>et al.</i> Neutrons are incident from the left. The scintillator is 5 inches in diameter and 3 inches in depth for a volume of 59 in ³ (0.97 liters).....	57
Figure 27 - The two basic contributions to the light output distribution for a monoenergetic neutron beam incident on a detector (from Knoll, ref. 26).	63
Figure 28 - Neutron detection efficiencies. The solid curve represents a simple estimate of the efficiency based on equations 12 and 15. The points represent the results of the simulation code TOTEFF. The triangle data points represent	65
Figure 29 - A schematic drawing of a neutron being detected in a long scintillator cell, perpendicular to the neutron's direction.....	67
Figure 30 - A representation of the scintillation light output as a function of time for different radiations in organic scintillator NE-213.....	70
Figure 31 - The integrated charge in the tail of the pulse for neutron and γ -ray signals, when the total integrated charge for both signals is the same. The FOM for this spectrum is 1.35.....	71
Figure 32 - A drawing of an individual detector cell from the <i>Neutron Wall Array</i> .	74
Figure 33 - A photograph looking lengthwise through a cell. The NSCL's logo was placed at the opposite end of the cell. Only the center image is real, the others are all reflections from the sides of the cell.....	74
Figure 34 - Schematic drawing of the passive voltage divider used on the XP4312/04 PMT.....	75
Figure 35 - A mechanical cutaway drawing of one of the <i>Neutron Wall Array</i>	77
Figure 36 - A schematic drawing of the bubbling procedure for a completed cell. For about 1 hour, dry nitrogen gas is blown through the small Teflon tube that is fed through the reservoir into the cell.....	79
Figure 37 - Top and side view of the cell-mounting bracket.	80

Figure 38 - Neutron and γ -ray TOF spectrum from Ar on Ho at 25 MeV/nucleon. The prompt γ -ray peak from the reaction is an indication of the overall time resolution of the <i>Neutron Wall Array</i>	81
Figure 39 - The relative energy resolution for the <i>Neutron Wall Array</i> . The upper pane shows the resolution as a function of neutron energy, for various flight paths; the lower pane shows the resolution as a function of flight path for various neutron energies.....	82
Figure 40 - A PSD spectrum from a cell in the <i>Neutron Wall Array</i> . The neutrons and γ -rays are from a PuBe source placed a few feet perpendicularly from the center of the cell.	85
Figure 41 - Individual QFAST spectra for various QTOTAL values. The QTOTAL values expressed in terms of equivalent electron energy.....	86
Figure 42 - The figure-of-merit from Figure 41 as a function of the equivalent electron energy.	87
Figure 43 - Basic outline of the processing of the signals from the <i>Neutron Wall Array</i> . Q1 through Q4 represent the charge signals: anode, attenuated anode, PSD, and attenuated PSD.	89
Figure 44 - Pulse shape discrimination methods.	92
Figure 45 - A simple schematic of the method of producng the PSD signal.	93
Figure 46 - The circuit used to produce the PSD pulse. The circuit also acts like an active splitter for the anode pulse. The QFAST output is gain matched to the 50 Ω input of the Lecroy 2249W QDC.....	93
Figure 47 - The master trigger logic. The circled numbers reference timing points whose relationship is shown in.....	95
Figure 48 - Timing diagram for the master trigger logic.....	96
Figure 49 - Sample pulse-height spectra for three different γ -ray sources. The compton edge is used to obtain a calibration of pulse-height to electron equivalent energy. The energies shown are the compton electron energies.	99
Figure 50 - A laser time calibration for a cell in the <i>Neutron Wall Array</i> . The laser pulses are separated by 20 ns.	101
Figure 51 - A typical example of a cross-talk event.....	103

Part I

A Measurement of the ${}^8\text{Li}(n,\gamma){}^9\text{Li}$ Reaction Cross Section at Astrophysical Energies by Reverse Kinematics.

1 Introduction

A persistent question that arose from Edwin Hubble's 1929 discovery of the expanding universe is whether or not the universe contains enough mass to halt its expansion. Given current cosmological theories, if the universe is to halt its expansion (or is closed), one must conclude that most of the matter in the universe is non-baryonic. This conclusion has lead many to search for exotic forms of matter or so called "dark matter." While most of these attempts have turned up empty, some recent enhancements to the standard big bang theory suggest it is possible to close the universe with baryonic matter. An observational test of these new theories might lie in observable quantities of primordial $A > 12$ isotopes. To calculate these quantities, additional reactions must be included in the nucleosynthesis chain. Many of these reactions have never been studied. One reaction in particular, ${}^8\text{Li}(n,\gamma){}^9\text{Li}$, is the subject of our study.

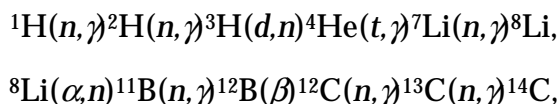
1.1 Purpose

The nucleosynthesis associated with the standard big bang (SBB) model begins with a homogeneous neutron-to-proton ratio, and it constrains the baryon-to-photon ratio, η . (If one believes that the universe is closed, then the constraints on η indicate that most of the matter in the universe must be non-baryonic.¹) A study by Witten² of the quark-gluon plasma to hadron phase

transition in the early universe has brought into question the assumption of a homogeneous neutron-to-proton ratio. In this study, an inhomogeneous density distribution leads to the formation of neutron-rich regions. These regions develop because the neutrons' long scattering length allows them to diffuse more easily than the protons from the higher to the lower-density regions.

Nucleosynthesis in these neutron rich regions would be very different than in the SBB model, and has been modeled by Malaney & Fowler.³ These models can successfully reproduce the observed primordial isotope abundance up to ${}^7\text{Li}$ —where the SBB ends—with a baryon density sufficient to close the universe. As an observational test, Applegate, Hogan, and Scherrer have suggested that nucleosynthesis in these neutron rich regions could lead to observable amounts of $A > 12$ isotopes.⁴

The primary reaction chain leading to $A > 12$ isotopes, is



with a weaker chain passing through the ${}^7\text{Li}(\alpha,\gamma){}^{11}\text{B}$ channel.⁵ A reduction of up to 50 percent in heavy element production could come from two leak reactions, ${}^8\text{Li}(n,\gamma){}^9\text{Li}$ and ${}^8\text{Li}(d,n){}^9\text{Be}$.⁵ Figure 1 shows a schematic view of this reaction sequence.

Malaney and Fowler comment “that the predictions concerning the level of $A > 12$ production remains uncertain due to the presence in the reaction chain of the radioactive isotope ${}^8\text{Li}$ which has a half-life of 0.9 s.”³ Of particular difficulty is the radiative, neutron capture reaction, ${}^8\text{Li}(n,\gamma){}^9\text{Li}$, where both the target and the projectile are radioactive. The theoretical estimates of the ${}^8\text{Li}(n,\gamma){}^9\text{Li}$ cross section vary by more than an order of magnitude. We present the

first attempt at determining this cross section by making a kinematically complete measurement of the inverse reaction ${}^9\text{Li}(\gamma,n){}^8\text{Li}$.

1.2 Procedure

To study the radiative capture process of neutrons, such as ${}^8\text{Li} + n \rightarrow {}^9\text{Li} + \gamma$, one would typically bombard a target of ${}^8\text{Li}$ with neutrons and measure the energy of the emitted γ -ray. Unfortunately, ${}^8\text{Li}$ is unstable and has a half-life of 850 ms, much too short to make a useful target. Although it is possible, with the advent of radioactive beam facilities, to produce a beam of ${}^8\text{Li}$, one would then be required to produce a target of neutrons. Since these two methods are extremely difficult or impossible, a new approach is needed to study this process.

A similar situation exists for the radiative capture of protons with radioactive beams; although proton (H) targets are possible, these targets are very difficult to construct and add complications to the analysis of the reaction. To study such difficult radiative capture reactions, Baur, Bertulani and Rebel⁶ suggested the method of coulomb dissociation. In this process, one measures the photodisintegration cross section of the time reversed reaction ${}^9\text{Li} + \gamma \rightarrow {}^8\text{Li} + n$, by passing the ${}^9\text{Li}$ through the virtual photon field of a large-Z nucleus. This cross section can then be related to the radiative capture cross section by the detailed balance theorem⁷

$$\sigma_{(n,\gamma)}({}^8\text{Li} + n \rightarrow {}^9\text{Li} + \gamma) = \frac{2(2j_{9\text{Li}} + 1)}{(2j_{8\text{Li}} + 1)(2j_n + 1)} \frac{k_\gamma^2}{k^2} \sigma_{(\gamma,n)}({}^9\text{Li} + \gamma \rightarrow {}^8\text{Li} + n), \quad (1)$$

where k is the wave number for the ${}^8\text{Li}+n$ channel, k_γ is the photon wave number, and $j_{9\text{Li}}$, $j_{8\text{Li}}$, and j_n are the appropriate spins. Figure 2 shows a schematic drawing of the coulomb dissociation process.

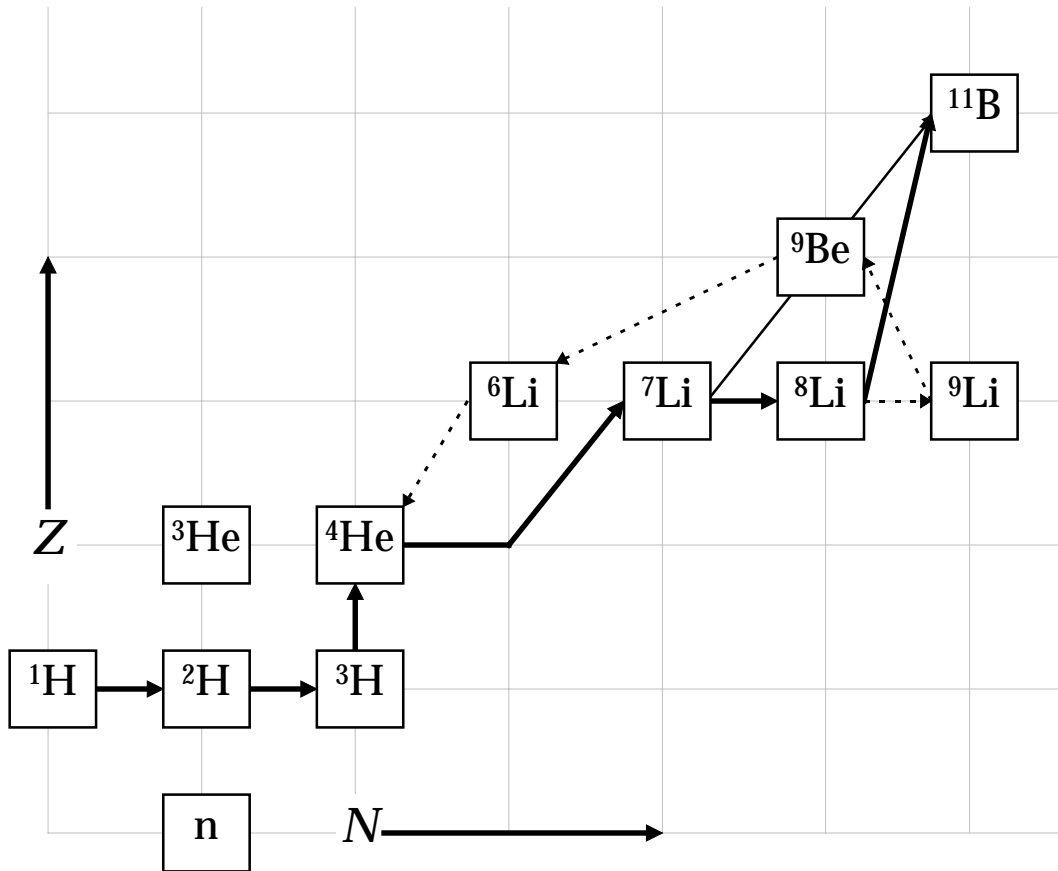


Figure 1 - The primary reaction chain for $A > 12$ nucleosynthesis in a neutron rich region. The solid lines indicate the primary production chain, and the dashed line indicates a destructive chain leading to ${}^4\text{He}$ production.

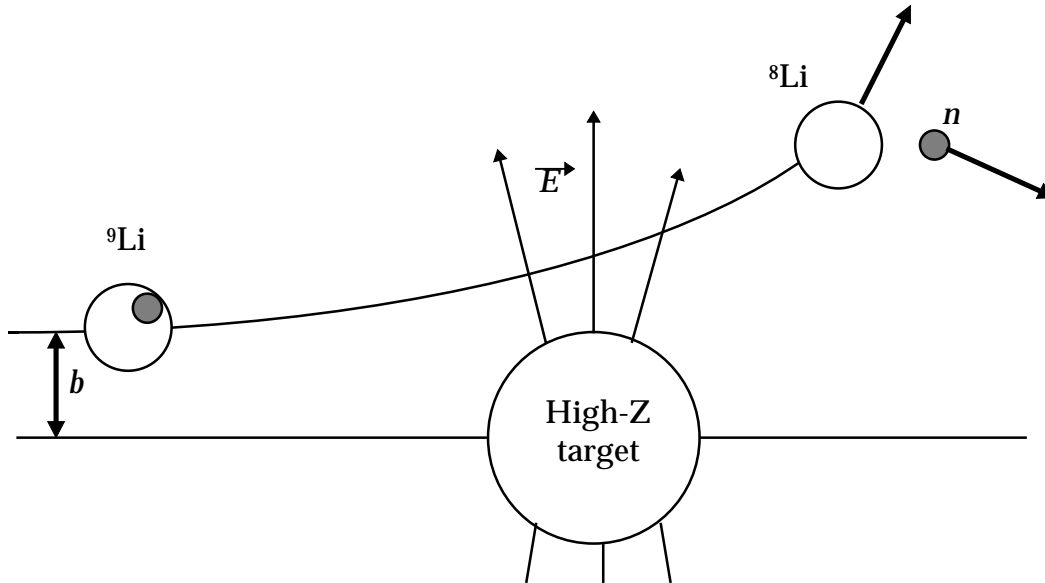


Figure 2 - Schematic drawing of the coulomb dissociation method.

The nuclear coulomb field produces a continuum of virtual photon energies. For each event it is necessary to measure the center of mass decay energy E_d of the reaction products to determine the excitation energy

$$E_x = E_\gamma = E_d + S_n, \quad (2)$$

where S_n , the neutron separation energy, is the binding energy of the least bound neutron in ${}^9\text{Li}$. Once the decay energy is known, the measured differential coulomb excitation cross section $d\sigma/dE_\gamma$ can be related to the photodisintegration cross section $\sigma_{(\gamma,n)}$ by

$$\sigma_{(\gamma,n)} = \frac{E_\gamma}{n_{E1}} \frac{d\sigma}{dE_\gamma}, \quad (3)$$

where n_{E1} is the virtual photon number for the electric dipole transition, which is assumed to dominate and is calculable.^{6,8} The virtual photon spectrum is discussed and calculated in section 3.4 on page 42.

1.3 Design

To measure the coulomb dissociation cross section, we used a ${}^9\text{Li}$ beam of 28.53 MeV/nucleon, incident on a high-Z target. In previous experiments using the coulomb dissociation method, the neutron separation energy of the projectile was sufficiently small that coulomb dissociation was the dominant reaction,^{9,10,11,12} and nuclear effects were ignored. However, the neutron separation energy for ${}^9\text{Li}$ is 4.063 MeV. This reduces the available number of virtual photons with sufficient energy to dissociate ${}^9\text{Li}$, thus reducing the coulomb dissociation cross section. Consequently, we expect the measured ${}^9\text{Li}$ dissociation cross section to contain a non-negligible nuclear component.

Our interest in the coulomb component lead us to attempt to estimate the nuclear component of the cross section. The coulomb dissociation cross section depends, among other things, on Z^2 of the target, and for very low-Z targets we expect the coulomb dissociation to be negligible compared to the nuclear dissociation. The nuclear dissociation should scale with the square of the target-plus- ${}^9\text{Li}$ radius. Therefore, if we normalize the nuclear dissociation to the observed cross section for a low-Z target, we can then scale the nuclear cross section for larger-Z targets where coulomb dissociation is expected to be significant. To measure the deviation from a pure nuclear dissociation in a systematic way, we have measured the dissociation cross section for six different targets with Z ranging from 6 to 92; see Table 1 for a complete list of the targets.

To determine $d\sigma/dE_\gamma$ we used a measurement of cross section versus E_γ . Then we get $\sigma_{(\gamma,n)}$ from equation 3 and the radiative capture cross section from equation 1. For each event E_γ is determined by measuring E_d and using equation 2 with $S_n = 4.063$ MeV. If we make a complete kinematic measurement of the two reaction products, the ${}^8\text{Li}$ fragment and the neutron, in the laboratory frame,

we can deduce E_d as follows: By knowing the masses of the ${}^8\text{Li}$ and neutron, the decay energy can be calculated from the relative velocity \mathbf{V}_{rel} of the ${}^8\text{Li}$ and neutron, $E_d = \frac{1}{2}\mu\mathbf{V}_{rel}^2$, where μ is the reduced mass.¹³ \mathbf{V}_{rel} can be expressed as the difference between the center of mass velocities in the ${}^9\text{Li}$ frame of each product, $\mathbf{V}_{rel} = \mathbf{V}_n - \mathbf{V}_{{}^8\text{Li}}$. In the laboratory frame, $\mathbf{V}_n^{\text{lab}} = \mathbf{V}_n + \mathbf{V}_{{}^9\text{Li}}$ and $\mathbf{V}_{{}^8\text{Li}}^{\text{lab}} = \mathbf{V}_{{}^8\text{Li}} + \mathbf{V}_{{}^9\text{Li}}$. Therefore, the relative velocity of the two products is simply the difference between their laboratory velocities, $\mathbf{V}_{rel} = \mathbf{V}_n^{\text{lab}} - \mathbf{V}_{{}^8\text{Li}}^{\text{lab}}$. The laboratory velocities can be measured if we know the energy and direction from the target of each reaction product.

Since big-bang nucleosynthesis begins when the temperature has dropped to $kT \approx 100$ keV¹, the ${}^8\text{Li}(n,\gamma){}^9\text{Li}$ reaction is of astrophysical interest for only low energy neutrons. Consequently, we are primarily interested in photo-disintegrations with photon energies of approximately 4.0 to 4.5 MeV. With a ${}^9\text{Li}$ beam energy of 28.53 MeV/nucleon, the beam velocity is much greater than the velocities of the decay products; as a result, the decay products are forward focused in the laboratory.

2 Experimental Setup

The measurements were performed at the National Superconducting Cyclotron Laboratory (NSCL). The laboratory's *A1200 Spectrograph* was used to produce an isotopically pure beam of ${}^9\text{Li}$ beam by a fragmentation reaction of 60 MeV/nucleon ${}^{15}\text{Ni}^{4+}$ on a thick ${}^9\text{Be}$ target. The ${}^9\text{Li}$ beam was sent into an experimental hall where, after passing through a target, the charged fragments were detected in a Si-CsI telescope and the neutrons were detected in the *Neutron Wall Array*.

The strong forward focusing of the reaction products mandates that we place both the fragment and neutron detectors at zero degrees with respect to the beam. We can let the telescope act as the beam stop because the beam current for a secondary radioactive beam is typically much less than a primary beam; for our ${}^9\text{Li}$ beam the rate was about 5000 particles per second. Unfortunately, the zero degree telescope provided more material than the target for ${}^9\text{Li}$ in which it could interact. To overcome this difficulty, we must make target-in and target-out measurements and subtract the target-out from the target-in to observe the reactions from the target.

Figure 3 shows a schematic diagram of the experimental setup. Not shown in Figure 3 are the *A1200 Spectrograph* and a small, thin plastic scintillator detector placed after the telescope and subtending the same solid angle as the *Neutron Wall Array*. This plastic scintillator was used to veto protons that made it to the *Neutron Wall Array*.

Table 1 - A list of the targets, their thicknesses, and the energy loss for 28.53 MeV/nucleon ${}^9\text{Li}$ particles.

Target	Thickness (mg/cm ²)	ΔE (MeV)
${}^{238}\text{U}$	339.2	27.27
${}^{208}\text{Pb}$	495.0	40.77
${}^{120}\text{Sn}$	356.8	34.29
${}^{63}\text{Cu}$	282.1	33.12
${}^{27}\text{Al}$	261.9	34.38
${}^{12}\text{C}$	125.2	15.84

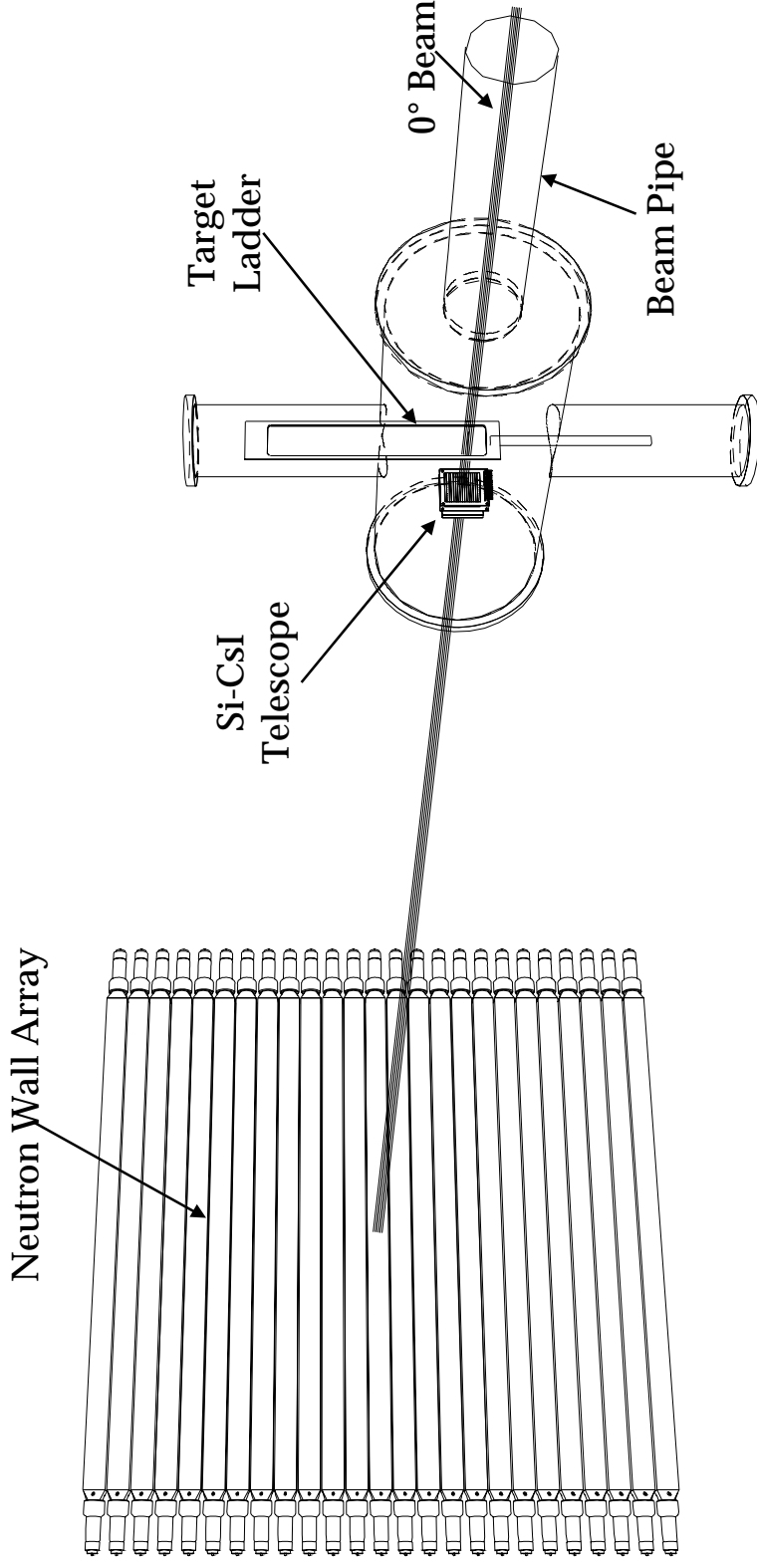


Figure 3 - A Schematic drawing showing the arrangement of the equipment. The Si-CsI telescope is 11.5 cm downstream from the target, and the center of the Neutron Wall Array is 5 meters downstream from the target.

2.1 *Fragment Telescope*

The fragment telescope must perform four functions: distinguish the ${}^8\text{Li}$ fragments from the unreacted ${}^9\text{Li}$ beam particles and other fragments, provide the energy and position information of the fragment and a timing signal for the *Neutron Wall Array*. The particle identification is accomplished by using the technique of a ΔE - E telescope. The energy loss ΔE of a particle passing through a thin absorber is directly proportional to its mass and charge squared and inversely proportional to its energy. When an E (stopping) detector is used to measure the residual energy of the particle after it passes through the ΔE detector, both the mass and charge can be determined for low- Z isotopes.¹⁴

The fragment telescope is composed of three individual detectors: a Si-strip detector for position, ΔE and timing information; a Si PIN diode detector for additional ΔE information; and a CsI stopping detector for residual energy information. Figure 4 shows an exploded view of the fragment telescope. Both of the Si detectors have an active area of $5 \times 5 \text{ cm}^2$. The Si-strip detector was $309 \text{ }\mu\text{m}$ thick and the Si PIN diode was $322 \text{ }\mu\text{m}$ thick. The Si-strip detector has 16 vertical strips on one side and 16 horizontal strips on the other side; when a Li particle passes through the strip detector, most of the charge is collected on a single vertical strip and a single horizontal strip, thereby identifying the location of the event. The CsI detector is a 0.5-cm-thick square crystal, 6 cm on a side; it is viewed by four Si-PIN diode detectors optically coupled to the back side of the crystal. By summing the ΔE signals from the Si detectors and comparing the sum to the energy in the CsI detector, we can identify the different fragment isotopes entering the telescope.

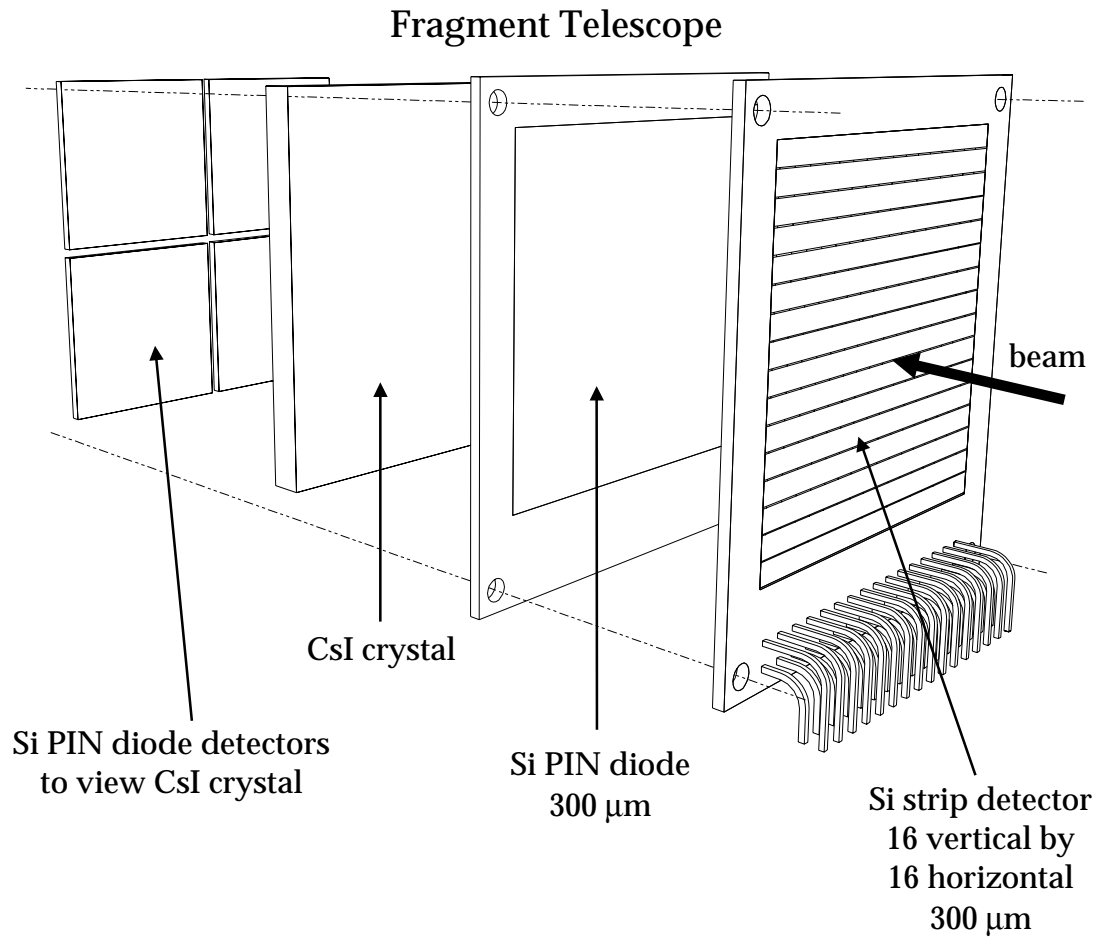


Figure 4 - An exploded view of the fragment telescope. The beam is incident from the right, and passes through a 300 μm Si strip detector, followed by a 300 μm Si PIN diode detector and stops in a 0.5 cm thick CsI crystal. The CsI crystal is viewed by 4 independent Si PIN diode detectors optically coupled to the backside of the CsI crystal.

The Si detectors were calibrated with both an α -particle source and a series of calibration beams. The energy deposited in the Si detectors by the α -particles is independent of the thickness of the Si detectors because the α -particles' range is sufficiently smaller than the thickness. Conversely, each calibration beam passes through the Si detectors, and the energy deposited depends on the thickness of the detectors. By comparing the two calibrations, we were able to determine the thickness of each detector. The calibrated energy signals were summed to produce the ΔE value for the particle identification and then added to the CsI to obtain the fragments' total energy. The lower pane of Figure 5 shows the ΔE spectra for a 24.43 MeV/nucleon ${}^9\text{Li}$ calibration beam. Very narrow momentum slits ($\frac{1}{4}\%$) were used in the *A1200 Spectrograph* to produce this beam; therefore the observed width represents the intrinsic resolution of the Si detectors and not the energy spread of the beam. The measured energy width is about 6% FWHM, or $\sigma_{\Delta E} = 0.61$ MeV. The asymmetric distribution is a natural result of statistical nature of the energy loss processes.

The light output of the CsI crystal, as a function of energy deposited, varies throughout the volume of the crystal. This produces very poor energy resolution when the crystal is viewed as a whole by the PIN diode detectors. To optimize the resolution, we use the pixel information from the Si strip detectors to calibrate 256 discrete regions of the CsI detector. Although the resolution still varies among regions, the mean resolution is about 2.6% FWHM; the best region has a resolution of 1.5% FWHM and no region used in the analysis has a resolution worse than 3.0% FWHM. The upper pane of Figure 5 shows the calibrated energy spectrum from the CsI detector for the 24.43 MeV/nucleon ${}^9\text{Li}$ calibration beam. The measured width of the peak is 2.1% FWHM, or

$\sigma_{\text{CsI}} = 1.71 \text{ MeV}$. The error in the Si detectors and the CsI detector combine to give an error in the total fragment energy of $\sigma_{\text{Total}} = 1.8 \text{ MeV}$.

Figure 6 and Figure 7 show the ΔE - E particle identification spectra for the Pb target runs. Figure 6 shows the telescope events in coincidence with an event in the *Neutron Wall Array*; Figure 7 shows the same data when the *Neutron Wall Array* event was required to be a neutron. In Figure 7 you can see the $1/E$ energy loss curves for ${}^7\text{Li}$, for ${}^8\text{Li}$, and very clearly for ${}^4\text{He}$. The bar running to the left of the ${}^9\text{Li}$ are mainly events that take place in the CsI crystal.

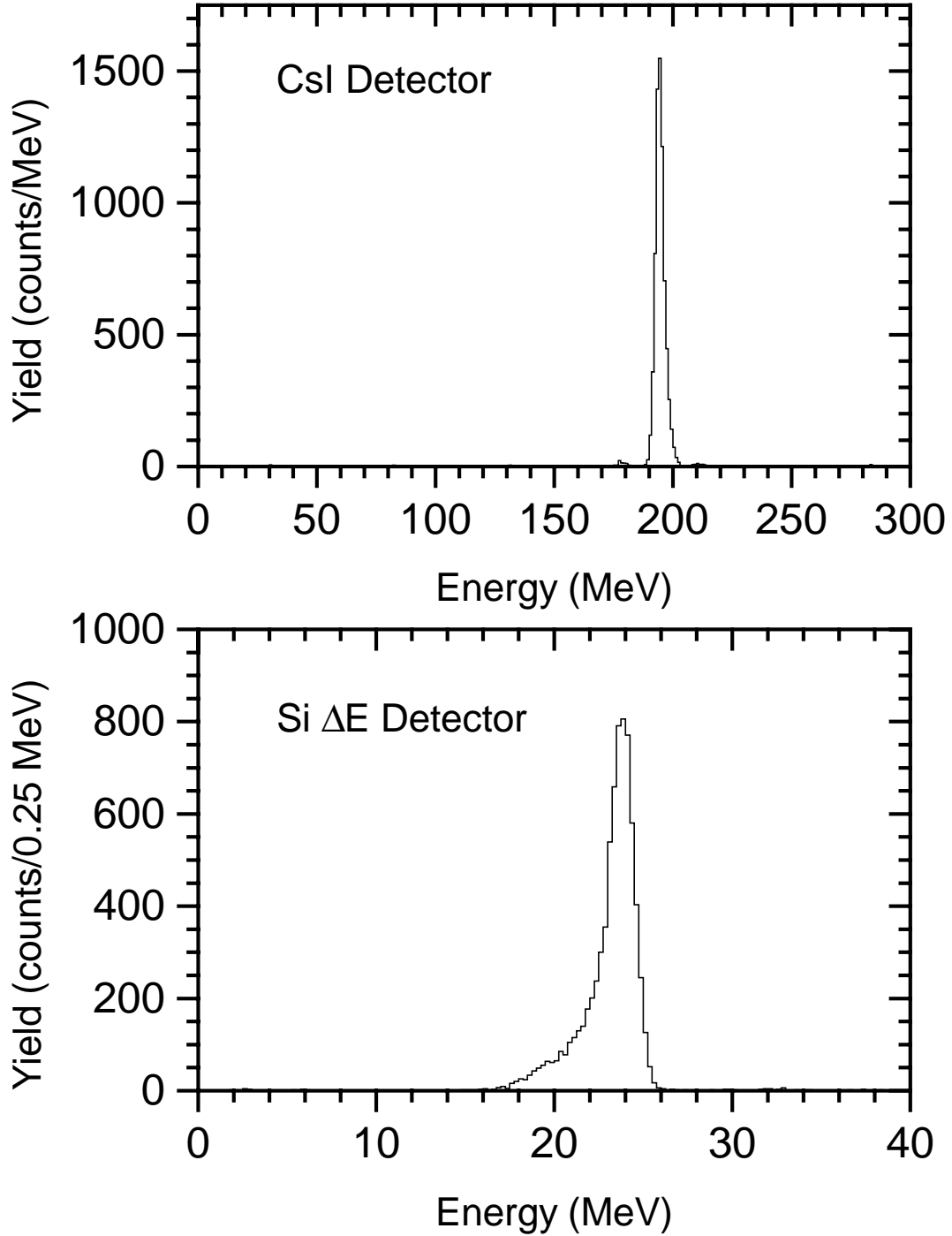


Figure 5 Energy spectra from the Si-CsI telescope for a 24.43 MeV/nucleon ${}^9\text{Li}$ calibration beam. The beam had an energy spread of $\frac{1}{2}$ %.

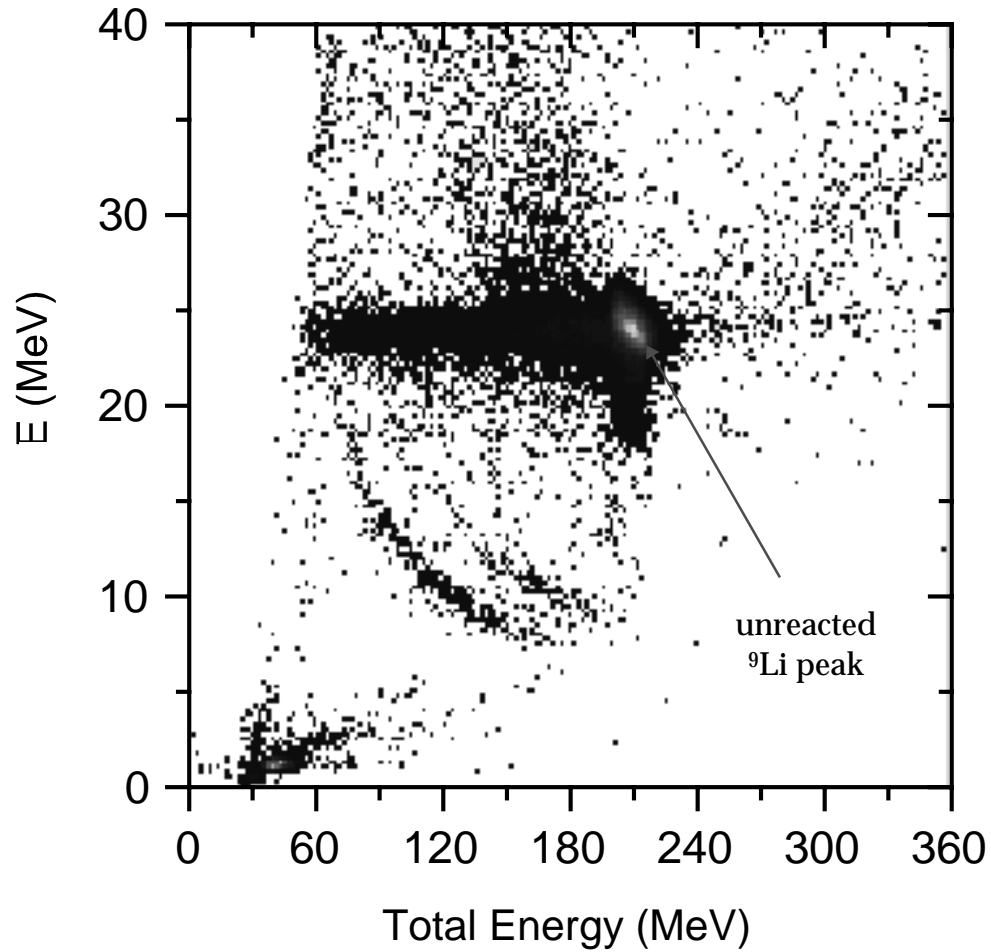


Figure 6 - The particle-identification spectrum for one Pb-target run. This spectrum shows all events in the Si-CsI telescope that were in coincidence with an event in the Neutron Wall Array, without a neutron gate.

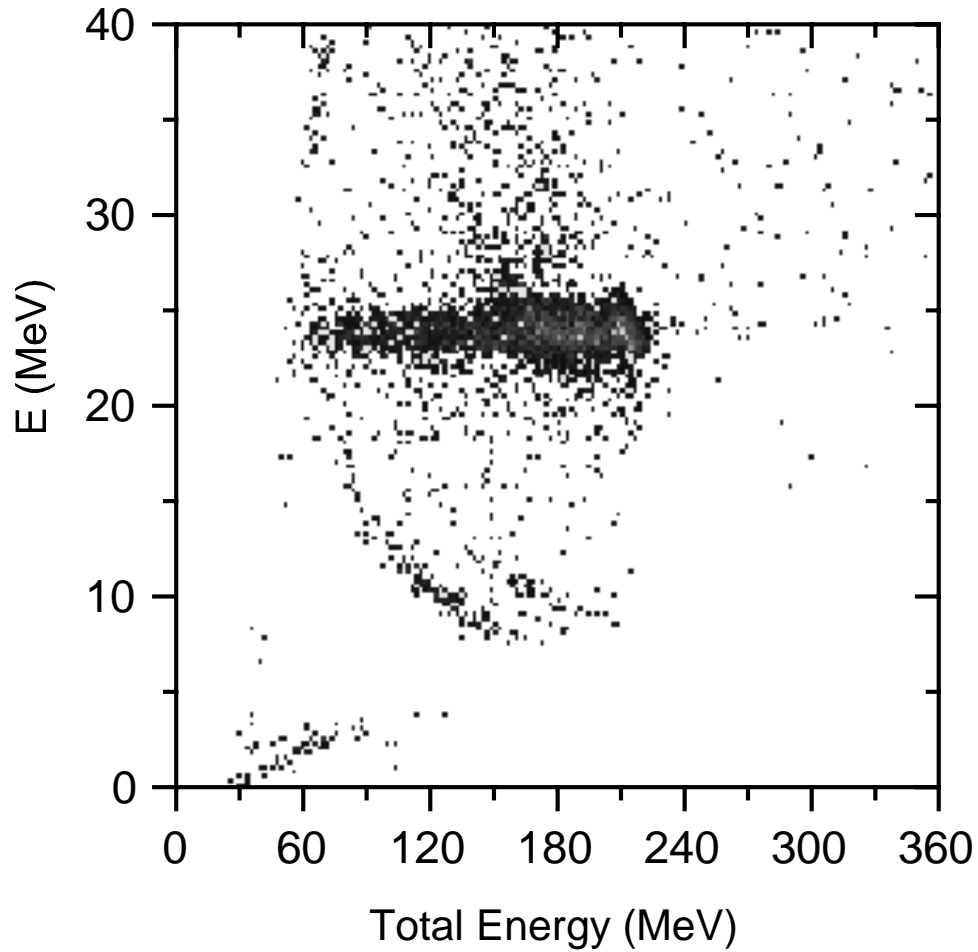


Figure 7 - The particle-identification spectrum for one Pb-target run. This spectrum is the same as for Figure 6, except the signal in the Neutron Wall Array is passed through a neutron filter.

2.2 *Neutron Wall Array*

We detect the neutrons with the NSCL's *Neutron Wall Array*, a large, 2x2 m², position sensitive neutron detector. The *Neutron Wall Array* is discussed in detail in Part II. Although the detector consists of two 2x2 m² planes, only one half of one plane was available at the time of the experiment. Each of the planes consists of 25 2-m-long glass cells filled with a liquid scintillator. Each cell is viewed by two photomultiplier tubes (PMT) optically coupled to the ends of the cell.

The primary mechanism for detecting neutrons with energies of between 5 and 30 MeV is by observing the scintillation caused by a recoiling proton that has elastically scattered a neutron. The proton scintillation process cannot provide unique information about the incident energy of the neutron; therefore, it is necessary to use the time-of-flight (TOF) method to determine the energy of the incident neutron. When using the TOF method, the energy resolution is dependent on two factors: the intrinsic time resolution of the detector and the length of the flight path. The flight path was 5.07 meters from the target to the center of the array; this value was chosen as a balance between the acceptable solid angle subtended by the detector and the required energy resolution.

The *Neutron Wall Array* has a scintillator volume of about 500 liters, spread through two thin detecting planes with a very large surface area. This configuration makes it very sensitive to cosmic-ray and γ -ray backgrounds, since cosmic-ray efficiency is primarily dependant on the the detector's surface area. To eliminate this background, the *Neutron Wall Array* was built using the liquid scintillator NE-213, which has the well known property of pulse-shape-discrimination (PSD), allowing us to distinguish between neutron events and γ -ray/cosmic-ray background events.

There are a number of different methods of performing this pulse-shape-discrimination, although most are not suitable to a detector as large as the *Neutron Wall Array*. To overcome the difficulties of these existing methods, we developed a new method which is discussed in Part 3. Our method produces a signal called QFAST, which is proportional to the charge in the early portion of a pulse from a PMT. If QTOTAL is the total integrated charge from a PMT, then for an equal amount QTOTAL from a γ -ray and a neutron, the value of QFAST is different for γ -rays and neutrons.

The scintillation light inside a cell is attenuated as it makes its way to each PMT, so that the luminosity measured at the PMT is $L_{PMT} = L_0 e^{-x/\lambda}$, where L_0 is the initial luminosity, x is the distance to the PMT, and λ is the attenuation length. If the other PMT is a distance l (the length of the cell) away from the first PMT, then its measured luminosity is $L_{PMT2} = L_0 e^{-(l-x)/\lambda}$. If we take the square root of the product of these two measured luminosities,

$$L_{measured} = \sqrt{L_{PMT} L_{PMT2}} = L_0 e^{-l/\lambda},$$

then $L_{measured}$ is independent of the position of the event within the cell. We use the $L_{measured}$ value to set a lower limit threshold in software. The limit we have used is 2 MeV γ -ray equivalent energy, or a 5.0-5.5 MeV neutron energy.

Figure 8, Figure 9, and Figure 10 show samples of the PSD spectra. Figure 8 shows the PSD for the square root of the product of the total charge signals and the QFAST signals. No software threshold has been applied to these data; as can be seen, we have very good pulse shape discrimination for low energy neutrons. Unfortunately, as the neutron energies increase, the PMT closer to the event saturates, and the square root of the product method fails. For these events, we use a spectrum such as that in Figure 9 to determine if the event was a neutron.

In Figure 9, we compare only one PMT signal to its corresponding QFAST signal. If the pulse is large enough to saturate both PMT signals, then we use an attenuated PMT signal; this is shown in Figure 10.

The upper pane of Figure 11 shows the TOF spectrum for one cell in the neutron wall, including all γ -ray and cosmic-ray events. The TOF is measured between the Si-Strip detector and the mean-time of two PMTs on a cell in the *Neutron Wall Array*. It is not possible to know an exact zero for the clock from the electronics; therefore, we use the observed prompt γ -ray peak in the TOF spectrum to determine the time-equals-zero channel. The prompt γ -ray peak is produced when the *Neutron Wall Array* detects the γ -rays from nuclear interactions in the target and telescope. Since their time is independent of their energy, and we know the flight path, we are able to determine when the clock started. The inset to the upper pane of Figure 11 shows the γ -ray peak in more detail. The width of this peak is a measure of the intrinsic time resolution of the neutron detector and allows us to know the neutron energy resolution. For a 24-MeV neutron, over a 5-meter flight path, the FWHM energy resolution will be 3%. The lower pane of Figure 11 shows the neutron only TOF spectrum for the cells used during the experiment.

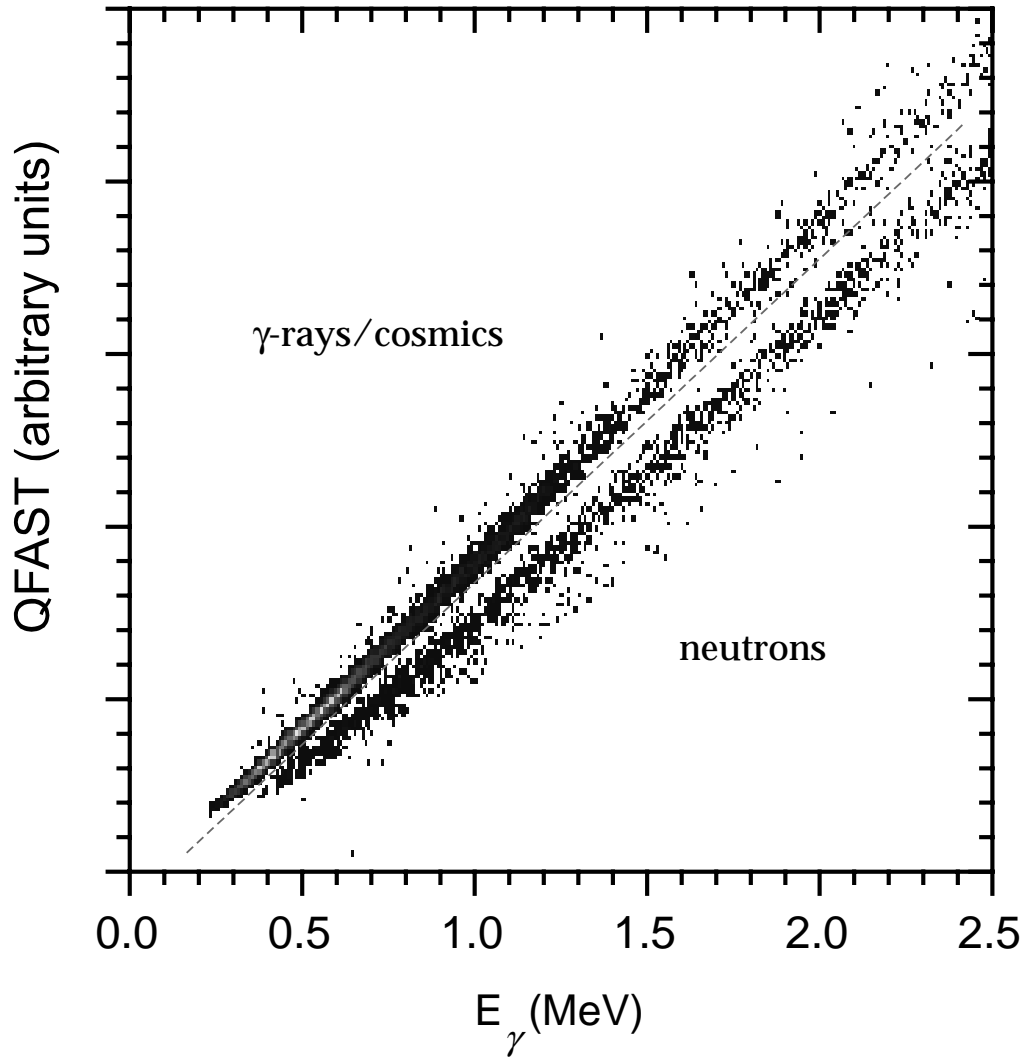


Figure 8 - A low energy pulse-shape-discrimination spectrum for a cell in the Neutron Wall Array. The square root of the product of the integrated charge from the two PMT signals is plotted on the abscissa and the square root of the product of the PSD signals on the ordinate.

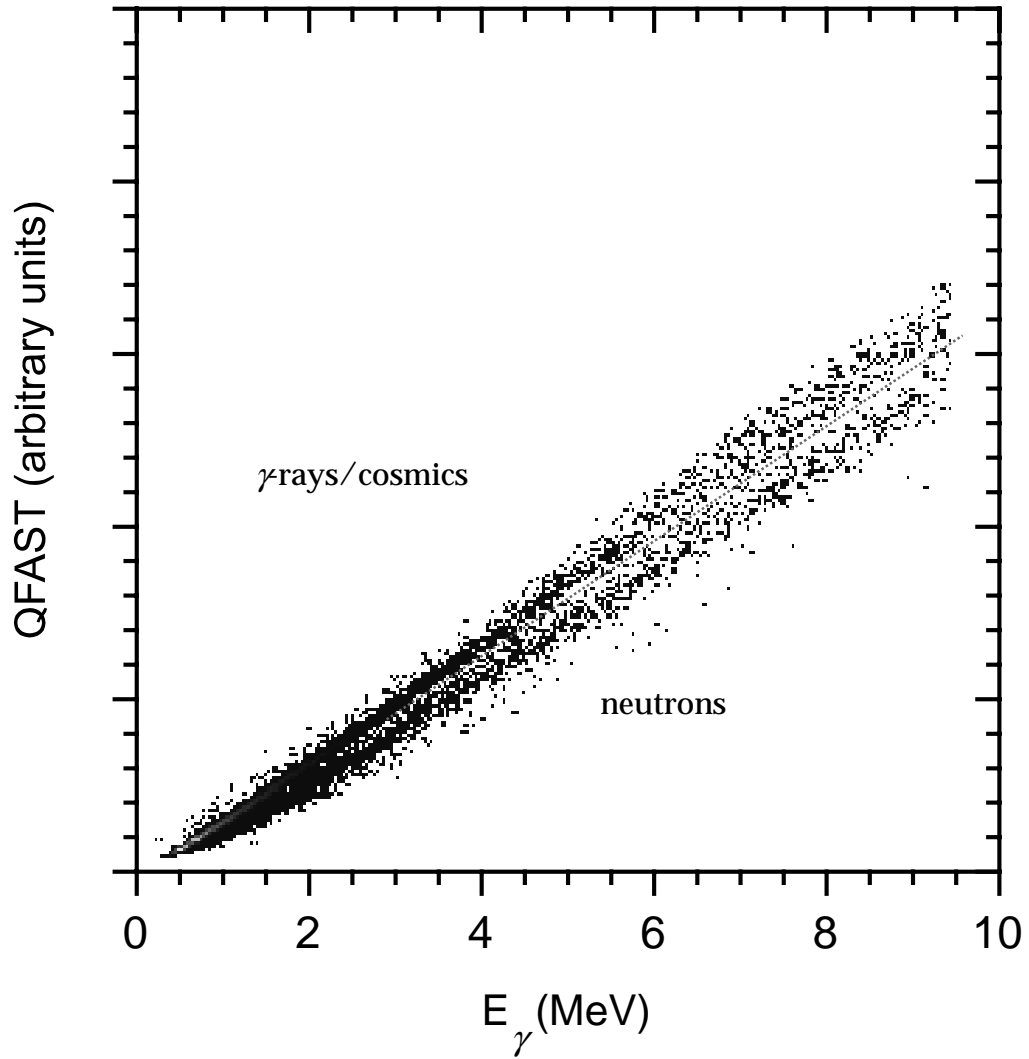


Figure 9 - A low energy pulse-shape-discrimination spectrum for a cell in the Neutron Wall Array. The integrated charge of the PMT signal is plotted on the abscissa and PSD signal is plotted on the ordinate.

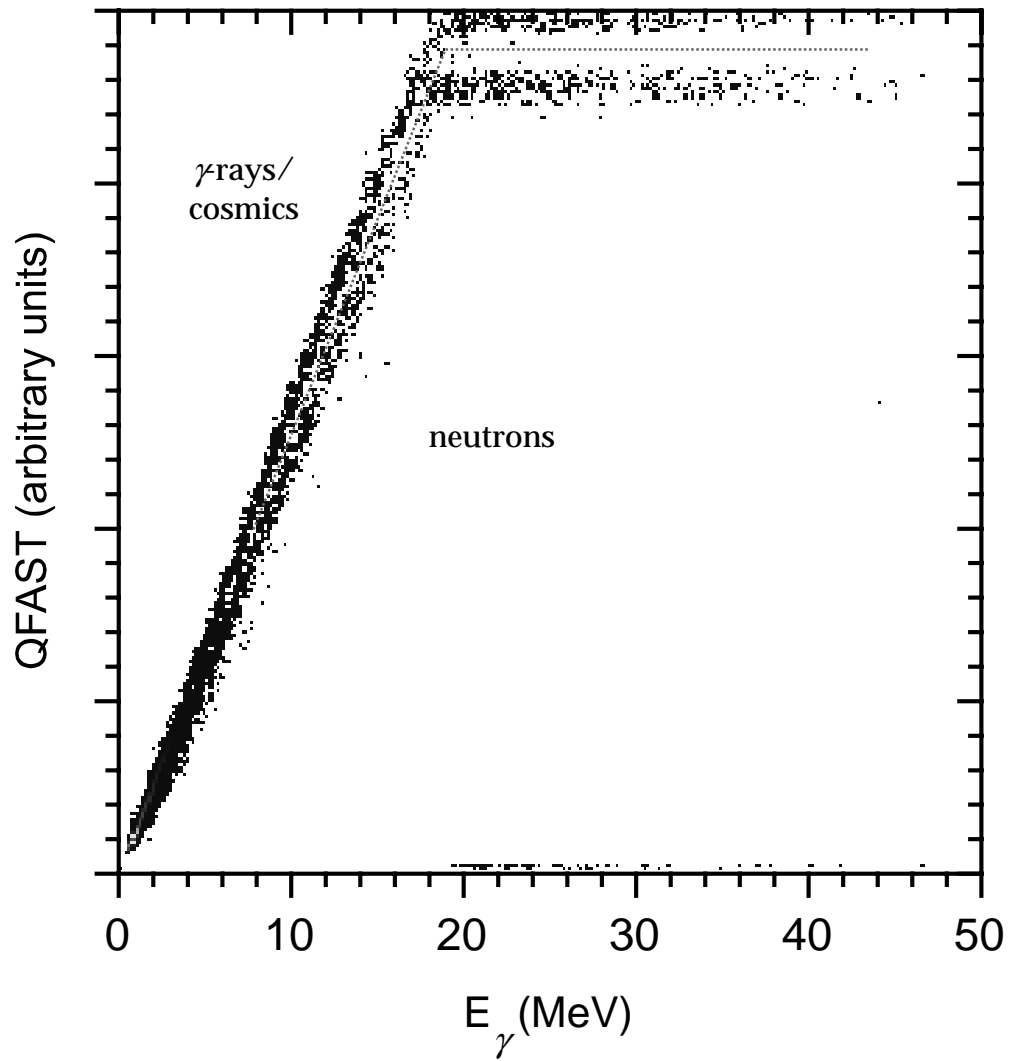


Figure 10 - A high energy pulse-shape-discrimination spectrum for a cell in the Neutron Wall Array. The attenuated integrated charge of PMT signals is plotted on the abscissa and the PSD signal is plotted on the ordinate.

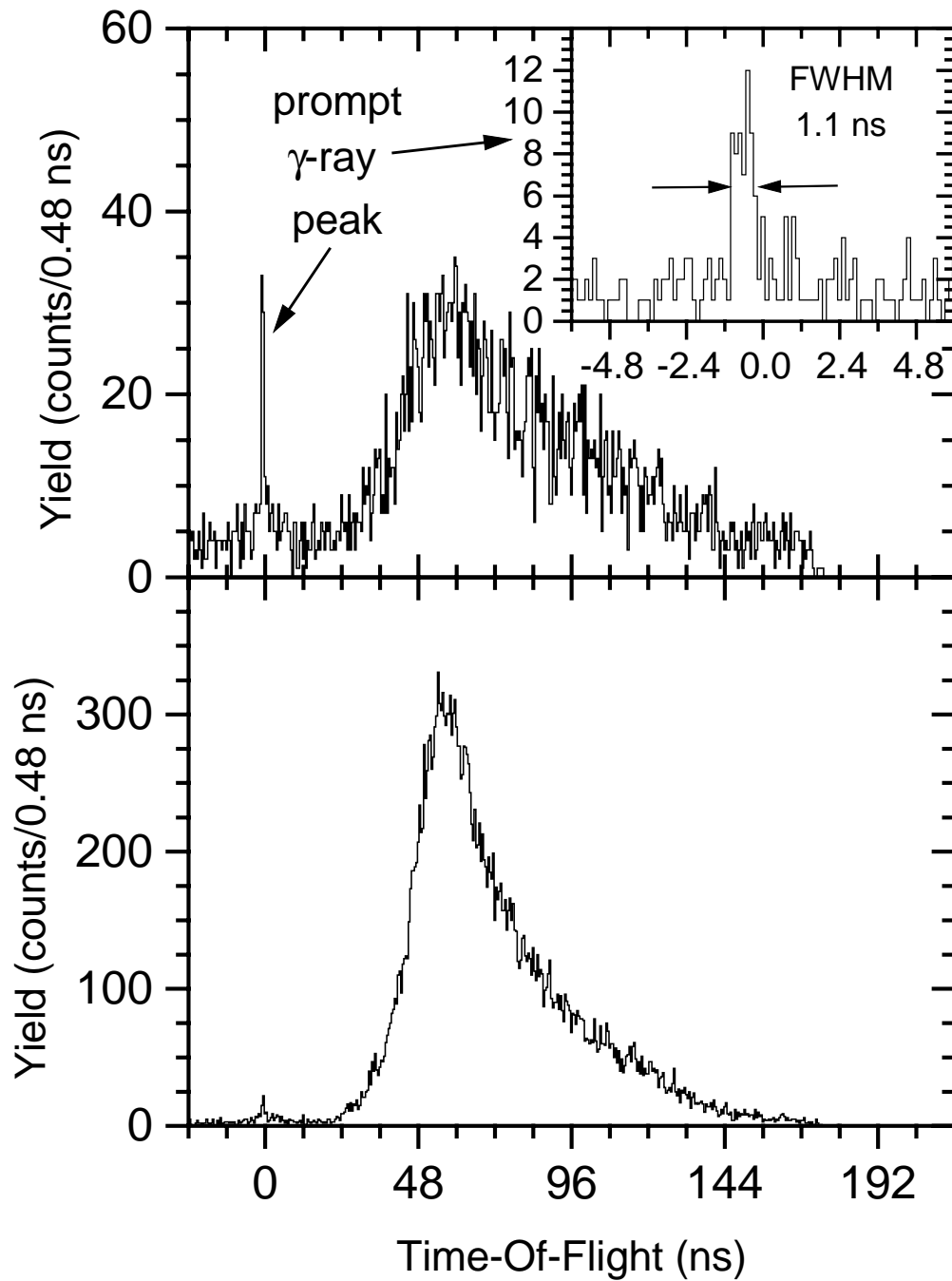


Figure 11 - Time-Of-Flight (TOF) spectra for the Neutron Wall Array. The upper pane shows the TOF without a neutron PSD filter applied to the data, the lower pane shows the TOF with a neutron PSD filter.

2.3 Data Acquisition

There are three primary sub-systems in the data acquisition system. The first sub-system acquires data from the *Neutron Wall Array*, and is described in more detail in Part II. The next sub-system acquires data from the Si-CsI telescope, and the final sub-system contains the master-trigger logic for controlling the data acquisition computer.

The *Neutron Wall Array* acquisition system provides direct and attenuated pulse-height information and a QFAST signal for each of the PMTs in the array. In order to make the time-of-flight (TOF) measurement, the acquisition system also provides a time value for each PMT, measured against some common stop signal. For this experiment, the common stop signal comes from the Si-CsI telescope.

The stop signal from the Si-CsI telescope comes from a logical OR of the timing signals from the 16 vertical strips of the Si-strip detector. Each of the vertical strips is connected to a pre-amplifier that provides a slow signal proportional to the energy deposited in the strip, and a fast timing signal. Only the energy signal is used for the horizontal strips. A 16-channel programmable constant-fraction-discriminator is used to produce a logic signal from each of the 16 fast signals. Since the TOF stop signal passed to the *Neutron Wall Array* is created by a logical OR of 16 different channels of electronics, the TOF must be corrected for the time variations between the channels. When a signal is produced in a strip by a charged particle passing through the strip, the neighboring strips also create small signals. The signals in the neighboring strips are about two orders of magnitude less than in the strip that was hit. These smaller signals will not pass the threshold of the constant fraction discriminator and will not contribute to the logical OR signal. Therefore, we calibrate the

Neutron Wall Array TOF with each of the 16 vertical strips, and for each event we use the calibration from the strip with the maximum pulse height to calculate the TOF.

A logical AND is formed from the logical OR signal of the Si-strips and the computer-not-busy signal; this AND signal is then used to create the gate signal for ORTEC AD811, peak-sensing, analog-to-digital-converters (ADC) that measure the pulse-height signals from the all the strips, vertical and horizontal. This same gate signal is also used for AD811s that read out the Si PIN diode detector and the four CsI light detectors.

For this experiment, a valid event is one where signals from the *Neutron Wall Array* and the Si-CsI telescope fall within some specified coincidence period. Registering this coincidence and instructing the computer to read out the data from the appropriate modules is the primary purpose of the master-trigger subsystem, shown schematically in Figure 12. The coincidence period is defined as the 250 nanoseconds following an event in the Si-CsI telescope; a time sufficiently large to allow the lowest energy (slowest) neutrons that we can detect to make it to the *Neutron Wall Array*.

To calculate the dissociation cross section, we must know the number of ${}^9\text{Li}$ particles incident on the target. We determine the number of incident particles by counting the number of ${}^9\text{Li}$'s that enter the telescope, since the vast majority of the ${}^9\text{Li}$ particles do not interact in the target and pass into the telescope. Counting all of these events would create an unacceptable dead-time in the electronics, and many coincidence events would be missed while the computer is busy counting the beam particles. Therefore, we only record 1/200th of events in the Si-CsI telescope that are not in coincidence with an event

in the *Neutron Wall Array*. To provide information during analysis on the performance of the *Neutron Wall Array*, we also record 1/1000 of the *Neutron Wall Array* events that are not in coincidence with an event in the Si-CsI telescope.

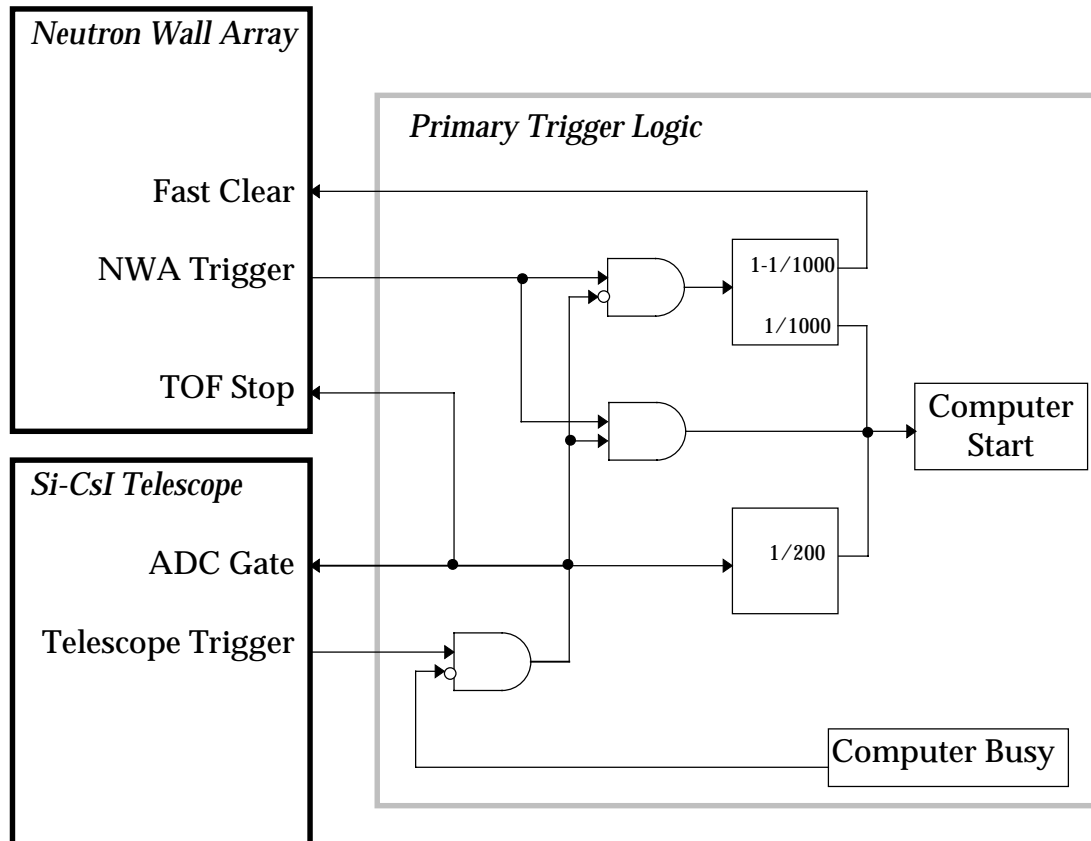


Figure 12 - Schematic drawing of the primary trigger logic. The boxes with the dark outlines indicate the electronics set-up for each of the two primary detectors. The modules labeled with fractions are down-scale units; they produce a logic output for every $1/n$ or $1-(1/n)$ logic input signal.

3 Data Analysis

The primary difficulty in the data analysis is the identification of the ${}^8\text{Li}$ particles in the telescope. The procedure we used is discussed in section 3.1. Once the ${}^8\text{Li}$ -neutron coincidences are identified in the data, the ${}^8\text{Li}+n$ system's

decay energy is calculated from the measured kinematics (see section 3.2). Then decay energy spectra for each target are folded with a decay energy dependent detection efficiency to obtain a measured dissociation yield. Using this measured dissociation yield and the detailed balance theorem, we determine the ${}^8\text{Li}(n,\gamma){}^9\text{Li}$ radiative capture cross section.

3.1 ${}^8\text{Li}$ Particle Identification

To calculate the dissociation cross section for ${}^9\text{Li}$, we must determine if the particle entering the telescope was ${}^8\text{Li}$. Although the coincidence requirement with a neutron in the *Neutron Wall Array* eliminates all but a few of the ${}^9\text{Li}$ from the telescope spectrum, it is necessary to distinguish the ${}^8\text{Li}$ from ${}^7\text{Li}$, ${}^4\text{He}$, and reaction products produced in the telescope itself.

The strong forward focusing of the reaction products, when the decay energy is low, requires us to place the telescope detector at 0° with respect to the beam. Unfortunately, the unreacted ${}^9\text{Li}$'s entering the telescope have much more mass to interact with than they had in the target. If an interaction in the telescope produces a neutron that is detected, it is difficult to determine if the event took place in the target or the telescope. To remove this telescope background, we measure the cross section with the target and without the target, the so called target-in and target-out measurements, and subtract the target-out cross section from the target-in cross section. To avoid creating systematic errors between the target-in and target-out measurements, the beam energy for the target-out measurement was reduced by an amount equivalent to the energy loss in the targets.

Although it is possible to identify the ${}^8\text{Li}$ isotopes from the ΔE - E spectrum shown in Figure 7, it is nevertheless difficult. To make the task easier, we take

advantage of the fact that light ions, such as He and Li, obey the empirical power-law formula $R = aE^\alpha$, where R is the range of a particle with an energy E and a and α are constants.¹⁵ Using this power-law relationship, we derive a particle-identification (PID) function that is directly proportional to the mass and charge squared (AZ^2). The PID function can be expressed as

$$\text{PID} = E^\alpha - (E - \Delta E)^\alpha \quad (4)$$

where E is the total energy of the fragment entering the Si-CsI telescope, ΔE is the energy loss in the Si detectors, and α is selected to provide, for a given fragment species, a constant value of PID over the energy range of interest. For our range of energy, values of α from 1.75 to 1.80 are acceptable. We used $\alpha = 1.78$.

The width of the PID peak for a given isotope can be found by using the two individual detector resolutions. For any function of two parameters, $x = f(u, v)$, where the variance of each parameter is known, the variance of x is given by

$$\sigma_x^2 = \sigma_u^2 \left(\frac{\partial x}{\partial u} \right)^2 + \sigma_v^2 \left(\frac{\partial x}{\partial v} \right)^2 \quad (5)$$

if u and v are uncorrelated.¹⁶ If the variances of the Si and CsI detectors correlated, the error in one must influence the error in the other. Since the electronics are sufficiently separated, there are no electronic effects to cause a correlation. Although there is energy straggling in the Si detector, which could affect the energy deposited in the Si and CsI in a correlated fashion, the expected energy straggling is about 0.3 MeV, less than half of the measured telescope resolution of 0.61 MeV. Therefore we will assume that the errors in the CsI and Si- ΔE signals represent the intrinsic resolutions of the detectors and thus $\sigma_{E_{\text{CsI}}}$

and $\sigma_{\Delta E}$ are uncorrelated. Using equations 4 and 5 and $E = E_{\text{Csl}} + \Delta E$, the variance in PID is given by

$$\sigma_{\text{PID}}^2 = \alpha^2 \left[\sigma_{E_{\text{Csl}}}^2 (E^{\alpha-1} - E_{E_{\text{Csl}}}^{\alpha-1})^2 + \sigma_{\Delta E}^2 E^{2(\alpha-1)} \right]. \quad (6)$$

Using equations 4 and 6, we get the following values of PID, and σ_{PID} for ${}^9\text{Li}$ and for its heavier dissociation products.

Table 2 - Particle Identification (PID) values and variances (σ_{PID}) for ${}^9\text{Li}$ and for its heavier dissociation products.

Isotope	E_{total} (MeV)	E_{Csl} (MeV)	ΔE (MeV)	PID $\div 20$	σ_{PID} $\div 20$
${}^9\text{Li}$	210	185.6	24.4	134.2	4.0
${}^8\text{Li}$	185	160.4	24.6	121.6	3.6
${}^7\text{Li}$	165	140.8	24.2	108.9	3.3
${}^6\text{Li}$	140	115.6	24.4	95.4	2.9
${}^8\text{He}$	185	174.1	10.9	55.7	1.6
${}^6\text{He}$	140	129.2	10.8	44.2	1.3
${}^4\text{He}$	95	84.3	10.7	31.7	0.9

The upper pane of Figure 13 shows the PID spectrum for the uranium target and for the target-out (telescope contribution); the lower pane shows the difference between the two spectra. The following five figures show the same information for each of the other five targets: Pb, Sn, Cu, Al, and C. The most prominent features in each of these spectra are the ${}^7\text{Li}$ and ${}^4\text{He}$ peaks.

The ${}^8\text{Li}$ yield in these figures is very small, but it can be observed in the four heaviest targets. The ${}^7\text{Li}$ peak in each spectrum is clear enough that we are able to fit it to a gaussian distribution. Allowing all the parameters to vary, we obtain good agreement between the centroid and width values in Table 2 and the fit results. The fits to the ${}^8\text{Li}$ peaks shown are the result of fitting the ${}^7\text{Li}$ and ${}^8\text{Li}$ region of data to a double gaussian distribution, holding fixed the centroids and widths. (The ${}^4\text{He}$ peaks are half way between the expected ${}^4\text{He}$ and ${}^6\text{He}$ peaks

from Table 2; this is attributed to the non-linear response, and projectile-Z dependence of the CsI light output.)

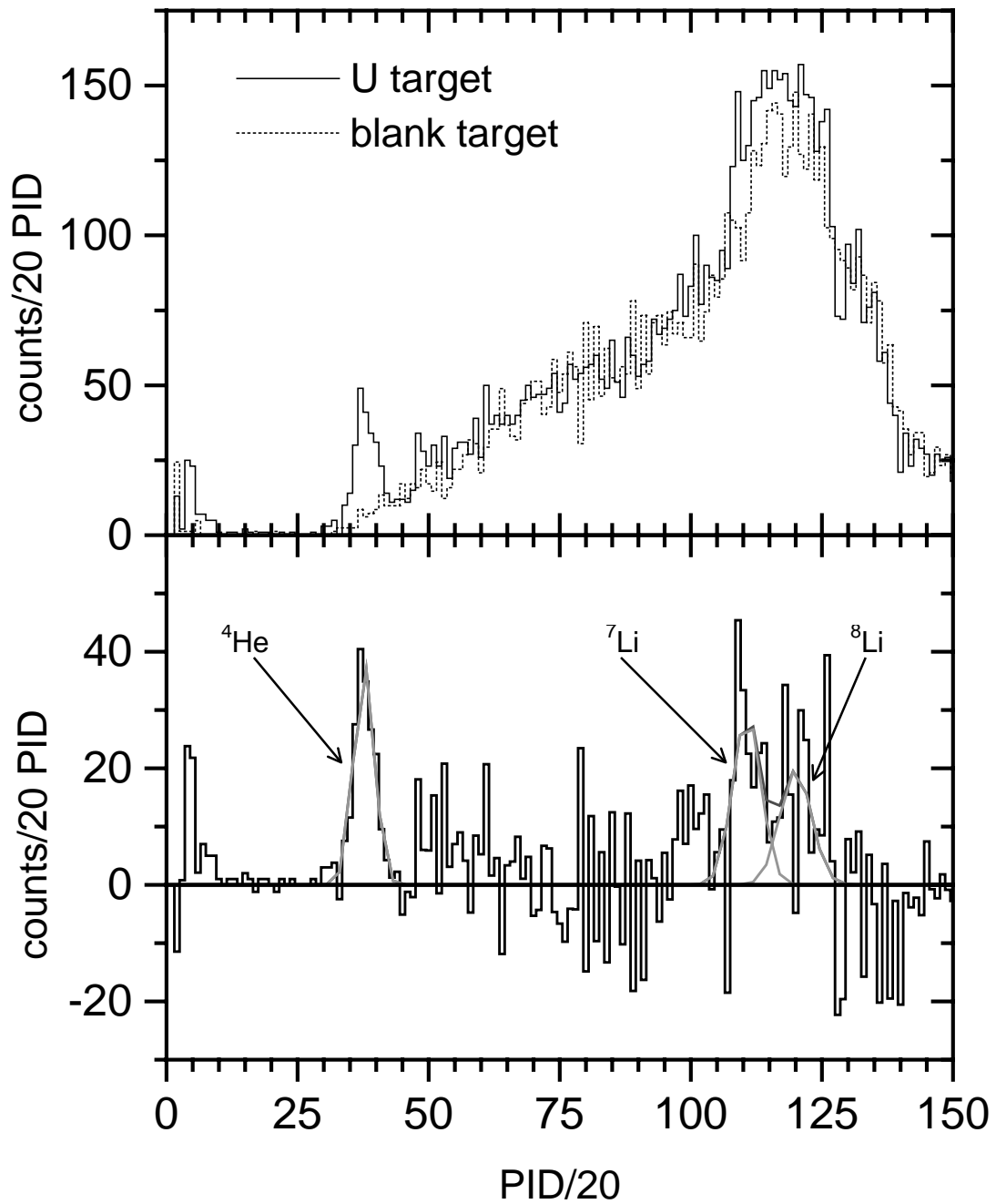


Figure 13 - The PID spectra for a U target. The upper pane shows the target in/target out data; the lower pane shows the difference of the two.

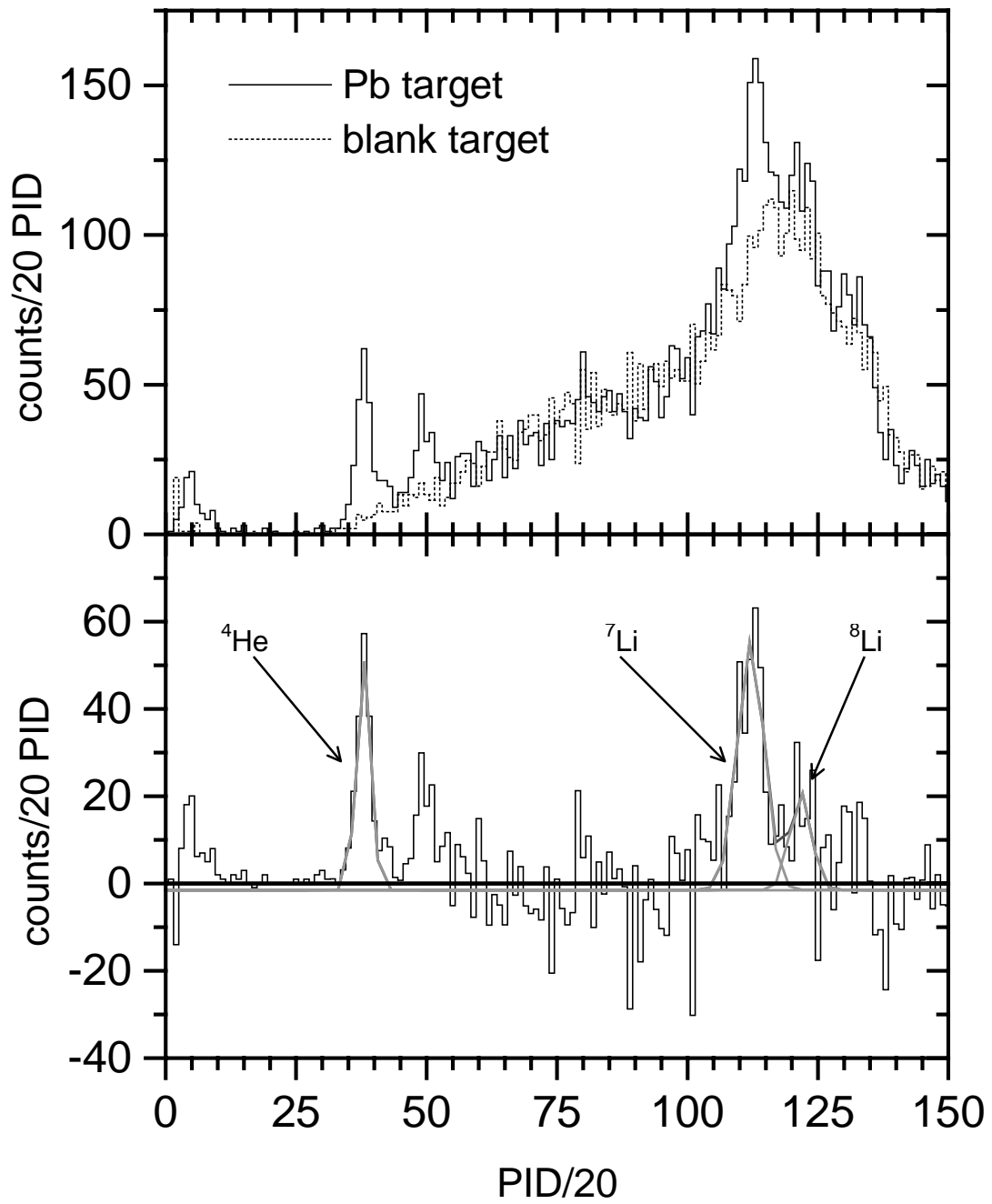


Figure 14 - The PID spectra for a Pb target. The upper pane shows the target in/target out data; the lower pane shows the difference of the two.

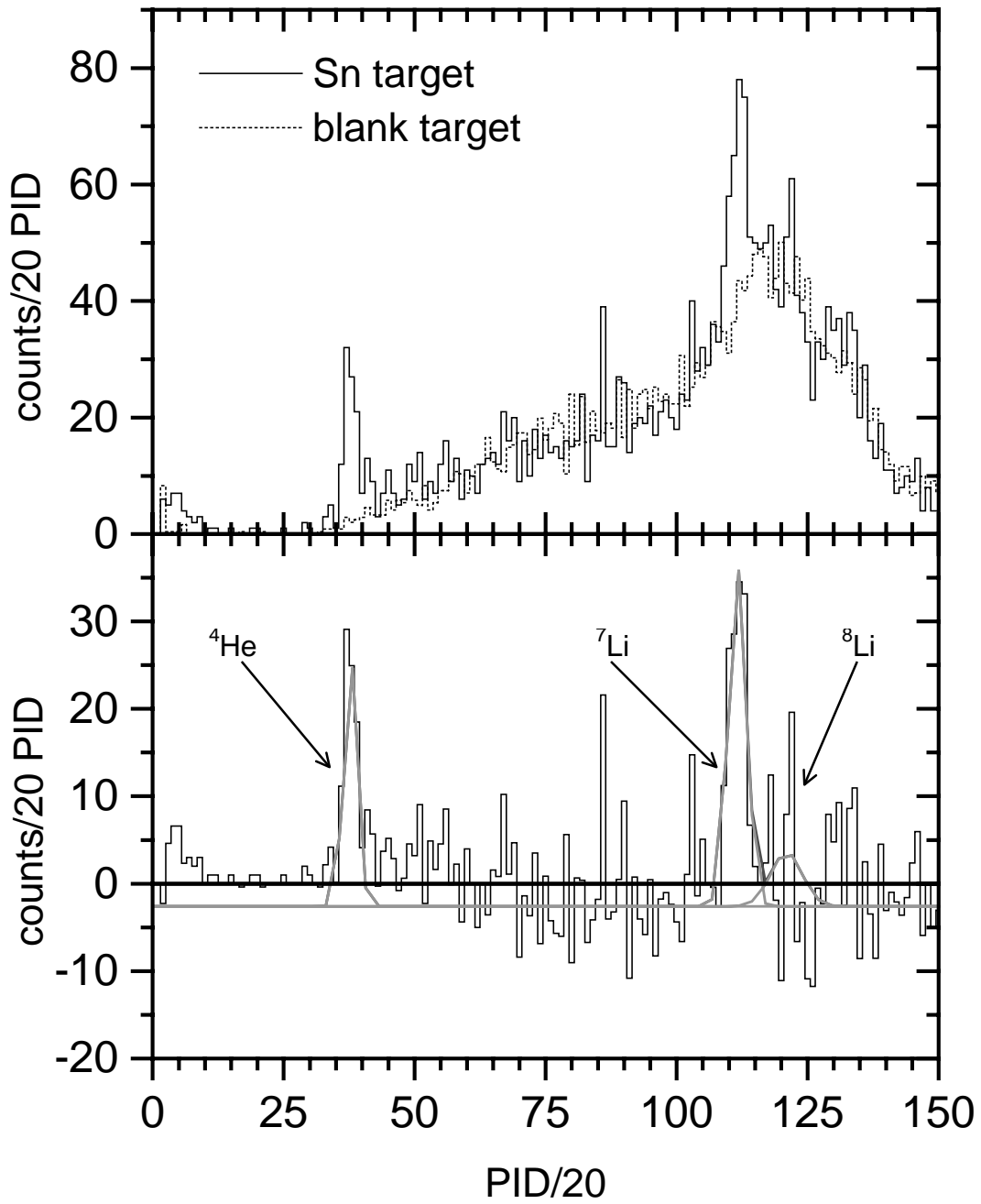


Figure 15 - The PID spectra for a Sn target. The upper pane shows the target in/target out data; the lower pane shows the difference of the two.

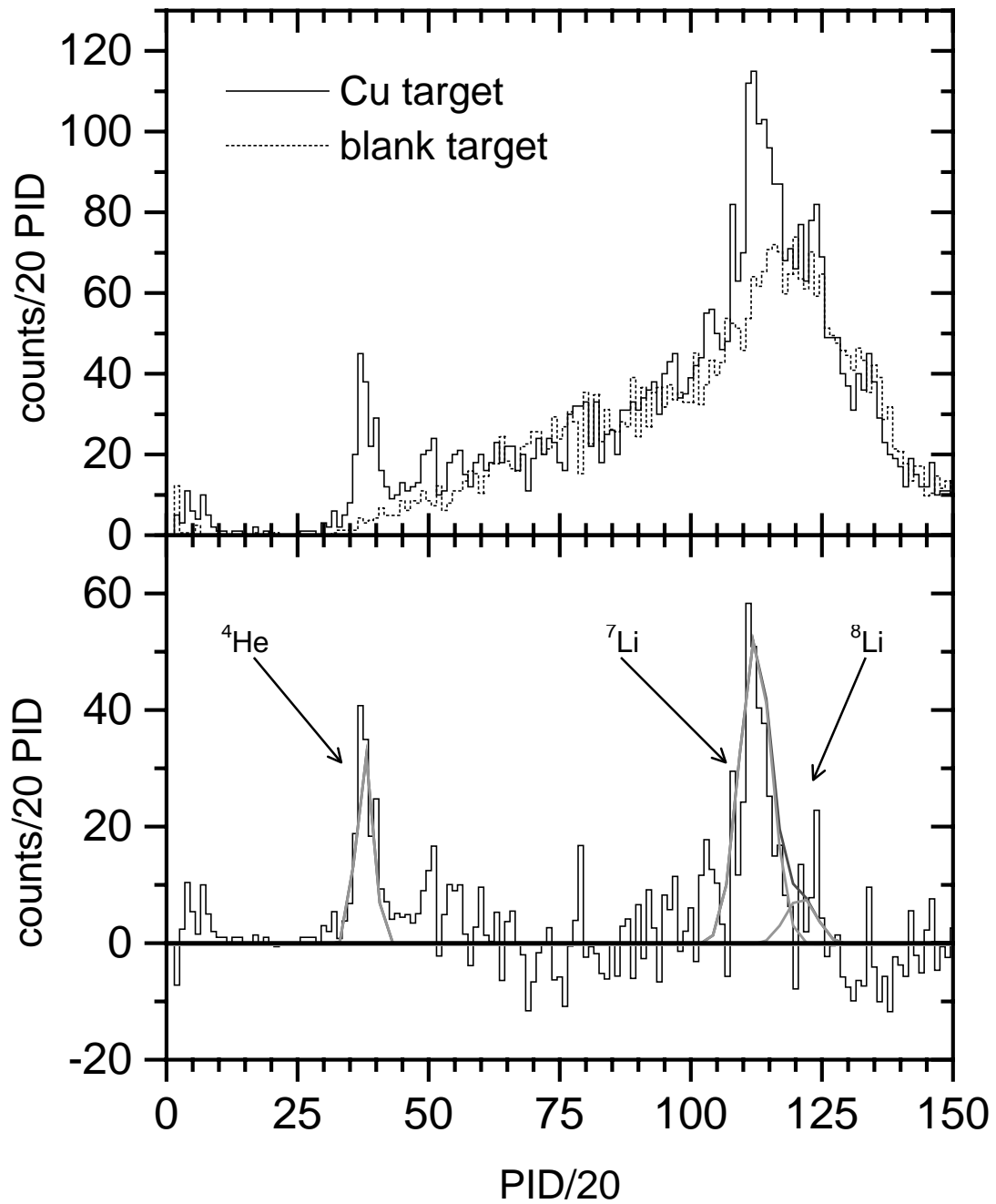


Figure 16 - The PID spectra for a Cu target. The upper pane shows the target in/target out data; the lower pane shows the difference of the two.

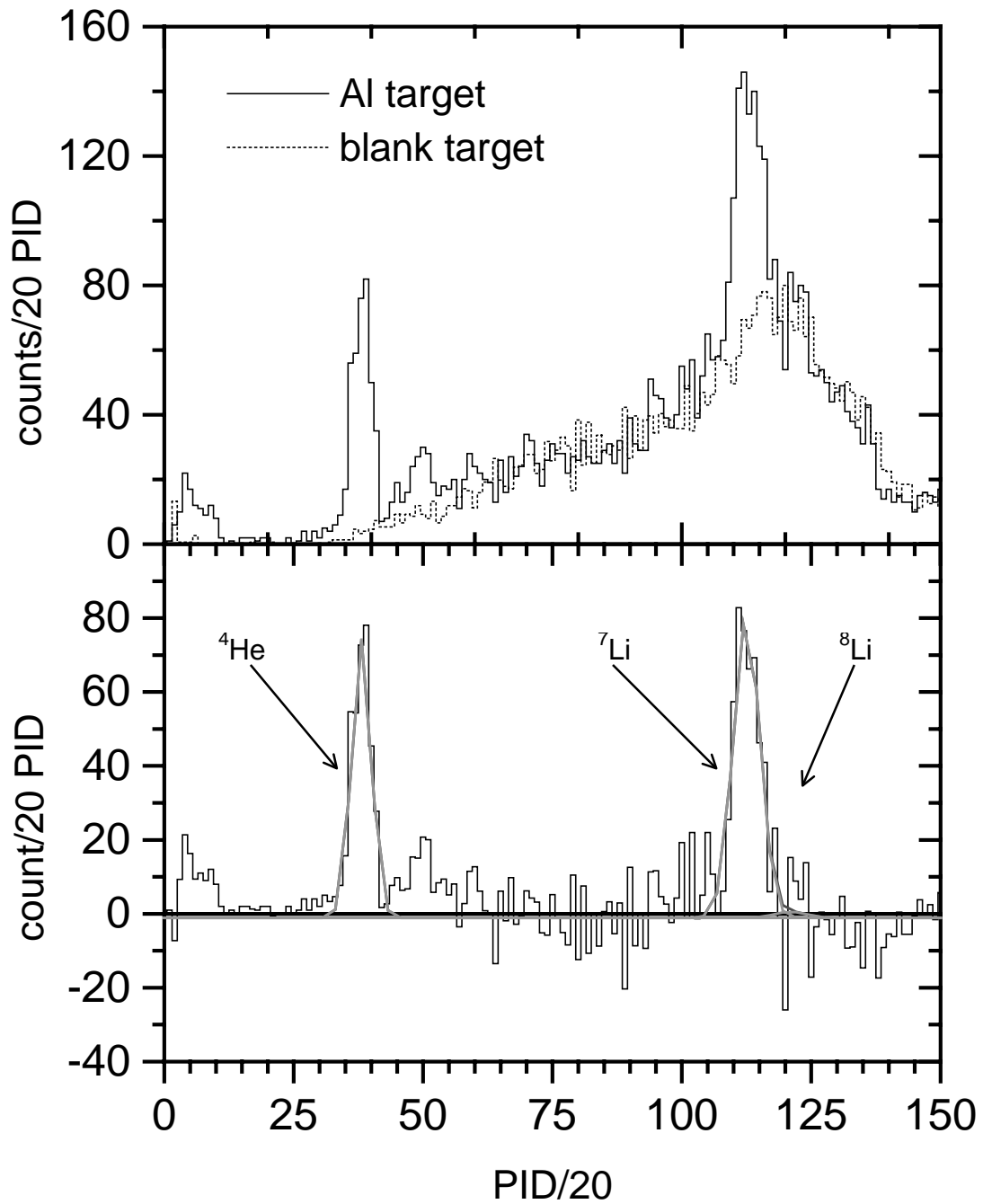


Figure 17 - The PID spectra for an Al target. The upper pane shows the target in/target out data; the lower pane shows the difference of the two.

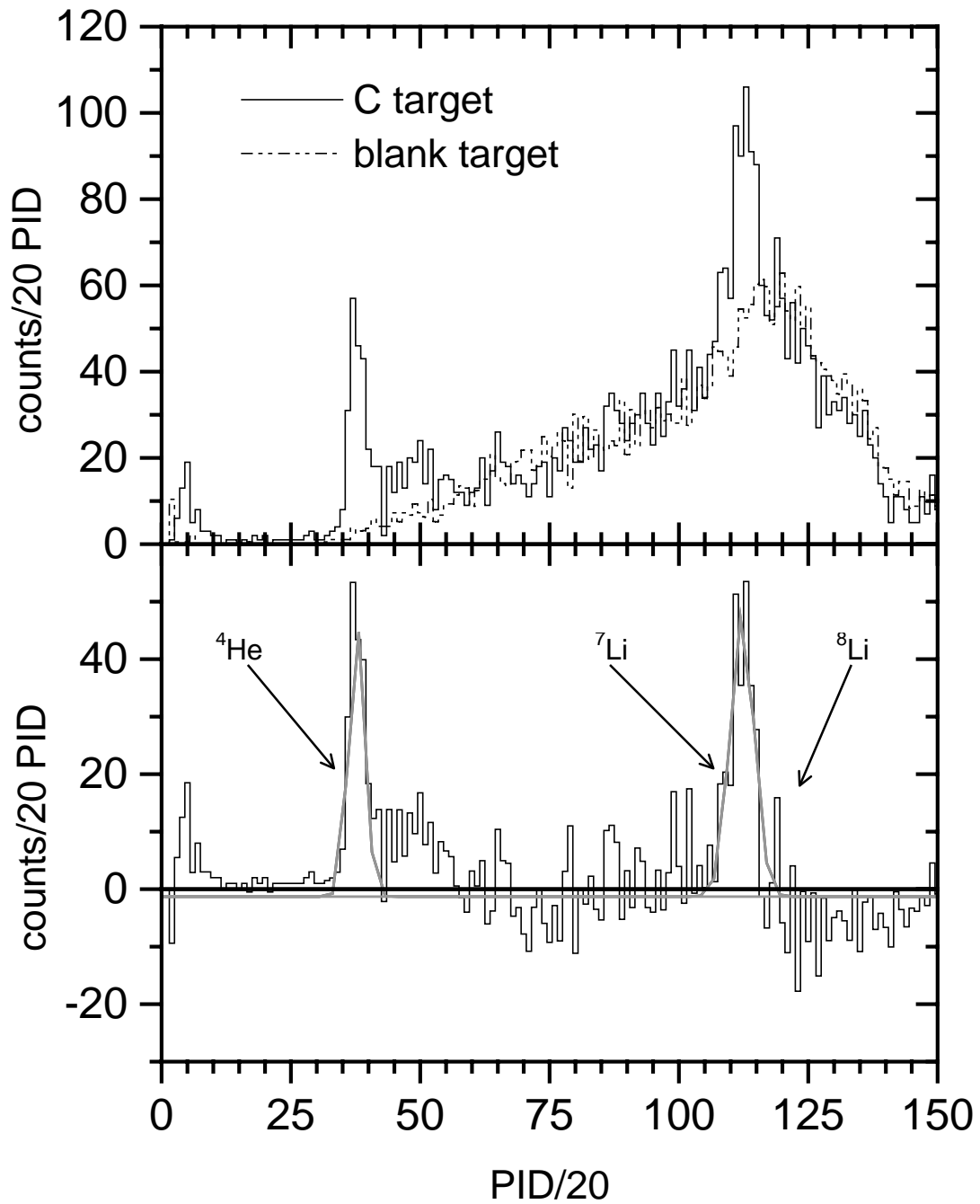


Figure 18 - The PID spectra for a C target. The upper pane shows the target in/target out data; the lower pane shows the difference of the two.

3.2 *Relative Energy Distribution*

Using the PID value from the telescope discussed in the previous section, we identify the ${}^8\text{Li}$ fragments as 1.5 times those within $\pm\sigma$ of the expected ${}^8\text{Li}$ PID value. This conservative definition of ${}^8\text{Li}$ PID is necessary because of the large yield of ${}^7\text{Li}$. For each identified ${}^8\text{Li}$ fragment, we use its total energy and direction from the target to determine its lab velocity, $\mathbf{V}_{{}^8\text{Li}}^{\text{lab}}$. We do the same for each neutron, and obtain $\mathbf{V}_n^{\text{lab}}$. Then, the relative decay energy E_d of the excited ${}^9\text{Li}$ is given by

$$E_d = \frac{1}{2} \mu \mathbf{V}_{rel}^2, \quad (7)$$

where μ is the reduced mass and $\mathbf{V}_{rel} = \mathbf{V}_n^{\text{lab}} - \mathbf{V}_{{}^8\text{Li}}^{\text{lab}}$. The yields for relative decay energy bins 0.5 MeV wide are shown in Figure 19 for the four heaviest targets. The error bars shown are statistical.

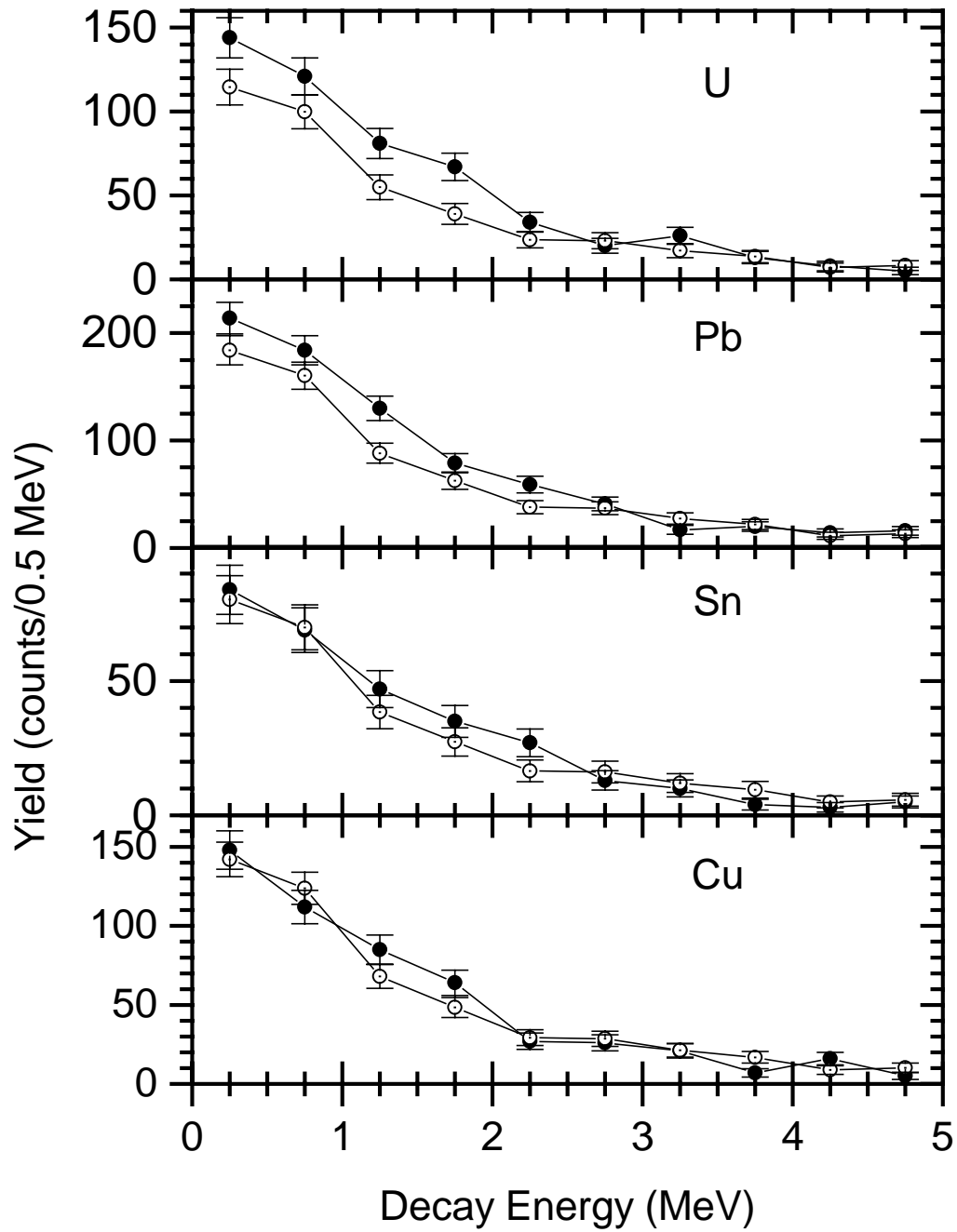


Figure 19 - Relative energy distributions for the four largest-Z targets. The solid circles represent the target-in data and the open circles represent the target-out data.

3.3 *Geometry and Efficiency Considerations*

To obtain the dissociation cross section from this measured yield, we must know the efficiency of our detection system. Two factors constitute the detection efficiency: the intrinsic efficiency of each detector, and the geometrical acceptance of the detectors. The geometrical acceptance decreases with increasing decay energy, therefore, the efficiency must be folded with the decay energy distribution and cannot be applied to the total yield.

The Si-CsI telescope has an intrinsic efficiency for particles that enter it of $\varepsilon=1$. The *Neutron Wall Array* is a more difficult problem. Since we detect a neutron by detecting the scintillation from an elastically scattered proton, the efficiency depends primarily on the (n,p) cross section and the thickness of the detector. Many computer simulations have been developed to calculate the efficiency of a neutron detector of a given geometry; we use a code called TOTEFF.¹⁷ The efficiency can vary significantly, depending on the velocity of the incident neutron; fortunately, our neutron velocities are narrowly focused about the beam velocity, see Figure 20. Therefore, we use the average efficiency of $\varepsilon=0.11$ for cells in the *Neutron Wall Array*.

Once these intrinsic efficiencies are known, we determine the overall efficiency by using the monte carlo method to simulate various decay energies and the geometrical acceptance of our apparatus. The curve of efficiency versus decay energy is shown in Figure 21. The dip around 0.5 MeV decay energy is attributed to the unsymmetrical distribution of active *Neutron Wall Array* cells about the 0° beam position.

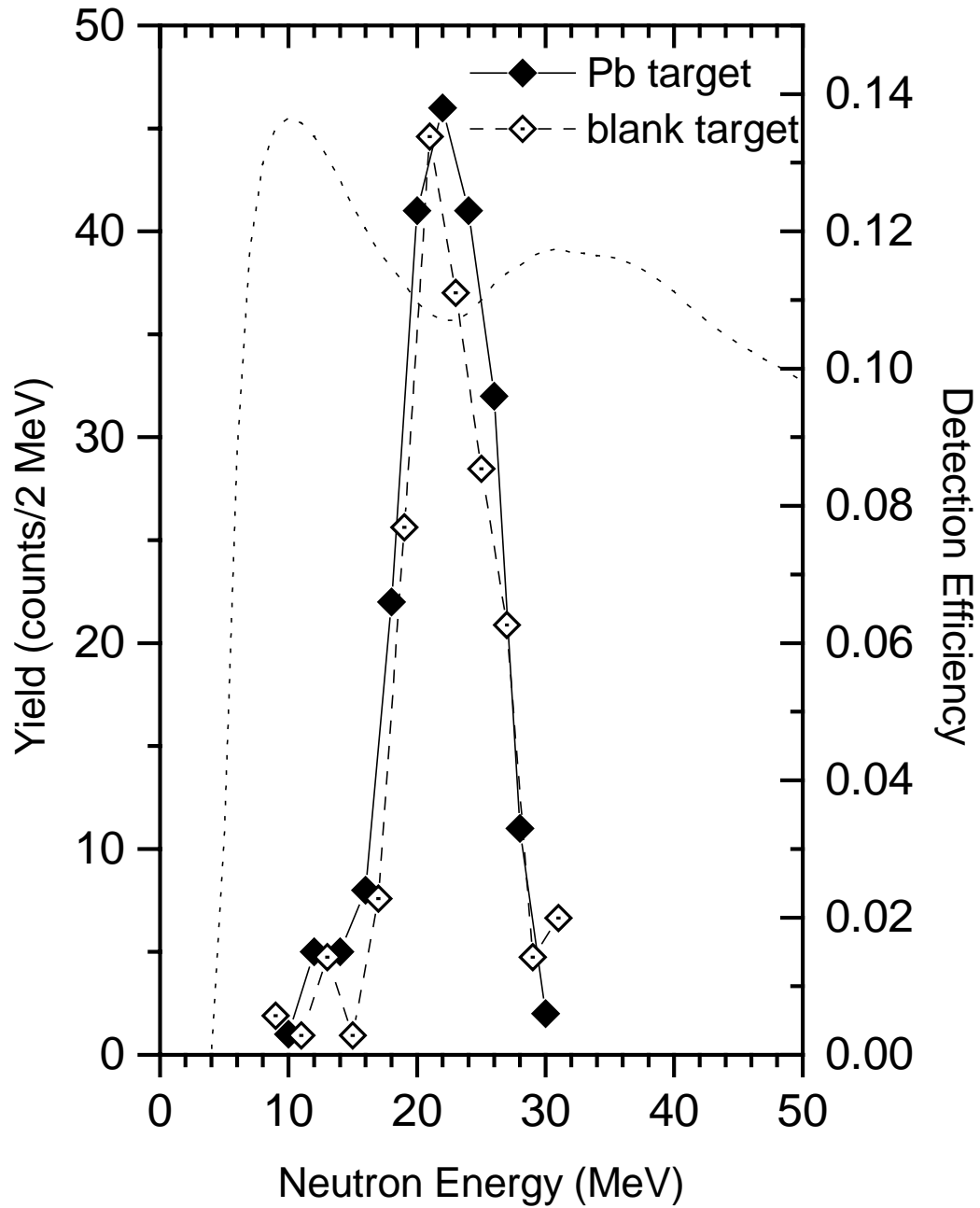


Figure 20 - Neutron energy distribution for the Pb target. The dashed curve represents the detection efficiency for neutrons in a detector with the approximate characteristics of a cell in the *Neutron Wall Array*.

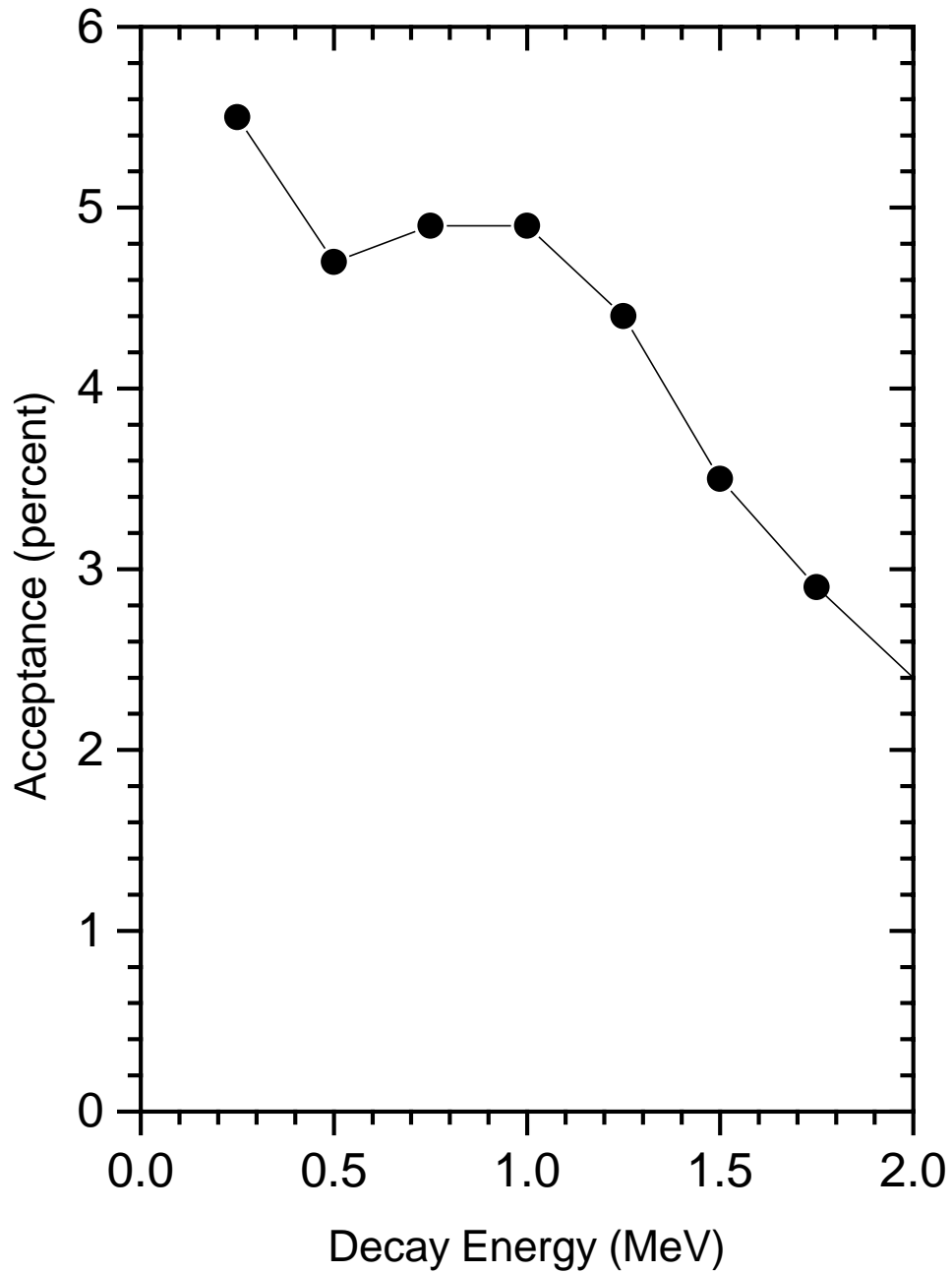


Figure 21 - The detector acceptance and efficiency. The dip at 0.5 MeV is from the asymmetric distribution of active cells in the *Neutron Wall Array*.

3.4 Virtual Photon Spectrum

To determine the photodisintegration cross section from the measured dissociation cross section, we must know the virtual photon number for each target nucleus. The virtual photon spectrum calculation and coulomb dissociation process are discussed at length in a review paper by Bertulani and Baur.¹⁸ Sackett has shown that their relativistic approximation for the E1 virtual photon number is valid for ^{11}Li in our velocity range.¹⁹ Sackett also demonstrated that there is little dependence on the projectile radius, and the relativistic approximation is independent of the mass of the projectile; therefore we use this relativistic approximation. The virtual photon number n_{E1} is given by

$$n_{\text{E1}}(E_\gamma / \hbar) = \frac{2}{\pi} Z_T^2 \alpha \left(\frac{c}{v}\right)^2 \left\{ x K_0 K_1 - \frac{1}{2} \left(\frac{v}{c}\right)^2 x^2 (K_1^2 - K_0^2) \right\}, \quad (8)$$

where K_0 and K_1 are modified Bessel functions of the argument x , with $x = E_\gamma b_{\text{min}} / \hbar \gamma v$. The minimum impact parameter, b_{min} , is the sum of the target and projectile radii. Figure 22 shows the virtual photon spectra as a function of photon energy for the six targets used.

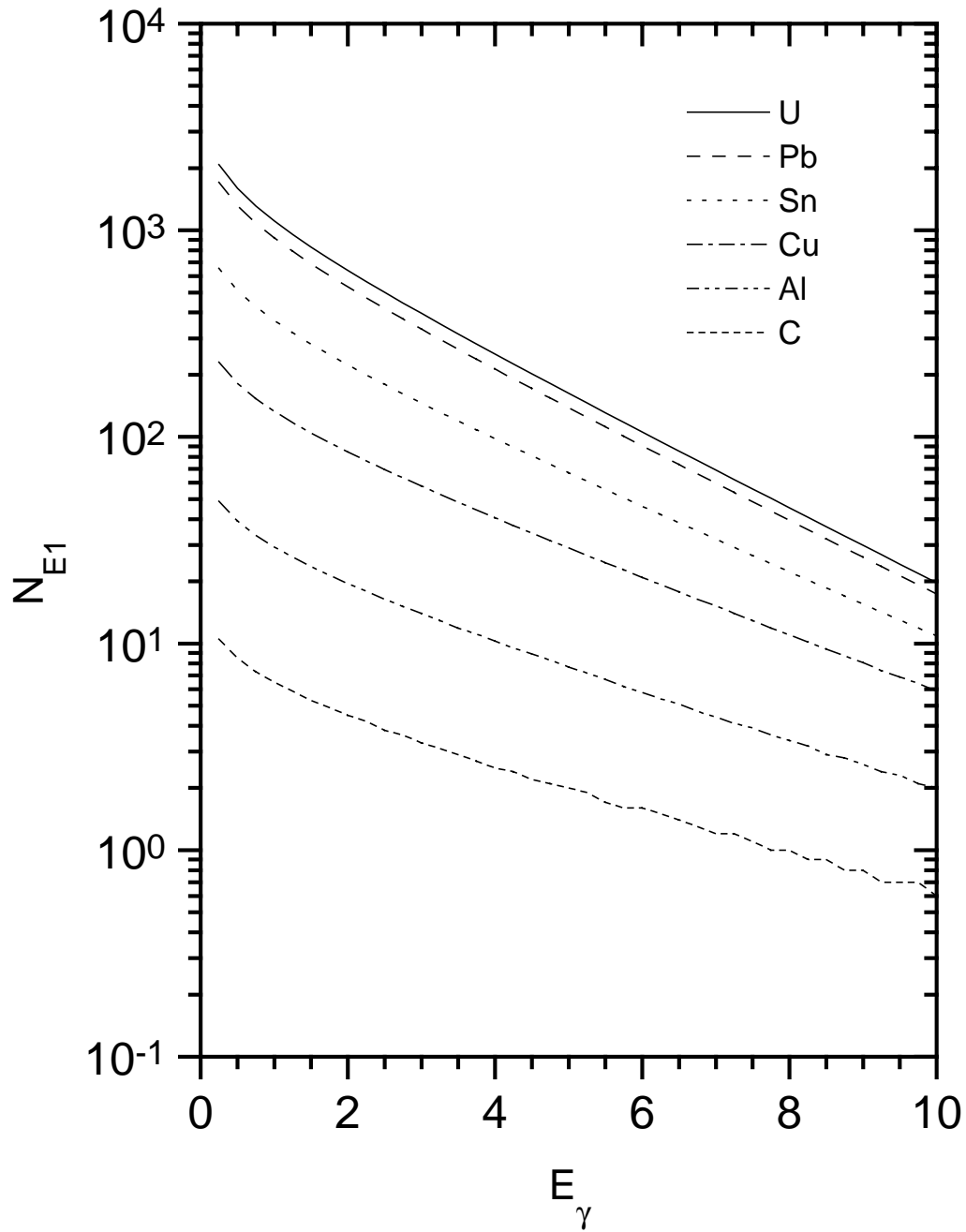


Figure 22 - The virtual photon number n_{E1} , as calculated by the commercial software package, *Mathematica*.

4 Results and Conclusions

Originally, the analysis was to follow this procedure:

1. measure the ${}^9\text{Li} \rightarrow {}^8\text{Li} + n$ dissociation cross section for six targets with Z from 6 to 92 (i.e. C, Al, Cu, Sn, Pb, U),
2. assume the ${}^9\text{Li}$ dissociation cross section for C and Al are primarily nuclear and then use the Z -dependence in a nuclear model to calculate the nuclear cross sections for the four higher- Z targets,
3. subtract the calculated nuclear cross sections from the measured cross sections for the higher- Z targets to obtain their coulomb cross sections,
4. finally, use these coulomb cross sections in the detailed balance theorem to obtain the ground state direct capture cross section, ${}^8\text{Li}(n,\gamma){}^9\text{Li}$.

Unfortunately, we did not observe any ${}^8\text{Li}$ in the target-out subtracted PID spectra for the C and Al targets (see Figure 17 and Figure 18), and are unable to calculate the corresponding dissociation cross sections. Without a measurement of these dissociation cross sections, we are not able to make any estimate of the nuclear dissociation cross sections for the heavier targets. To proceed, we can only discuss the present data in terms of limits to the coulomb cross section.

If all of the ${}^8\text{Li}$ production is assumed to proceed via coulomb dissociation, we obtain an upper limit on the coulomb dissociation cross section. With this extreme assumption, it is wise to consider only the highest- Z targets, Pb and U, where coulomb would play its largest role. If Y is the ${}^8\text{Li}$ yield for some range of decay energy where the ${}^8\text{Li}$ PID value was within $\pm\sigma_{PID}$ of the expected value, then the measured dissociation cross section, $\sigma_{measured}$, is given by

$$\sigma_{measured} = \frac{3}{2} \frac{Y}{\epsilon N_T N_p}, \quad (9)$$

where ε is the detection efficiency for the measured decay energy, N_P is the number of incident ${}^9\text{Li}$ particles, and N_T is the number of target atoms per square centimeter. The $3/2$ factor is included to compensate for our limited $\pm\sigma_{PID}$ range when selecting the ${}^8\text{Li}$ from its PID measurement. We obtain the differential cross section $d\sigma/dE_\gamma$ by dividing $\sigma_{measured}$ by the range of decay energies used to obtain $\sigma_{measured}$. From the differential cross section, the coulomb dissociation cross section $\sigma_{(\gamma,n)}$ is found using equation 3,

$$\sigma_{(\gamma,n)} = \frac{E_\gamma}{n_{E1}} \frac{d\sigma}{dE_\gamma}. \quad (3)$$

Finally, we use the detailed balance theorem, equation 1, to calculate the radiative capture cross section, ${}^8\text{Li}(n,\gamma){}^9\text{Li}$. Table 3 shows the results of these calculations for the Pb and U targets. For each target, two decay energy bins, 0.5 MeV wide, from 0 to 1.0 MeV were considered.

The radiative capture cross sections shown in Table 3 are only upper limits. To obtain a lower limit, we could assume that all of the observed ${}^8\text{Li}$ yield from the intermediate targets (Cu and Sn) is from nuclear processes, and then use these values to estimate the nuclear component for the heavier targets, much as we were going to do with the C and Al targets. Since calculating the measured cross section is dependent on knowing the decay energy, we would have to use the yields from the decay energy spectra, Figure 19. Although there is an observable ${}^8\text{Li}$ yield in the PID spectra for the intermediate targets, their yields are not statistically significant when broken down by decay energy. Therefore, we cannot use them to place any meaningful lower limit on the radiative capture cross sections.

Table 3 - The radiative capture cross section calculated from the detailed balance theorem.

Target	Decay Energy (MeV)	Observed Counts		$\sigma_{\text{meas}}(E_\gamma)$		$n(E_\gamma)$	$\sigma_{(\gamma,n)}$		$\sigma_{(n,\gamma)}$	
				(mb)	(mb)		(mb)	(mb)	(μb)	(μb)
U	0.0-0.5	29.4	± 16.1	13.9	± 7.6	225.44	0.53	± 0.3	19.1	± 10.4
U	0.5-1.0	21.2	± 14.9	10.2	± 7.1	186.05	0.53	± 0.4	7.9	± 5.5
Pb	0.0-0.5	29.9	± 20.0	10.8	± 7.2	188.56	0.50	± 0.3	17.8	± 11.9
Pb	0.5-1.0	23.6	± 18.6	8.7	± 6.9	154.16	0.54	± 0.4	8.1	± 6.4

Although we have only been able to determine an upper limit to the radiative neutron capture cross section for ${}^8\text{Li}$, it is still of some use for its astrophysical implications considering the large range of theoretical estimates. These estimates are shown in Figure 23 along with our measured limits from the U target. The estimates shown are for the direct capture to the ground state unless otherwise noted. We only compare our data to the ground state capture since we assume the ${}^9\text{Li}$ is in its ground state when we measure the inverse reaction ${}^9\text{Li}(\gamma,n){}^8\text{Li}$. The direct capture to the ground state should be stronger than to the one bound excited state at 2.691 MeV²⁰ since the transition strength goes as E_γ^3 .

A neutron-unbound state exists at 0.247 MeV above the one neutron separation threshold. Although there are no experimental determinations of this state's spin-parity²⁰, two shell model calculations by Mao and Champagne²¹ predict it to be $J^\pi = \frac{5}{2}^-$. Given this spin-parity, p -wave neutrons will dominate the resonance capture cross section. Since neutrons at such a low resonance energy are primarily s -wave, the resonance is not expected to contribute much to the cross section. Also, the only transition from this excited state is through electric quadrupole radiation, further suppressing the resonance contribution.

Of the four theoretical estimates shown, two are based on models of the ${}^9\text{Li}$ structure, and two are based on the systematics of similar nuclei. Of the

model calculations, we are in sharp disagreement with the spd-shell model calculations of Mao & Champagne²¹ and consistent as an upper limit with the cluster model calculations of Descouvemont²². Similarly, we are in disagreement with the estimates of Malaney & Folwer,²³ and consistent with the estimates of Rauscher.²⁴

Considering their astrophysical interest, radiative capture cross sections are often discussed in terms of a reaction rate per particle pair, $N_A \langle \sigma v \rangle$, where N_A is Avogadro's number. The reaction rate is given by

$$\langle \sigma v \rangle = \int_0^{\infty} \phi(v) \sigma(v) v dv, \quad (10)$$

where $\phi(v)$ is the normalized Maxwell-Boltzman distribution, $\sigma(v)$ is the cross section, and v is the relative velocity. This reaction rate is approximately constant for low-energy, s -wave neutron capture because the cross section for the direct capture of s -wave neutrons is proportional to $1/v$. By fitting a $1/v$ function to our data points, we obtain an upper limit to the reaction rate, $N_A \langle \sigma v \rangle = 9560 \text{ cm}^3 \text{ s}^{-1} \text{ mole}^{-1}$. This rate, and the four theoretical estimates are given in Table 4.

Table 4 - Reaction rates for the four theoretical estimates and our data.

	Reaction Rate $\text{cm}^3 \text{ s}^{-1} \text{ mole}^{-1}$
Malaney & Fowler	4.294×10^4
Mao & Champagne	2.10×10^4
NSCL-MSU	9560
Descouvemont	5280
Rauscher, <i>et al.</i>	4650

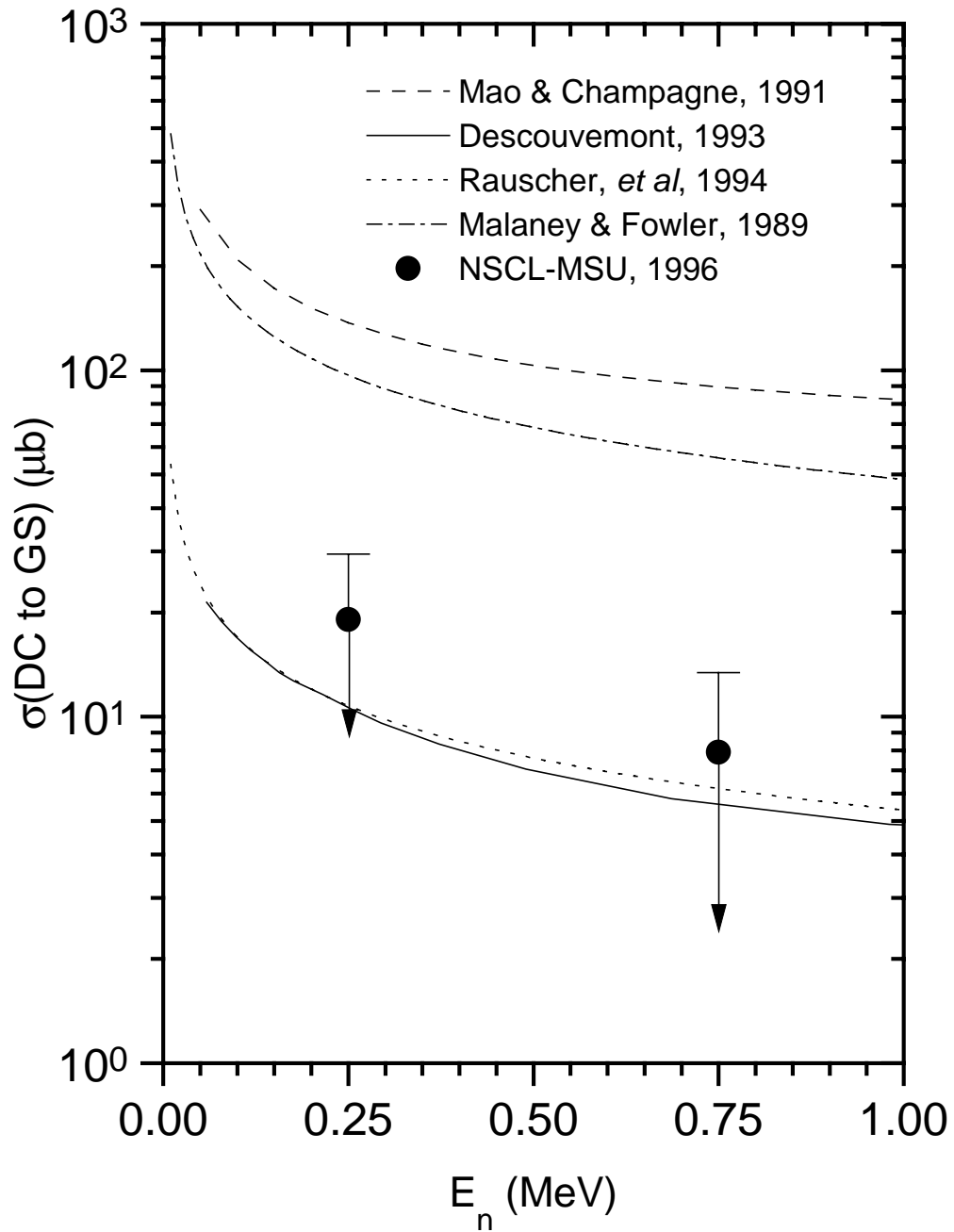


Figure 23 - Radiative capture cross sections for ${}^8\text{Li}(n,\gamma){}^9\text{Li}$. The data points are upper limits measured using the coulomb dissociation method with a U target. All curves are for direct capture to the ground state, except Malaney & Fowler, which is for direct capture to the ground state and first excited state.

In an inhomogeneous early universe, nucleosynthesis in neutron rich regions could produce an observable amount of $A > 12$ isotopes, whereas the standard-big bang nucleosynthesis ends with the production of ${}^7\text{Li}$. The primary reaction chain to heavy elements begins with ${}^7\text{Li}(n,\gamma){}^8\text{Li}(\alpha,n){}^{11}\text{B}$ and has a weaker channel beginning with ${}^7\text{Li}(\alpha,\gamma){}^{11}\text{B}$. The ${}^8\text{Li}(n,\gamma){}^9\text{Li}$ and ${}^8\text{Li}(d,n){}^9\text{Be}$ reactions provide so called leaks from the main sequence, reducing the heavy element production. These leaks could reduce the heavy element production by half according to Malaney & Fowler.⁵ Our data suggest that the reduction might not be so large.

In conclusion, we have used the coulomb dissociation method to determine an upper limit to the ${}^8\text{Li}(n,\gamma){}^9\text{Li}$ radiative capture cross section. The very small yield from low-Z targets prevented us from making any estimate of the nuclear contribution to the measured dissociation cross section from high-Z targets. Without this estimate, our measurement can only be interpreted as an upper limit. Even so, current estimates of this cross section range over an order of magnitude, and our measurement is only consistent with the lowest estimates.

5 Discussion for Future Experiments

Had we determined a ${}^9\text{Li}(\gamma,n){}^8\text{Li}$ cross section for C and Al, we would have then used it to estimate the nuclear cross section for the higher-Z targets. Doing so would require a model for the nuclear dissociation. In one type of model nuclear reactions would occur via central collisions, in another via peripheral collisions. If the observed dissociation cross section was primarily from central collisions, then the cross section would depend on the cross sectional area of the target-plus-projectile, or roughly scale as $A^{2/3}$, where A is the atomic number of the target. If the dissociation cross section was primarily

from peripheral collisions, then the cross section would depend on the cross sectional circumference of the target-plus-projectile, or scale as $A^{1/3}$.

Further consideration is necessary to determine which model is more appropriate. The detector geometry is a factor in determining whether we observe central or peripheral collisions. Our detectors subtend only a narrow forward angle, and by detecting both the neutron and the fragment in the forward direction, we favor peripheral collisions. We can also observe the energy distribution of the neutrons; while neutron velocities from peripheral collisions will be peaked around the beam velocity, neutrons from central collisions will exhibit an exponential decay distribution. Since the ${}^8\text{Li}$ events from the high-Z targets contain some amount of coulomb dissociation, which result from peripheral collisions, their neutron energy distributions might not provide the best evidence for peripheral or central nuclear collisions.

The data from the ${}^9\text{Li} \rightarrow {}^7\text{Li} + 2n$ events should contain a weaker coulomb component because of the greater 2 neutron separation energy, $S_{2n} = 6.1$ MeV as compared to $S_{1n} = 4.1$ MeV. The low-Z targets are still preferable for measuring the nuclear effect, and whereas there are no ${}^8\text{Li}$ events for the low-Z targets, there are plenty of ${}^7\text{Li}$ events as Figure 17 Figure 18 show. Figure 24* shows the neutron distribution for the ${}^7\text{Li}$ events from the C and Al targets (the target-out background has been subtracted). Clearly, the neutron energy spectrum is peaked near the beam velocity, indicating that we are detecting primarily peripheral events.

* The neutron energy distribution shown in Figure 20 is not appropriate for this discussion because by selecting neutrons from events with a given decay energy, we have selected a narrow range of neutron energies.

One of the assumptions for calculating the nuclear dissociation cross section by scaling cross sections from low-Z targets was that the dissociation cross section would have two contributions, one nuclear ${}^9\text{Li} \rightarrow {}^8\text{Li} + n$, and one coulomb ${}^9\text{Li} \rightarrow {}^8\text{Li} + n$. As we clearly see from the PID spectra, ${}^9\text{Li} \rightarrow {}^7\text{Li} + 2n$ and ${}^9\text{Li} \rightarrow {}^6\text{He} + 3n$ are very strong channels. These channels' actual relative strength compared to the ${}^9\text{Li} \rightarrow {}^8\text{Li} + n$ channel may be misrepresented in the PID spectra because they could be producing more neutrons. A measurement of the $2n$ cross section for the ${}^9\text{Li} \rightarrow {}^7\text{Li} + 2n$ reaction would provide more information about the nature of the reaction. The strong presence of these two channels increases the difficulty in modeling the nuclear dissociation cross section for the ${}^9\text{Li}(\gamma,n){}^8\text{Li}$ reaction. These considerations will have to be addressed when a better measurement of the ${}^8\text{Li}(n,\gamma){}^9\text{Li}$ cross section is attempted.

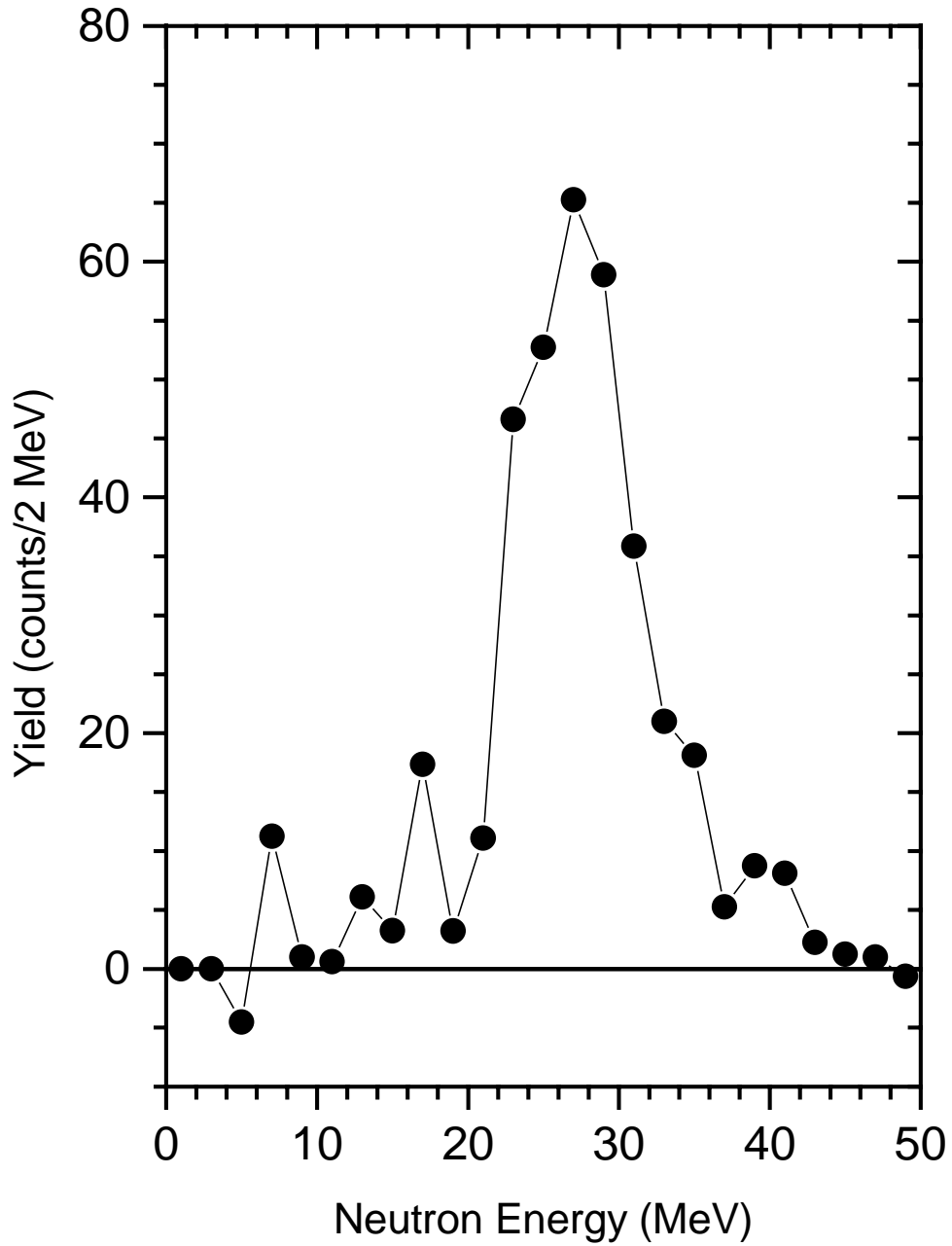


Figure 24 - The neutron energy distribution for neutrons in coincidence with ${}^7\text{Li}$ fragments from the C and Al targets. This shows the results from a target-in/target-out background subtraction. The narrow energy distribution near the beam velocity is indicative of a peripheral collision.

Part II

A Large-Area, Position-Sensitive Neutron Detector with Neutron/ γ -ray Discrimination Abilities.

6 Motivation

We have constructed a large-area, position sensitive neutron detector with neutron/ γ -ray discrimination abilities, called the *Neutron Wall Array*. Although the *Neutron Wall Array* was originally intended for a particular experiment, it has already been used in a number of other experiments and has been incorporated into the design of the future experiments of other research groups using the NSCL facility. Section 6 discusses the original motivation behind the construction of the *Neutron Wall Array* and the original design requirements. Section 7 is a brief discussion of the principles of neutron detection methods used by the *Neutron Wall Array*. An outline of the physical construction and a demonstration of the primary functions of the detector are shown in section 8. Section 9 presents some of the operational procedures used in the experiments to date. Finally, section 10 outlines the three experiments that have used the *Neutron Wall Array*.

6.1 Radioactive Nuclear Beam Advances

Our original motivation for building the *Neutron Wall Array* was to improve and extend measurements made at the NSCL of neutron-rich nuclei. These measurements are part of an extensive research program the NSCL has developed around its production of radioactive nuclear beams (RNBs). One of the biggest opportunities RNBs offer is the chance to systematically study

isotopes far from the limits of stability. Many of these unstable isotopes are very-neutron rich, and neutron detection has played an important roll in probing their structure. The nature of RNBs has also lead to a change in the size and scope of the neutron detectors that are needed.

The primary difference in working with RNBs is a great reduction in intensity in comparison to beams of stable nuclei. RNBs are the result of sifting through the many fragmentation products produced when an intense primary beam of heavy ions strikes a thick target. Consequently, radioactive beam intensities are much lower than primary beam intensities. A typical experiment with a stable beam would have an intensity of about 10^{12} particles per second; in constrast, an experiment with a radioactive beam might have an intensity of only hundreds or thousands of particles per second. With such low beam intensities, it is preferable to cover as much solid angle as possible to reduce the beam time necessary to aquire sufficient statistics for an experiment.

The reduction in beam intensity is even more accute if two or more neutrons must be detected in coincidence. Unlike most charged particle detection, neutron detectors do not have an efficiency of 100 percent; a common value for one-neutron detection efficiency is about 10 percent. If two neutrons are to be detected in coincidence, then the efficiency falls to 1 percent. Since the two-neutron detection efficiency goes as the square of the one-neutron efficiency, it is useful to try to increase the one-neutron efficiency.

6.2 *The $^{11}\text{Li}(\gamma,2n)^9\text{Li}$ Experiment*

One of the early clues to the richness of RNBs was the anomalously large cross section for ^{11}Li interacting with various target nuclei.²⁵ For years the nuclear density was thought to be nearly constant throughout the table of

isotopes, but studying ^{11}Li has demonstrated that far from stability, the final nucleons added to a system may form a low-density halo around a more common core. A recent experiment that studied ^{11}Li is an excellent example of the added complexities of working with neutrons from RNB experiments. First, the experiment required two neutrons to be detected in coincidence, and second, the available beam intensity was only 500 ^{11}Li per second. The *Neutron Wall Array* was constructed to replace the neutron detectors used in this experiment with a device that has better resolution and efficiency. What follows is a brief description of this experiment and the limitations of the neutron detector used.

In 1991, Sackett *et al.* performed an experiment to measure the soft-dipole-resonance parameters and ground state n - n correlations of ^{11}Li . To accomplish this, they made a complete kinematics measurement of the coulomb dissociation of ^{11}Li as it passed through the virtual photon field of a Pb nucleus. In this situation, if the ^{11}Li absorbed a virtual γ -ray from the Pb nucleus with sufficient energy to excite it above the two-neutron separation energy, it could dissociate into a ^9Li and two neutrons. By measuring the velocities of the incident ^{11}Li , the ^9Li fragment and the two neutrons, it is possible to determine the γ -ray energy and then determine the $(\gamma 2n)$ decay cross section.

The experimental setup used by Sackett *et al.* is shown in Figure 25. A beam of 30 MeV/nucleon ^{11}Li 's were produced by the A1200 fragment separator. The beam was incident on a Pb target after passing through two position-sensitive parallel-plate avalanche counters (PPACs) used to determine the incident direction of the ^{11}Li . After dissociation in the Pb target, the ^9Li fragment's energy and position were measured in a Si-CsI telescope about 15 cm downstream from the target. The two neutrons passed through the telescope and were detected in two arrays consisting of 54 small scintillation detectors.

The arrays were placed 5 and 6 meters downstream and subtended a maximum half-angle of 5 degrees. Each neutron's energy was determined by measuring its time of flight from the target. The neutron's direction was determined by knowing which detector it hit.

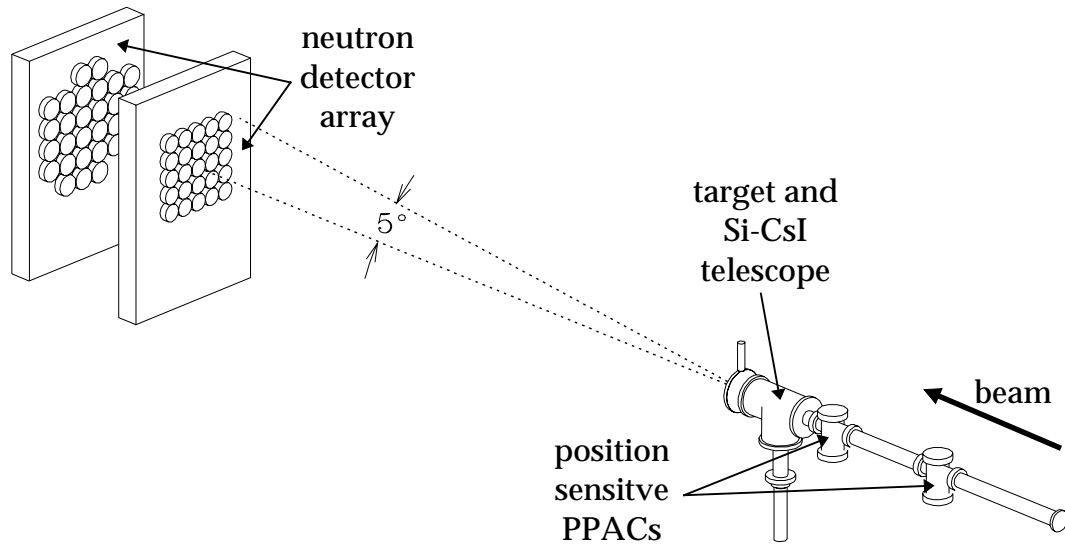


Figure 25 - Experimental setup to measure the complete kinematics of $^{11}\text{Li} \rightarrow ^9\text{Li} + 2n$ events (Sackett *et al.*, 1991).

The neutron detectors used were small cylindrical scintillation counters, shown in Figure 26. The liquid scintillator volume was housed in an aluminum can; one end of the can was open and optically coupled to a large plastic light pipe attached to a photomultiplier tube. The neutrons were incident parallel to the axis of the cylinder. When these detectors are stacked into a tight array, the cylindrical design creates a 50 percent dead space between the detectors, decreasing the array's efficiency. To help boost the efficiency, a second array was added behind the first. The experimenter choose a second array instead of increasing the thickness of the detectors' to increase the efficiency. The reason for not increasing the detectors thickness is that it adds uncertainty to the flight path's length and thus to the measured neutron energy. Unfortunately, adding

the second array complicates the analysis by enhancing the effects of cross-talk and what we call out-scattering.

Cross-talk is the familiar problem of one neutron creating signals in two separate detectors. Out-scattering is a process whereby a neutron scatters from the non-active part of a detector and is then detected in a different detector with a distorted position and TOF (energy) measurement. While methods exist for identifying and eliminating cross-talk events from the data, there are no methods available identifying out-scattering events. Therefore, the neutrons should pass through as little non-active material as possible. Unfortunately, the neutron detectors used in the array had a ratio total mass to active mass of over 4 to 1.

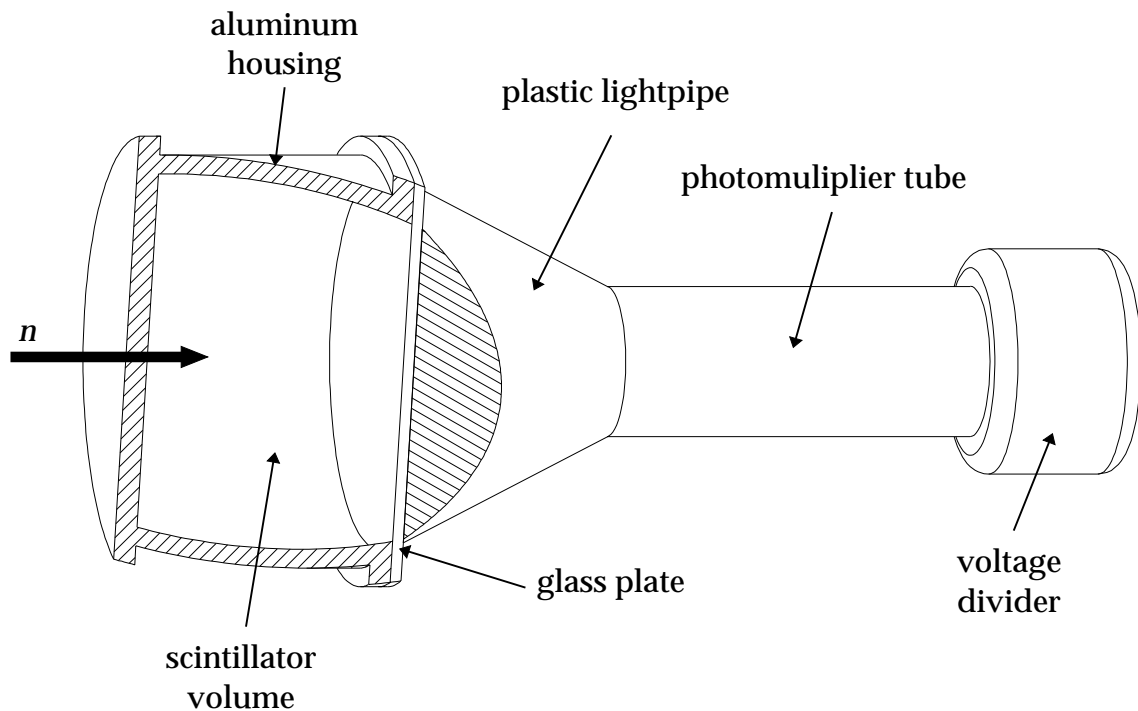


Figure 26 - A cutaway diagram of a neutron detector used by Sackett *et al.* Neutrons are incident from the left. The scintillator is 5 inches in diameter and 3 inches in depth for a volume of 59 in³ (0.97 liters).

For small decay energies, the reaction products were forward focused in the lab and the setup had a reasonable geometric efficiency. Given a one-neutron

detection efficiency $\varepsilon_{neutron}$ of 10%, a ^{11}Li reaction probability in the target $P_{reaction}$ of 1%, a beam intensity I of 500 $^{11}\text{Li}/\text{sec}$, and the factor $\frac{1}{2}$ for the empty space in the array, a simple estimate of the counting rate is

$$\varepsilon_{neutron} \varepsilon_{neutron} P_{reaction} I = 0.1 \times 0.1 \times 0.01 \times 500 \times \frac{1}{2} = 0.025 \text{ events / sec}$$

For larger decay energies, this counting rate drops as the geometrical efficiency drops.

The intense interest in neutron-rich nuclei and the intriguing questions posed by this experiment lead us to attempt to improve it. The first improvement is to measure larger decay energies, where the geometrical efficiency of Sackett's setup is small. The second improvement is to increase the energy resolution of the decay energy spectrum. Unfortunately, increasing the energy resolution requires decreasing the target thickness, thus reducing $P_{reaction}$. These factors reduce the counting rate to an unacceptably low value. Although some improvement has been made in the intensity of ^{11}Li beams, it is not enough to compensate for these new requirements. Therefore, we are left with improving the detectors in the experiment to increase the geometrical efficiency and the one-neutron detection efficiency.

The first area of improvement was the neutron detector array. To overcome many of the limitations imposed on Sackett's experiment by the array, we proposed, designed, and constructed what is now called the *Neutron Wall Array*. We had four main objectives when designing the *Neutron Wall Array*:

1. Increase the angular acceptance of the array by increasing its area,
2. To greatly decrease the dead-space between the individual detectors,
3. To reduce the inactive (non-scintillator) mass through which the neutrons must pass to reduce scattering,

4. To increase the total area of the detector array while decreasing the ratio of the number of electronic channels to scintillator volume.

This last point is simply one of cost-savings; as an example, if we duplicated the existing detectors so we could cover the same solid angle as we intend on covering with the new detector, we would need over 500 individual detectors with over 500 channels of associated electronics.

To meet our objectives, we are using the well known geometry of long rectangular scintillator cells, placed perpendicular to the beam axis. Each cell is viewed at both ends by photomultiplier tubes (PMTs). By using 25 cells of scintillator, each 2 meters long, we will cover an area of 4 m² in each wall. Using the same flight path as the previous experiment, the array will subtend a half-angle of 15 degrees where the previous array only subtended a half-angle of 5 degrees. A time signal for the time-of-flight measurement is obtained from the mean time of the PMT signals. The position of the event along the cell is determined from the time difference between the signals. The thickness of the cell in the beam direction is determined by the energy resolution we wish to achieve with a 5 meter flight-path. To increase the efficiency, we created two identical arrays of 25 cells, so that one can be placed behind the other.

Complicating the design of the detector is a requirement that the detector be capable of pulse-shape-discrimination (PSD) to distinguish between neutron and γ -ray events. When the time-of-flight method is used to determine energy, a time-independent γ -ray background will introduce a constant background in the neutron spectrum; because we wish to study a continuous neutron energy spectrum, we must have some method of eliminating this γ -ray background from the neutron spectrum. Also, γ -ray identification plays an important role in cross-talk rejection. The complication in the design arises because the only

scintillators capable of PSD are a few liquid hydrocarbon scintillators. Instead of the self-supporting plastic bars of scintillator that are usually employed in the configuration we are using, our scintillator is housed in long, cast Pyrex tubes that are sealed at both ends. Although the Pyrex cell adds non-active material through which neutrons must pass, the ratio of total-mass to active-mass is much less than with the previous detector configuration.

7 Neutron Detection at Intermediate Energies

Given the general operating parameters of the NSCL's cyclotron, neutrons from nuclear reactions can have anywhere from a few MeV to a few hundred MeV in energy. The next four sections discuss the basic principles of detecting neutrons in this energy range, so called fast neutrons. A more detailed discussion of fast neutron detection can be found in reference 26.

The lack of charge makes a neutron very difficult to detect directly. Therefore, almost all neutron detection methods involve imparting some or all of the neutron's kinetic energy to a charged nucleus that is then detected. The simplest means of doing this is to transfer some of the neutron's energy through elastic scattering, creating a *recoil nucleus*. Since the energy of a recoil nucleus will be a random fraction of the neutron's energy, we cannot determine the neutron's energy by measuring the energy of the recoil nucleus. To determine the neutron's energy, we measure the time the neutron takes to travel from the target to the detector. Then, if the length of the flight path is known, we can determine the neutron's velocity and energy regardless of the energy deposited in the detector.

The more energy the recoil nucleus has, the easier it is to detect. Simple two body kinematics gives the maximum recoil energy $E_R|_{\max}$ for elastic neutron scattering as

$$E_R|_{\max} = \frac{4A}{(1+A)^2} E_n, \quad (11)$$

where A is the mass number of the recoil nucleus and E_n is the neutron's incident energy.²⁷ The maximum recoil energy is obtained when $A=1$; therefore, it is preferable to use hydrogen as the primary scattering target for neutron detection. Detectors based on hydrogen scattering are called *proton recoil detectors*.

7.1 Scintillation Detection

Scintillation detectors are among the most popular devices used as proton recoil detectors. Scintillation detectors convert the kinetic energy of ionizing radiation into detectable light pulses. In the case of neutron detection, the ionizing radiation is an elastically-scattered recoil proton from a hydrogen atom in the scintillator material. Most recoil protons will deposit all of their energy in the scintillator since the range of the recoil proton is typically much less than the dimensions of the detector. Although many materials are available as scintillation detectors, the most commonly used materials are organic solvents and plastics that have incorporated an organic scintillant.

Once a light pulse is produced in the scintillator, a photomultiplier tube (PMT) is used to detect the light. In a PMT, the photoemission of electrons from light passing through a semitransparent photocathode creates an electrical charge that is then amplified. The amplification takes place inside the PMT as the electrons emitted from the photocathode are collected in an electron multiplier. The electron multiplier uses a series of high-voltage dynodes to accelerate the electrons and create secondary electron emissions that are

accelerated by the next dynode in the series. After a series of accelerations, the charge is collected on an anode. The typical gain of such a multiplier is about 10^6 or 10^7 .

7.2 Efficiency

If only elastic proton scattering is considered, the intrinsic efficiency $\mathcal{E}_{\text{scattering}}$ of a neutron detector is

$$\mathcal{E}_{\text{scattering}} = 1 - \exp(-N\sigma_s t), \quad (12)$$

where σ_s is the (n,p) scattering cross section, N is number density of hydrogen, and t is the thickness of the detector. The efficiency is further curtailed by the minimum light pulse threshold of the PMT and electronics. To better estimate the efficiency, we need to know what the light output distribution is for a monoenergetic neutron beam incident on a scintillation detector.

The light output, as a function of energy, for heavy charged-particles in an organic scintillator is nonlinear. In fact, for many organic scintillators the light output L as a function of energy is

$$L = kE^{3/2}, \quad (13)$$

where k is a constant. Since the scattering cross section as a function of recoil energy dN/dE is a constant for monoenergetic incident neutrons, the light output distribution is

$$\frac{dN}{dL} = \frac{dN/dE}{dL/dE} = \frac{\text{constant}}{\frac{3}{2}kE^{1/2}} = k'L^{-1/3}, \quad (14)$$

where k' is a proportionality constant (see Figure 27). Given this distribution, when a threshold L_T is set below the maximum light output L_0 , the counting efficiency is

$$\mathcal{E}_{\text{counting}} = 1 - \left(\frac{L_T}{L_0}\right)^{3/2} = 1 - \frac{E_T}{E_n}. \quad (15)$$

The total efficiency is the product of the two, $\varepsilon = \varepsilon_{\text{scattering}} \varepsilon_{\text{counting}}$. The solid curve in Figure 28 shows the detector efficiency as a function of neutron energy as calculated using equations 12 and 15.

To make the efficiency calculation more accurate we also must consider the pulse-height resolution of the detector. This has the effect of rounding off the end of the uniform differential energy distribution dN/dE . If we assume the detector's pulse-height resolution has a gaussian dependence with a width σ ,

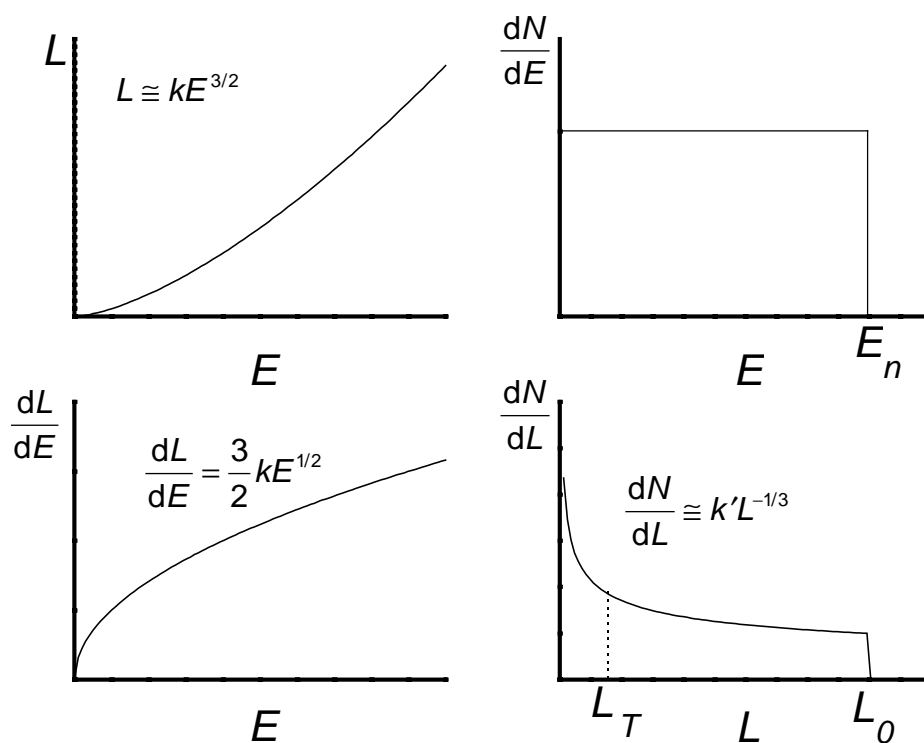


Figure 27 - The two basic contributions to the light output distribution for a monoenergetic neutron beam incident on a detector (from Knoll, ref. 27).

then the differential light output becomes

$$\frac{dL}{dN} = \frac{\frac{1}{\sigma\sqrt{2\pi}} \int_0^{E_n} \exp\left(-\frac{(E-E')^2}{2\sigma^2}\right) dE}{\frac{3}{2}kE^{1/2}}. \quad (16)$$

Other, more subtle, effects that influence the efficiency are multiple scattering and edge effects. For large volumes of scintillator, the possibility of multiple scattering must be considered. For smaller scintillator volumes, edge effects can significantly effect the efficiency. Edge effects refer to a decrease in the efficiency created by recoil protons near the edge of the detector escaping from the scintillator before they deposit enough energy to be detected. All of these effects are included in the code TOTEFF, and are used to calculate the efficiency of right-cylindrical detector where neutrons are incident to the end of the cylinder. Figure 28 also shows the results of the TOTEFF code. The triangle data points represent the efficiency from (n,p) scattering, and the square data points represent to the total efficiency for the detector.

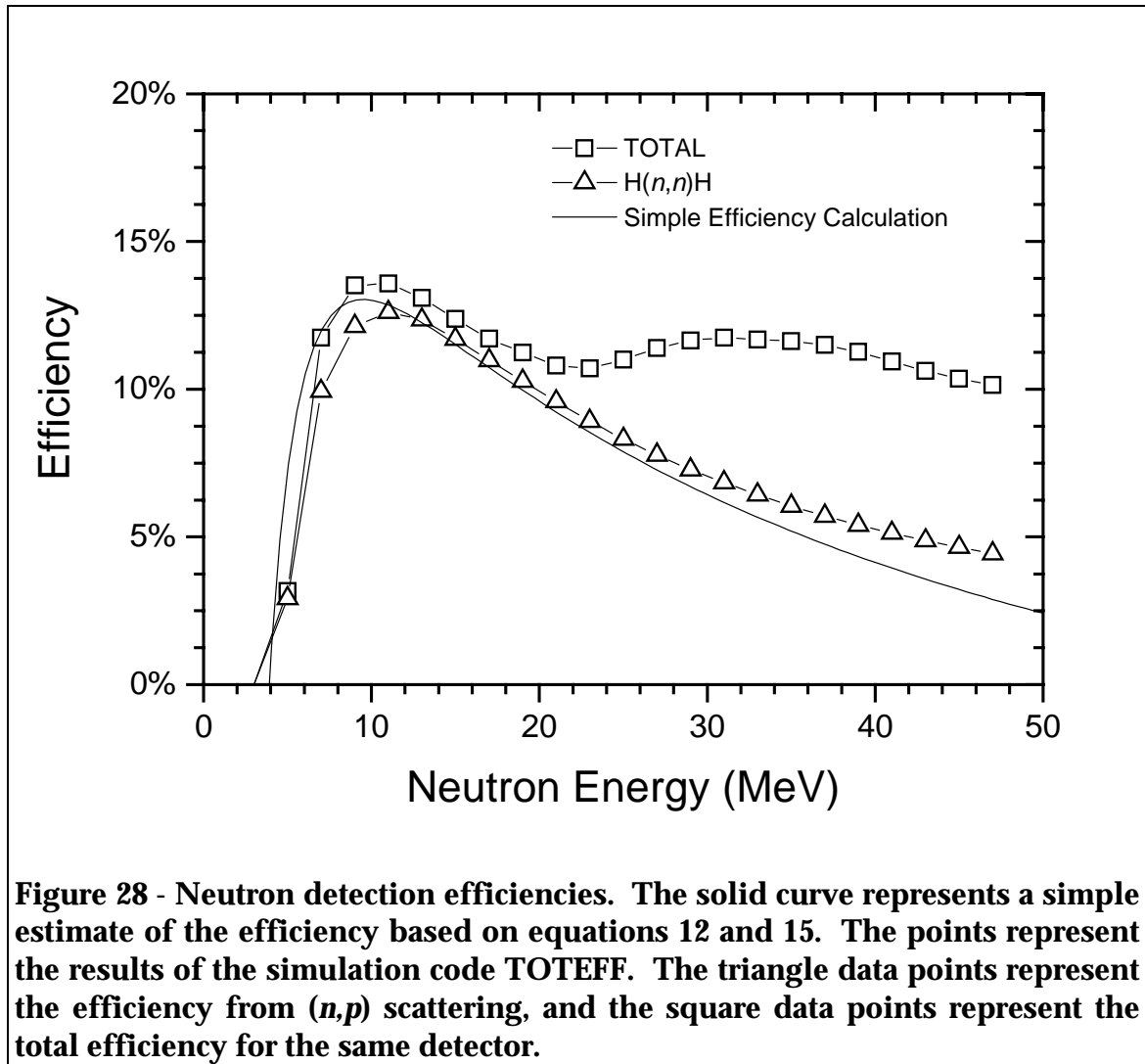


Figure 28 - Neutron detection efficiencies. The solid curve represents a simple estimate of the efficiency based on equations 12 and 15. The points represent the results of the simulation code TOTEFF. The triangle data points represent the efficiency from (n,p) scattering, and the square data points represent the total efficiency for the same detector.

7.3 Time-Of-Flight Resolution

Determining the neutron's energy by measuring the time the neutron takes to travel a known distance is called the time-of-flight (TOF) method. When using TOF, five factors contribute to the energy resolution.

1. The rise time of the light pulse in the scintillator.
2. The intrinsic time resolution of the electronics.
3. The scintillation light intensity.
4. The collection efficiency of the available light.
5. The thickness of the scintillator.

The first three factors are characteristics of the scintillator and electronic equipment available. The last two factors are properties of the detector's design.

The light pulse arrives at the PMT as a series of photons spread out over some time interval. The electronics used to time the neutron requires a logic pulse that is generated when a sufficient number of photons have arrived at the PMT to surpass some threshold. (The threshold could be one photon, but the quantum efficiency of the photocathode surface is not unity, so the time pulse might not correspond to the first photon that arrives at the photo-cathode surface.) Therefore, the time of the logic pulse relative to the actual scintillation event can vary depending on the statistics associated with the number of required photons to trigger the logic pulse. A more luminous pulse will create a higher density of photons-per-unit-time, thus increasing the time resolution.

In organic liquid and plastic scintillators light is emitted isotropically. For very large volumes of scintillator, this can lead to very different path lengths for the light reaching a PMT. Since the number of direct photons reaching the PMT drops off as $1/r^2$, most of the light collected by the PMT will have scattered from multiple sides of the detector before reaching the PMT. This uncertainty in the photon's flight path can add to the uncertainty in the true start time of the scintillation pulse. This effect must be considered when studying the time resolution of the detector; it can also be exploited to help correct for the fifth and final effect on the time resolution in special cases.²⁸

The final contribution to a detector's time resolution comes from the finite time it takes a neutron to pass through the detector. Figure 29 shows a schematic diagram of our rectangular scintillator detector some distance from a neutron source. The scintillator is viewed at both ends by PMTs. As a neutron penetrates

the scintillator, it has a uniform scattering probability as a function of distance into the scintillator. Since the PMTs are unable to locate the position of the scintillation in the z direction, there is an uncertainty Δs in the distance s from the source to the scattering event. It is useful to express this uncertainty in terms of a time uncertainty, $\Delta t = t\Delta s / s$, related by the neutron's velocity, $v = s / t$. Then, for a given thickness of detector, the absolute time resolution depends on the flight time of the neutron through the scintillator, and therefore on the neutron's energy.

Increasing the detector's thickness reduces the detector's time resolution, but it increases its efficiency. The thickness chosen for a detector is therefore a compromise between the desired efficiency and the required energy resolution. It is often best to choose a thickness that creates a Δt is comparable to the other time resolution characteristics.

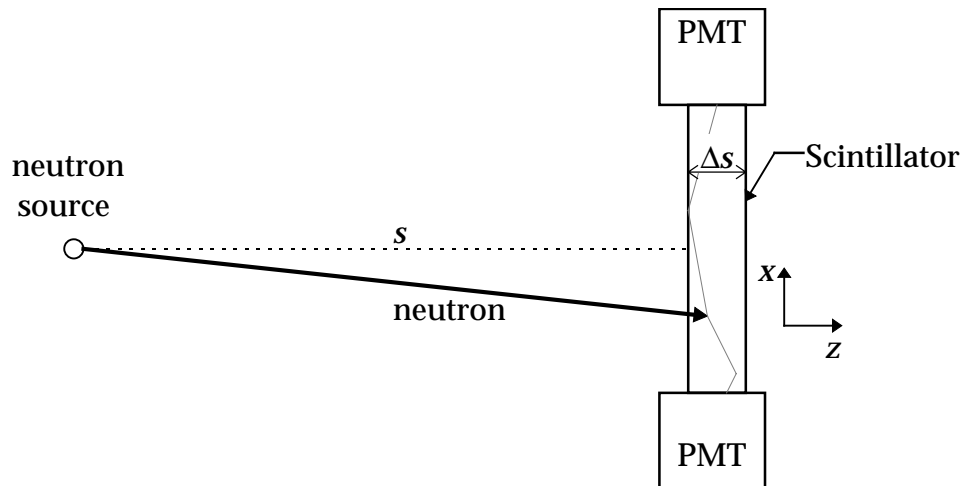


Figure 29 - A schematic drawing of a neutron being detected in a long scintillator cell, perpendicular to the neutron's direction.

If the neutron's energy is to be determined by its TOF over a given flight path,

$$E_n = \frac{1}{2} m \left(\frac{s}{t} \right)^2, \quad (17)$$

and there is an uncertainty in both the flight path Δs and the time Δt ; then the uncertainty in the neutron's energy is

$$\sigma_E^2 = \sigma_s^2 \left(\frac{\partial E}{\partial s} \right)^2 + \sigma_t^2 \left(\frac{\partial E}{\partial t} \right)^2. \quad (18)$$

Or, expressed as the relative energy resolution,

$$\frac{\sigma_E^2}{E^2} = 4 \left(\frac{\sigma_s^2}{s^2} + \frac{\sigma_t^2}{t^2} \right). \quad (19)$$

It is often difficult to determine the overall time-uncertainty Δt from each of the contributions discussed. Luckily, there is a process by which the overall Δt can be determined. When a TOF spectrum is observed for neutrons from a heavy ion reaction, there is also present a distinct, narrow peak associated with the prompt γ -rays from the reaction. Since the γ -rays move at the speed of light, their transit time through a thin scintillator detector is negligible compared to the neutron's transit time, thus it represents the time uncertainty for the whole system without the added complication of detector's thickness. (The γ -rays emission time does not contribute to the uncertainty since the γ -rays are emitted on the time-scale of electromagnetic nuclear transitions ($\sim 10^{-13}$ ns), very much less than typical laboratory resolution of < 1 ns.) Using the width of this γ -ray peak and the given detector thickness, we can determine the relative energy resolution dE/E .

7.4 Pulse Shape Discrimination

Proton recoil scintillation detectors are sensitive to more than just neutrons. Typically, a large background of γ -rays and cosmic-rays is present during an experiment. A few possible methods exist for managing these background radiations. One such method is to raise the threshold level of the detector. Most γ -rays come from nuclear transitions and their energies are therefore limited to the binding energy, about 8 MeV. If the threshold is set

above this level, most of the γ -rays can be eliminated. Although cosmic-rays are usually high energy muons, the energy they deposit in a scintillator depends on the length of their flight path through the scintillator. For scintillation detectors with small enough dimensions, the threshold can be set above the maximum possible energy deposited to eliminate the cosmic-ray background. Unfortunately, as can be seen from equation 15, the higher the threshold, the lower the neutron detection efficiency.

Another method of reducing the background is to require the neutron signal to be in coincidence with another signal that is known to be associated with the neutron. This method reduces the so called time-uncorrelated background signals. When the TOF method is used to determine the neutron's energy, a coincidence between two events is always present. While all cosmic-rays are time-uncorrelated, and many γ -rays are time-uncorrelated, there are γ -rays from the reaction that produced the neutron, or secondary reactions. These γ -rays will be correlated in time with neutrons and are harder to eliminate. If the coincident signal is also used as the basis of the TOF measurement, then the width of the coincidence period will determine the possible neutron energies allowed. If it is necessary to measure a large dynamic range of neutron energies, the coincidence period might be so wide as to eliminate the background reduction benefits of a coincidence requirement.

The most useful method of eliminating background events comes from analyzing the electric pulse from the detector. For some scintillators, the shape of the pulse varies according to the specific ionization of the ionizing particle. The light produced by an ionizing particle has two components, a prompt fluorescence and a delayed fluorescence. The prompt fluorescence has a decay constant of a few nanoseconds, whereas the delayed fluorescence has a decay

constant on the order of a few hundred nanoseconds. The proportion of light produced by each of these two components varies according to the specific ionization of the ionizing particle. A lightly-ionizing particle, such as a cosmic-ray or an electron from the Compton scattering of a γ -ray, will produce most of its light in prompt fluorescence. A highly-ionizing particle, such as a recoil proton, will produce a larger fraction of light in the delayed fluorescence for the same amount of total fluorescence as a lightly-ionizing particle.

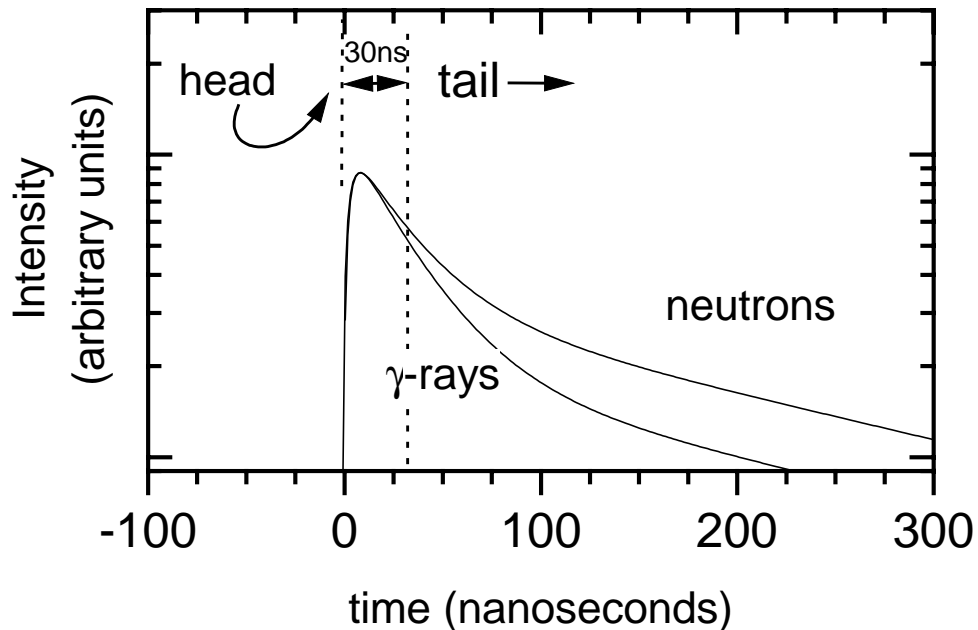


Figure 30 - A representation of the scintillation light output as a function of time for different radiations in organic scintillator NE-213.

Over the years, many procedures have been developed to exploit this property, commonly called pulse-shape-discrimination (PSD). Most methods are able to discriminate between γ -ray and neutron signals for neutron energies above 3 MeV. A method developed at the NSCL uses two ADCs: one integrates the total charge of the pulse, and the other integrates the charge for some fixed time-fraction of the pulse. The fixed time-fraction is usually either the head of

the pulse or the tail of the pulse. Then, by comparing the charge in this fraction of the pulse to the total charge in the pulse, we can determine what particle created the pulse.

To quantitatively discuss the PSD property of a scintillator, we calculate the so called Figure-Of-Merit (FOM). The FOM is defined as a function of the total integrated charge. If we illuminate a detector with both γ -rays and neutrons and record the charge in the tail of the pulse, we obtain a histogram as shown in Figure 31. The FOM is then defined as the separation between the two centroids of the peaks divided by the sum of the FWHMs of the two peaks. We consider a FOM above 1 to be acceptable.

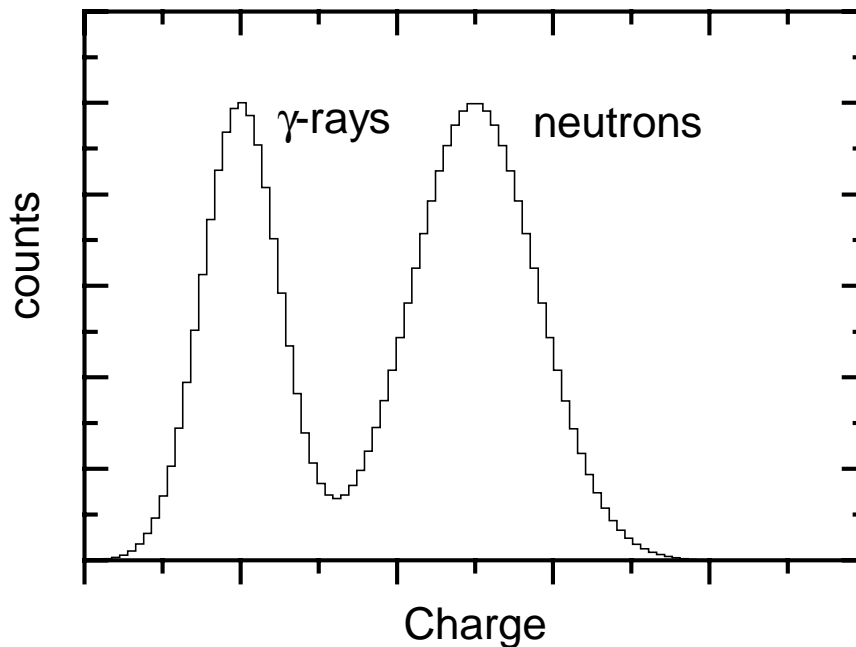


Figure 31 - The integrated charge in the tail of the pulse for neutron and γ -ray signals, when the total integrated charge for both signals is the same. The FOM for this spectrum is 1.35.

8 *Neutron Wall Array Characteristics*

The *Neutron Wall Array* consists of two individual detector arrays, each consisting of 25 individual detector cells. The area of each array is 2x2 m²; the inactive area is less than 12 percent of the total area. The scintillator used in the array is NE America's NE-213.* The total scintillator volume is 500 liters. Currently, the *Neutron Wall Array* resides in the NSCL's N4 vault. The overall time resolution of the array has been shown to be about 1 ns FWHM. The position resolution along the length of the cell approaches 7 cm FWHM for neutrons depositing greater than about 10 MeV of energy in the detector. This position resolution is comparable to the 7.62 cm height of the individual detector cells. Using our PSD circuit, described in section 9.1, we have obtain excellent PSD for neutrons down to 3 MeV of energy.

Section 8.1 describes the general physical characteristics of the *Neutron Wall Array*. Section 8.2 briefly describes the measured time resolution of the array. Section 8.3 discusses measurements of the position resolution along the length of a cell. Finally, section 8.4 demonstrates the PSD properties of a cell.

8.1 *Size, Configuration and Construction*

The elements that form the array are 2-meter long Pyrex cells filled with the liquid, organic scintillator NE-213. Two PMTs view the cell from both ends. Figure 32 shows a drawing of one cell. The outside of the Pyrex cell is not treated with any reflective or specular coating; this allows total internal reflection to be the means by which the light is channeled through the cell to the PMTs. Monte carlo simulations of the detector show that approximately 20 percent of the light from an event reaches each PMT; the other 60 percent of the light

* NE America was recently purchased by Bicron Corporation of Newbury, Ohio.

escapes from the cell because the angle it forms with the surface normal of the glass is less than the critical angle. Figure 33 is a photograph taken looking through one end of a cell; the NSCL logo was placed at the other end. Multiple reflections of the logo in the sides of the detector are visible. (The cell used for the photograph had a square cross section and was not one of the cells used in the *Neutron Wall Array*, which have a rectangular cross section.)

The Pyrex cells were custom made for this application and have a wall thickness of $\frac{1}{8}$ inch. To make the cell, we purchased custom Pyrex tubing made to our cross sectional dimensions and at least 85 inches long. The tubing arrived from the manufacturer with the ends of the tube open. The Michigan State University Scientific Glass Blowing Shop then closed the ends of the tubes so that they could be coupled to the PMTs. The PMT used was a new product of Philips Photonics, model XP4312B/04. This model is a fast, 12-stage PMT with a 3 inch photocathode surface. In order to make use of the whole photocathode surface, the end of the tubes were closed off with a 3 inch circular Pyrex disk. Closing the tubes was a two step process. First, a cylindrical Pyrex tube, 3-inches in diameter, was fused onto the end of the rectangular tube. The cylindrical tube was then trimmed at the nearest point to the junction where the cross section became circular, about 1 inch. The second step was to fuse a circular plate, 3-inches in diameter, onto the cylindrical tube. Except for cleaning, the surfaces of the cells required no further polishing or finishing and were used as they came from the manufacturer.

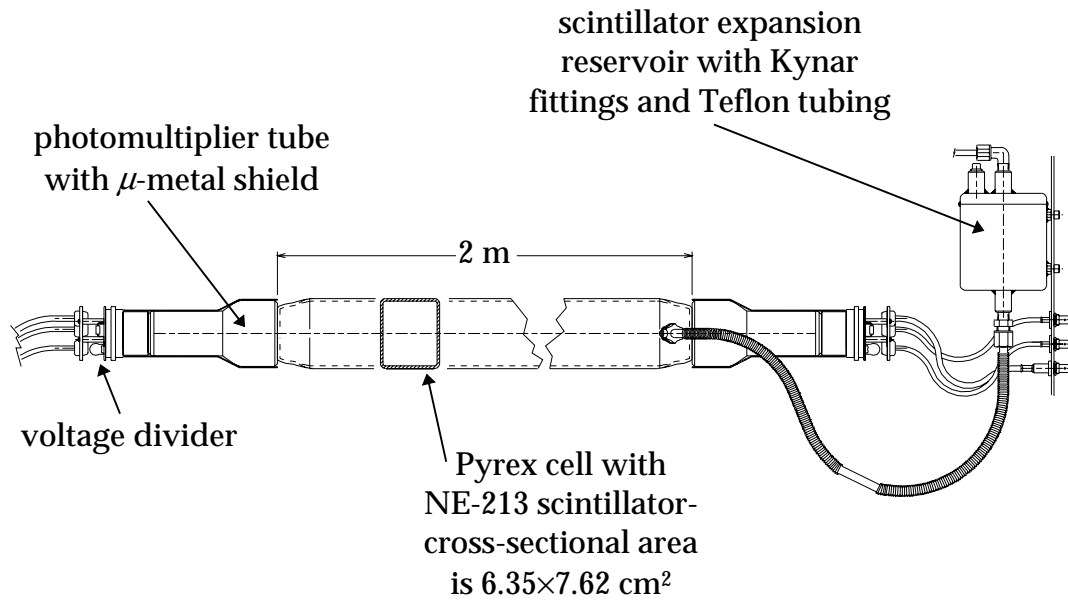


Figure 32 - A drawing of an individual detector cell from the *Neutron Wall Array*.

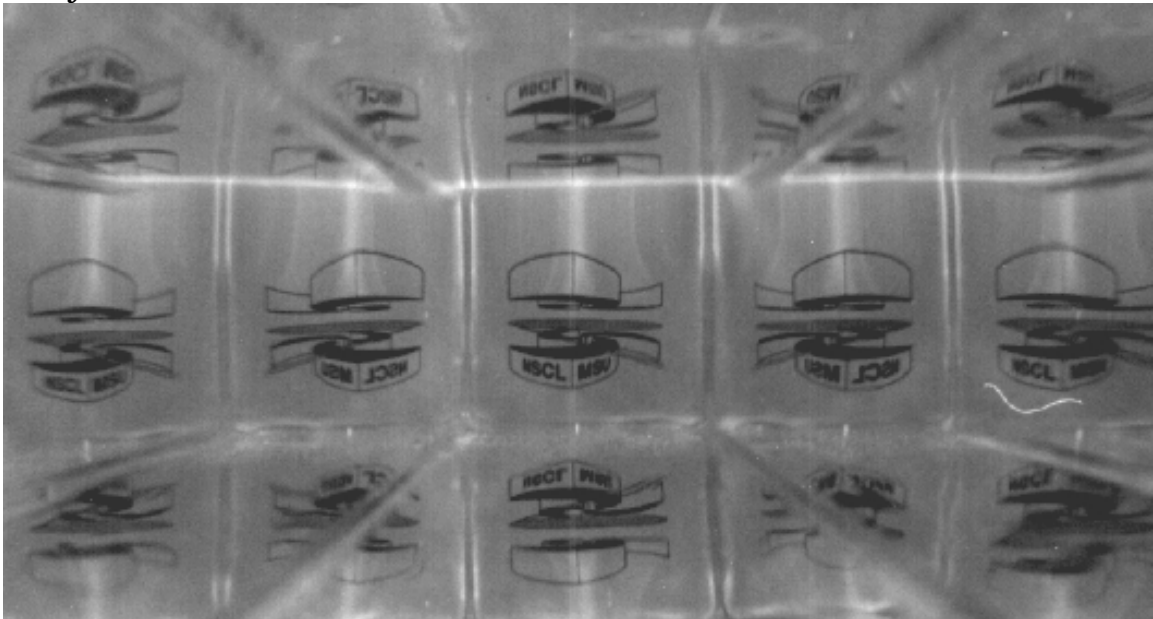


Figure 33 - A photograph looking lengthwise through a cell. The NSCL's logo was placed at the opposite end of the cell. Only the center image is real, the others are all reflections from the sides of the cell.

The PMTs are attached to the end of the cell with an optically clear epoxy, BC-600. A special jig was designed to hold the PMT and cell in place for the 24 hours the epoxy requires to cure. Surrounding each PMT is a μ -metal shield; this prevents any extraneous magnetic fields from interfering with the operation of the PMT. We designed a simple passive voltage divider for our PMTs. Both the anode and last dynode signals are used by the acquisition electronics. Figure 34 shows the voltage divider's circuit. The total resistance of the resistor chain was selected to use the maximum current available from the power supply. Having a large current flow through the resistor chain helps maintain the linearity of the signal amplification.

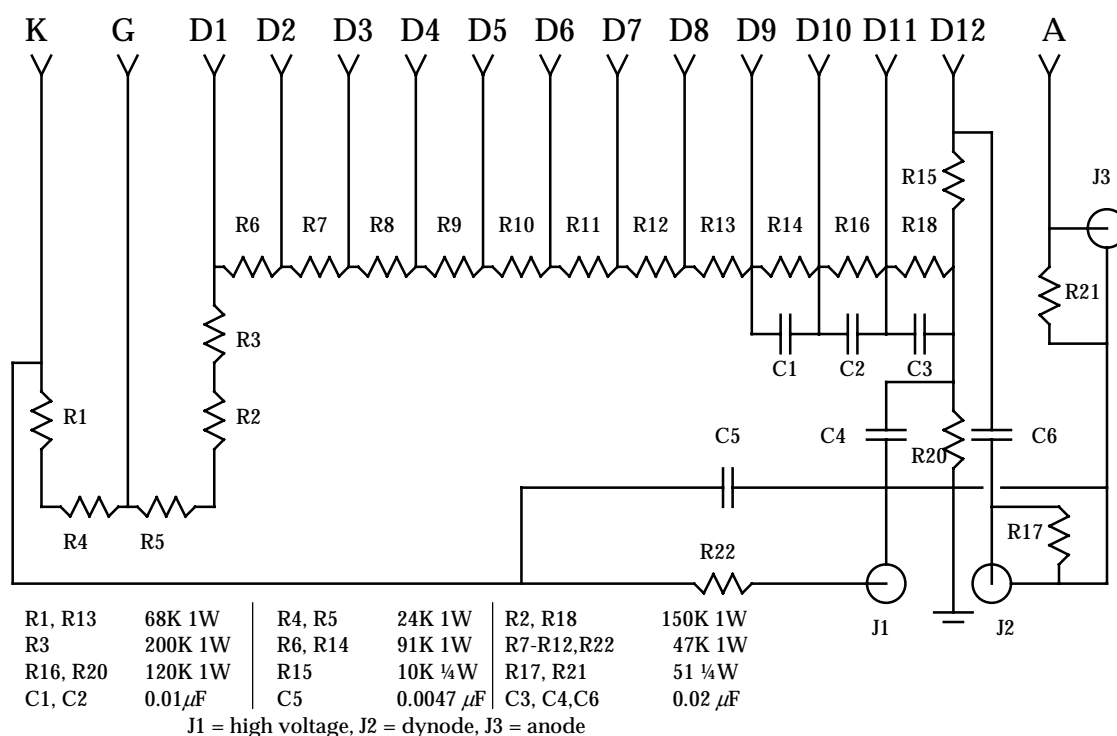


Figure 34 - Schematic drawing of the passive voltage divider used on the XP4312/04 PMT.

Once this cell is sealed, a small ($\frac{1}{4}$ inch diameter) tube with a glass-Kovar seal is fused onto the cell. The cell is cleaned and filled through this small tube. The tube is connected to an aluminum can by a corrugated Teflon tube. This can

is a thermal expansion chamber for the scintillator, since the scintillator's coefficient of expansion is greater than the glass'. The scintillator, NE-213, will corrode most plastics; therefore, all of the tubing and fittings used are made of Teflon or the resin Kynar, both being chemically resistant to the scintillator. Once the can is in place, a small ($\frac{1}{8}$ inch OD) Teflon tube was inserted through the can and corrugated Teflon tube into the cell (see Figure 36). The scintillator was then pumped through this small tube, filling the cell.

The PSD properties of NE-213 can be degraded by the presence of dissolved oxygen in the scintillator. To remove any oxygen that might have been introduced when the cell was filled, we passed dry nitrogen gas throughout the volume of the scintillator for about 1 hour. We call this process bubbling. The nitrogen gas will dissolve into the scintillator and force out any dissolved oxygen gas. The nitrogen gas was delivered into the cell through the small Teflon tube that was used to fill the cell. After the bubbling was complete, the small Teflon tube was removed and the aluminum can was sealed with a stainless-steel pipe-plug.

After the cells were completed, they were inserted into the array. The array was supported by a large aluminum frame. In case of a catastrophic accident, the bottom of the frame has a large catch-basin capable of containing the scintillator volume from all 25 cells in the frame. The sides and top of the frame are covered with aluminum plates and made light-tight with opaque caulking. The front and back of the frame are covered with a removable aluminum sheet attached at the edges to another aluminum frame. The aluminum sheet is $\frac{1}{32}$ of an inch thick, providing very little material for unwanted neutron scattering. A cutaway drawing of the complete assembly is shown in Figure 35.

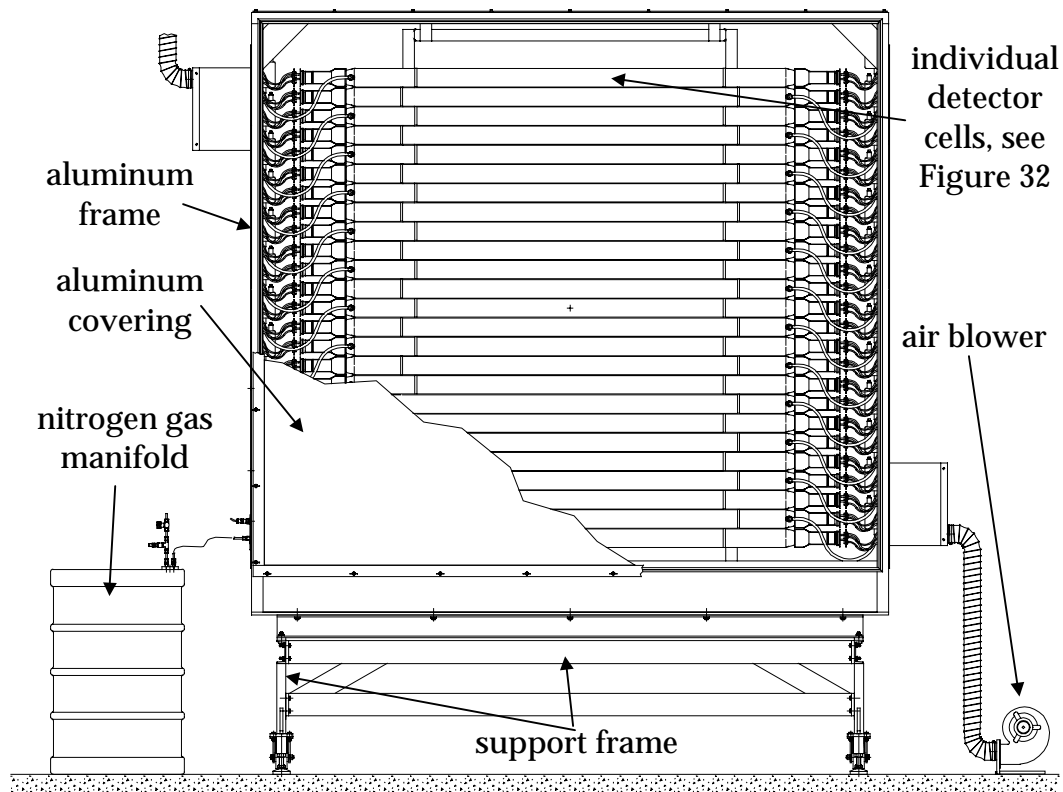


Figure 35 - A mechanical cutaway drawing of one of the *Neutron Wall Array*.

The cells are attached with special brackets to two, hollow, 2-inch square, aluminum posts in the center of the frame. The cells are strapped to the bracket with a 20 mil thick stainless-steel band. To allow for small variations in the surface of the cell, the cells are spaced $\frac{1}{8}$ inch apart. Once a cell is in place, the aluminum can is unsealed and attached to a nitrogen gas manifold to provide a greater gas volume for expansion.

The inside of each of the aluminum frames is painted flat black, and when the front and back cover sheets are in place, the aluminum box becomes light-tight. By making the frame light-tight, we have avoided the difficulty of making the 50 cells light-tight individually. To prevent cross talk between the cells—that

is light from one cell entering a neighboring cell—a piece of black paper is inserted between the cells.

Other miscellaneous hardware associated with arrays included a gas monitoring system, an air blower, and a fiber optic timing system. The gas monitor detects high levels of xylene gas; xylene is the solvent for the scintillator. This gas is explosive and the liquid has a flash point of 97° F. The gas monitor is connected to the laboratory's electronic control system. If the gas monitor detects a dangerous level of xylene, it alerts the control system which shuts down the high-voltage system powering the PMTs. Each of the voltage dividers produces 5 W of heat; to help keep the inside of the frame cool, each frame has an air blower. To keep the frames light-tight, the blowers are connected to the frame through light-tight baffles. The fiber optic system is used for various timing purposes and is discussed in Section 9.2.2.

Each of the two arrays is supported on a steel frame that centers the array about the beam height in the N4 vault, where the *Neutron Wall Array* is used. The steel frames are on wheels and can be moved about the vault. The frames are also designed to fit into each other so that the arrays can be placed front to back, with a minimum distance between the cells of about 1 foot.

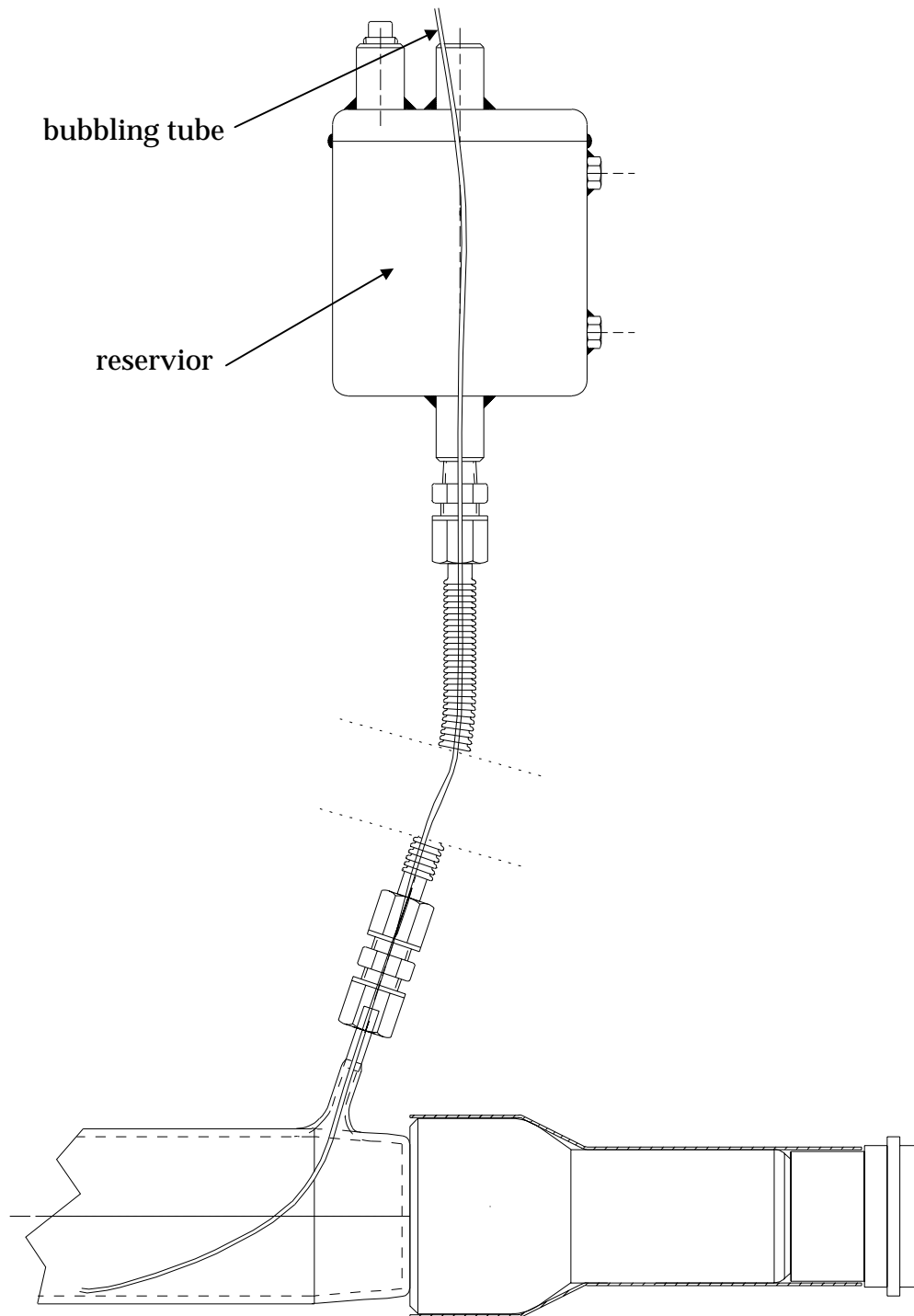


Figure 36 - A schematic drawing of the bubbling procedure for a completed cell. For about 1 hour, dry nitrogen gas is blown through the small Teflon tube that is fed through the reservoir into the cell.

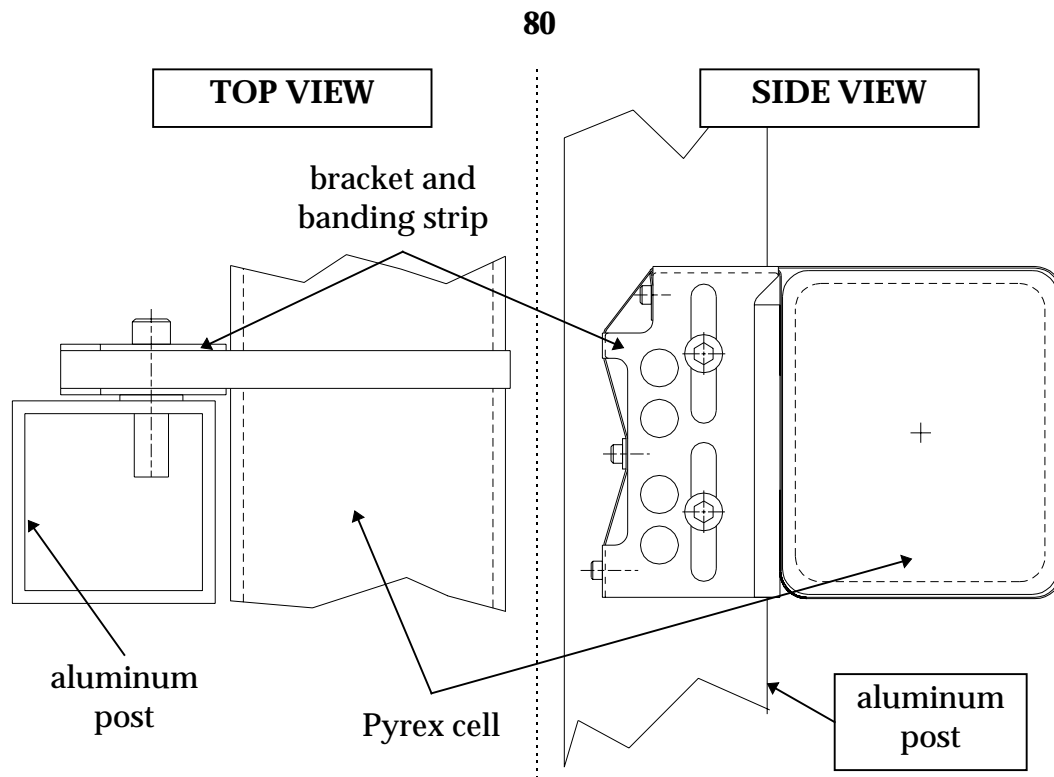


Figure 37 - Top and side view of the cell-mounting bracket.

8.2 Time-Of-Flight Energy Resolution

Section 7.3 describes the various contributions to the detector's time resolution and how they effect the neutron's energy resolution. A good estimate of the overall time resolution can be obtained from the prompt γ -ray peak in a TOF spectrum. From the γ -ray peak shown in the upper pane of Figure 11 and the γ -ray peak shown in Figure 38 (from reference 29), the time resolution of the detector array is about 1 ns. Using this value, the width of the cells and equation 19, we show in Figure 39 the relative energy resolution for various flight paths and neutron energies.

8.3 Position Sensitivity

I have a position calibration of 7.65 cm/ns.

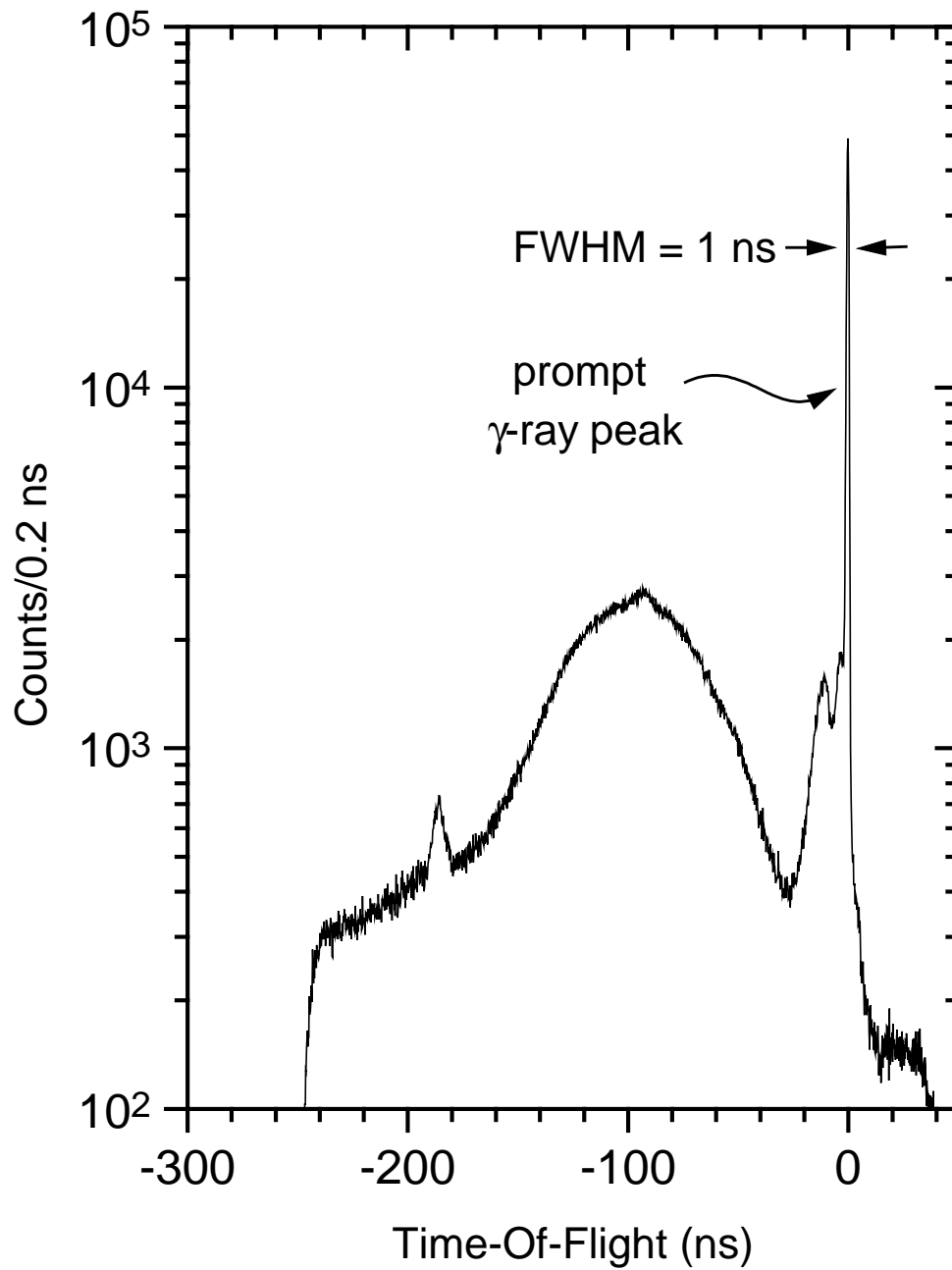


Figure 38 - Neutron and γ -ray TOF spectrum from Ar on Ho at 25 MeV/nucleon. The prompt γ -ray peak from the reaction is an indication of the overall time resolution of the *Neutron Wall Array*.²⁹

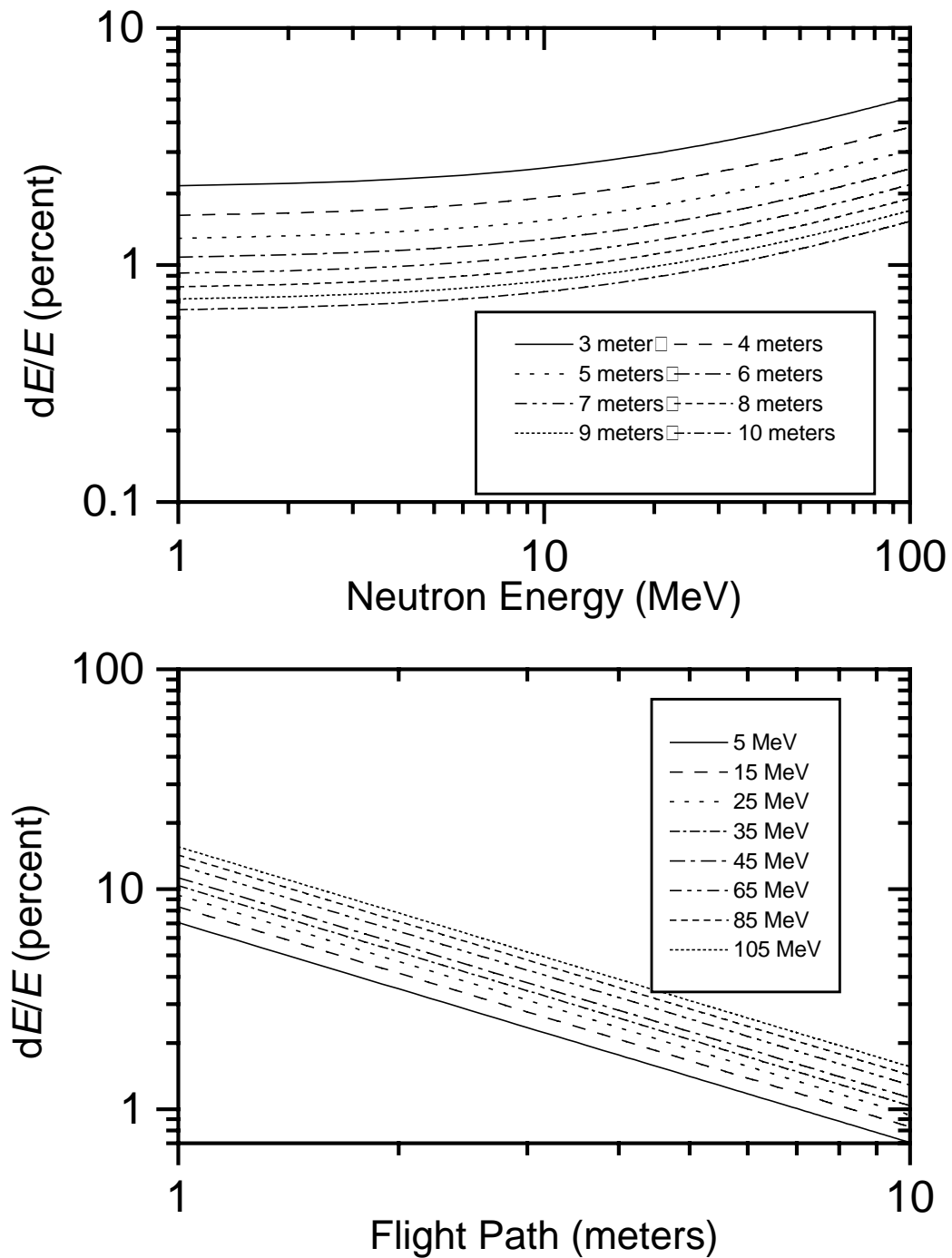


Figure 39 - The relative energy resolution for the *Neutron Wall Array*. The upper pane shows the resolution as a function of neutron energy, for various flight paths; the lower pane shows the resolution as a function of flight path for various neutron energies.

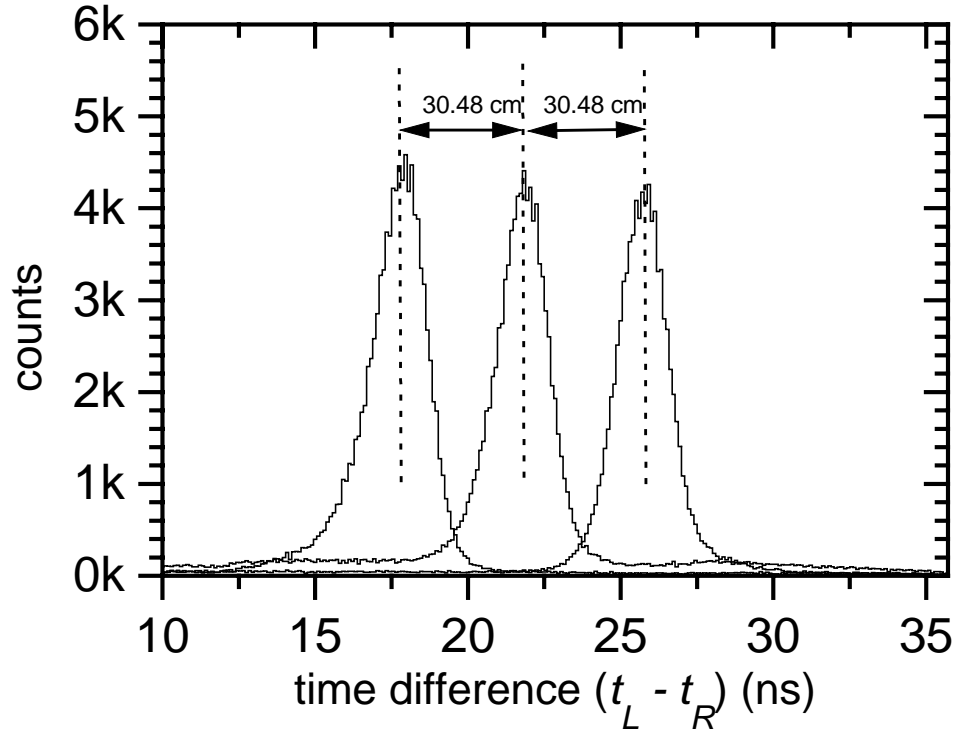


Figure 40 - Time difference measurement of a collimated ^{60}Co source at three different positions. The positions are separated by 1 ft (30.48 cm).

8.4 Pulse Shape Discrimination

When we began researching the possibility of using long cells of liquid scintillator, our primary concern was over the quality of the pulse-shape-discrimination we could achieve. PSD methods improve with increased light output, therefore we were concerned with what the low energy cut-off is for acceptable n/ γ -ray discrimination. We found that combining the information from the two PMTs greatly increases our PSD resolution, and that we have complete n/ γ -ray separation for recoil protons with as little energy as 3 MeV. Given a 30 MeV neutron energy, as used in Sackett's experiment, and using 3 MeV as a threshold, then the counting efficiency (from equation 15) is $\epsilon_{\text{counting}} = 1 - \frac{3}{30} = 90\%$. We consider this efficiency acceptable.

As described in section 7.4, we can distinguish between neutron signals and γ -ray signals by comparing the total integrated charge of the pulse to the integrated charge in either the head or the tail of the pulse. Currently, the *Neutron Wall Array* uses a circuit we have developed to provide a signal proportional to the head of the pulse, called QFAST. Both the QFAST signal and the total integrated charge, QTOTAL, are dependent on the distance of the event from the PMT because of light attenuation by the scintillator. To compensate for this, we create a position-independent QFAST/QTOTAL signal by taking the squareroot of the product of the two QFAST/QTOTAL signals from the two PMTs. For the rest of this section, QFAST/QTOTAL refers to the position-independent values. In Figure 41 we show the QFAST signal plotted against QTOTAL. Since QTOTAL is proportional to the light output, it can be related to either the Compton scattered electron energy or the recoil proton energy. It is easier to represent QTOTAL in terms of the equivalent electron energy than in terms of the recoil proton energy since the electron's light output is linearly dependent on its energy and the proton's light output varies as its energy to the three-halves power (equation 13).

Figure 42 shows the QFAST signal for various values of QTOTAL, which is again represented in terms of electron equivalent energy. It is clear from the figure that we have achieved excellent neutron/ γ -ray discrimination to below 1 MeV electron equivalent energy, or a recoil proton energy of about 3 MeV. By fitting a double gaussian curve to these data, we can determine the figure-of-merit. In Figure 43 we show the FOM as a function of electron equivalent energy.

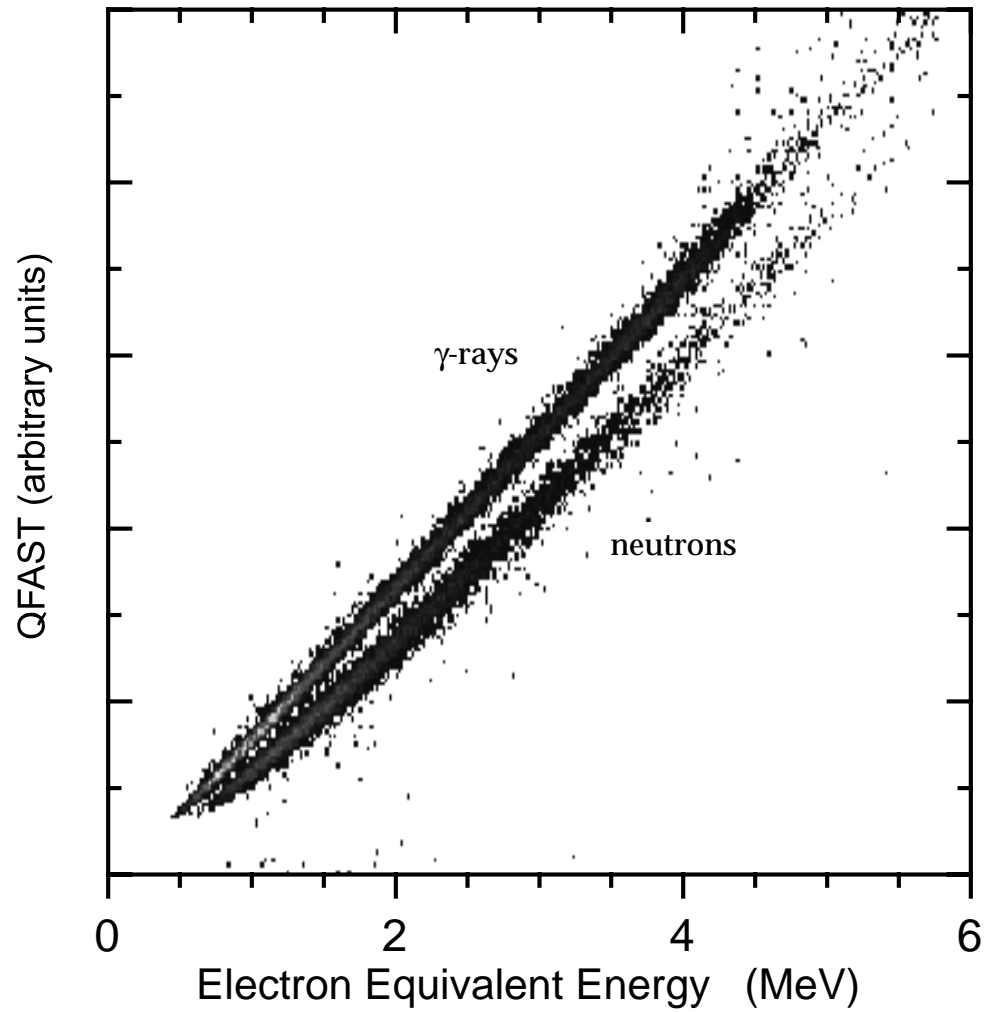


Figure 41 - A PSD spectrum from a cell in the *Neutron Wall Array*. The neutrons and γ -rays are from a PuBe source placed a few feet perpendicularly from the center of the cell.

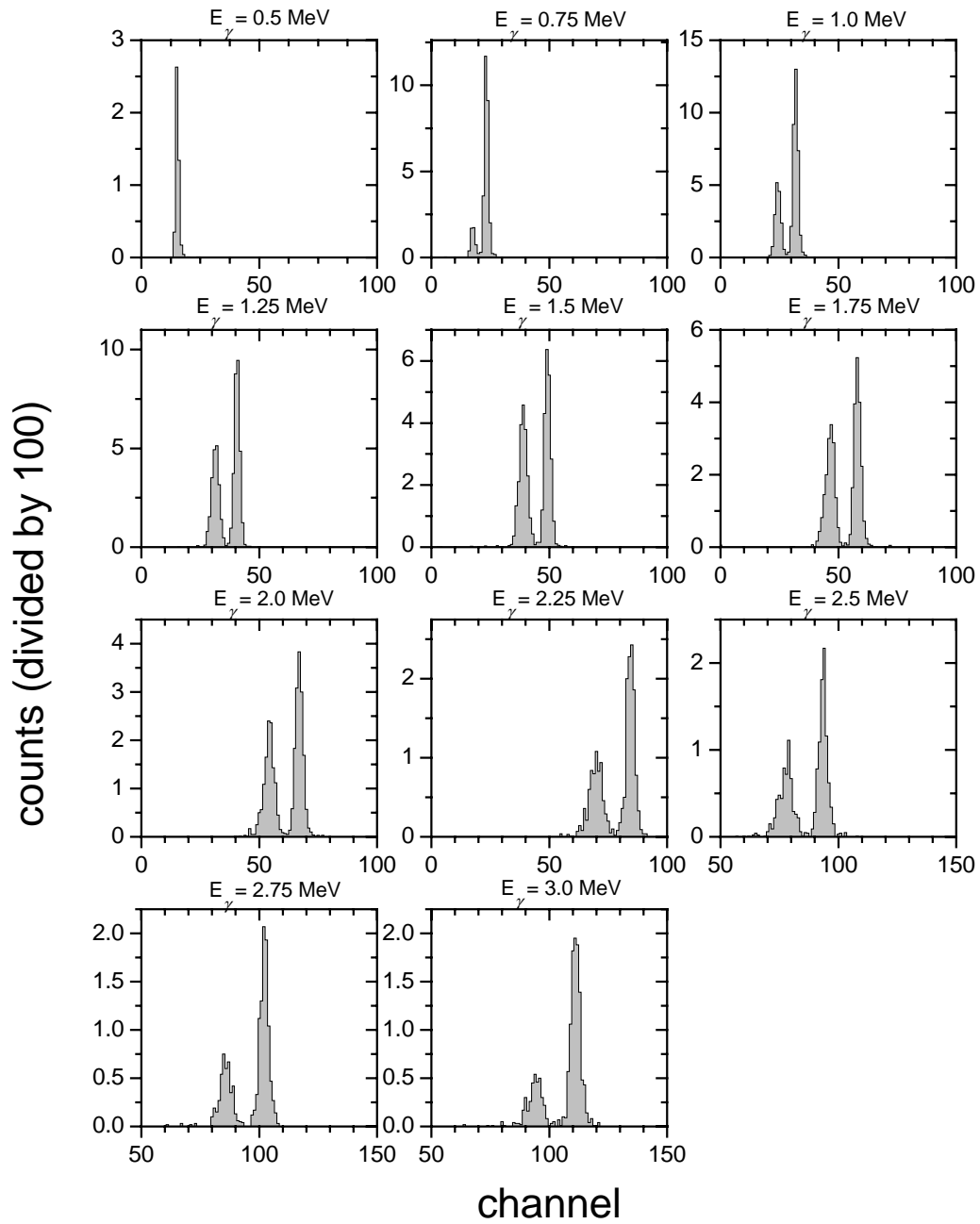


Figure 42 - Individual QFAST spectra for various Q_{TOTAL} values. The Q_{TOTAL} values expressed in terms of equivalent electron energy.

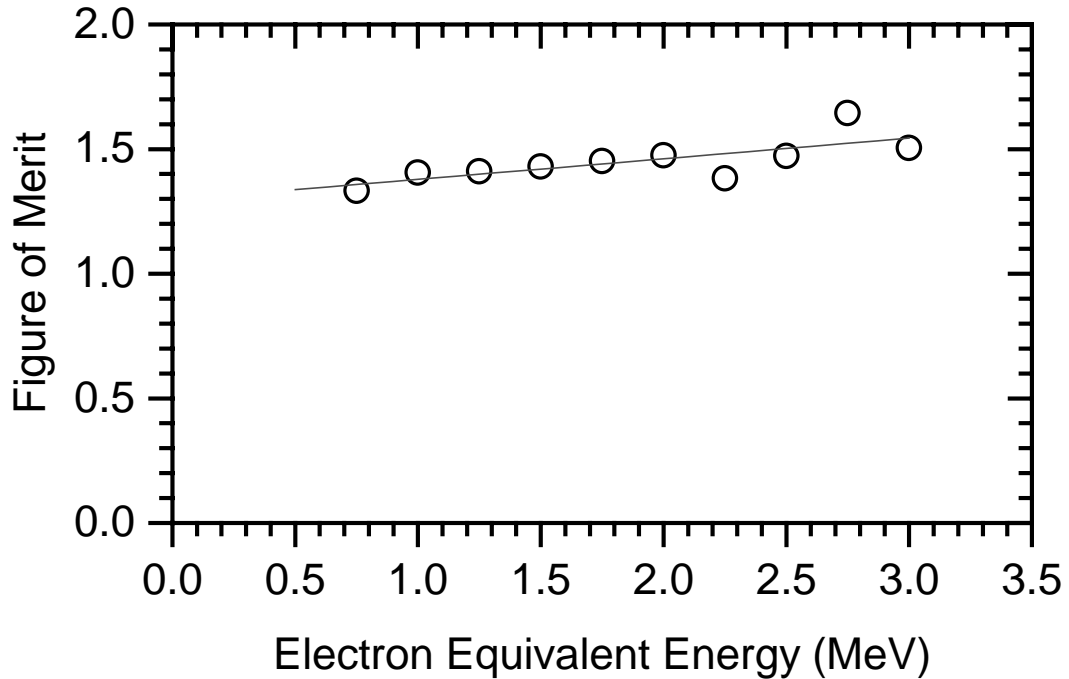


Figure 43 - The figure-of-merit from Figure 42 as a function of the equivalent electron energy.

9 Operation

The following sections deal with various aspects of operating the *Neutron Wall Array*. Of primary interest is the electronics system used to obtain the necessary information from the cells in the array. Also of interest are the two primary calibrations that must be performed when the *Neutron Wall Array* is used.

9.1 Electronics

For every event in the *Neutron Wall Array* we must know the time of the event with respect to some reference signal (e.g., the time of a fragment event or the cyclotron's RF signal), the position of the event along the cell, and the energy of the recoil proton. We must also have some means of identifying whether the event was from a neutron or from a γ -ray or cosmic-ray. By measuring the time

between some reference signal and each of the PMTs on a cell, we can find both the time of the event and the position of the event along the cell. If t_L is the time between the reference signal and the left PMT tube, and t_R is the time between the reference signal and the right PMT tube, then to first order, the time-of-flight of the event is

$$\text{TOF} = \frac{t_L + t_R}{2}, \quad (20)$$

and the position from the center of the cell is

$$\text{position} = k(t_L - t_R), \quad (21)$$

where k is the scale factor between time and distance (see section 8.3). Higher order terms correct for nonlinear effects at the very ends of the cell. We can determine the energy of the recoil proton by integrating the charge of the signal from the PMT, which is proportional to the recoil proton's energy (see section 9.2.1). If we have integrated the total charge of the signal, we can then integrate some portion of the signal to determine whether it was produced by a neutron or a γ -ray (see section 8.4). If there is a large dynamic range in the recoil proton energies, we must also integrate an attenuated charge signal and some portion of the attenuated signal.

Figure 44 shows a simple schematic of the electronics used to obtain this information from a PMT. All of the information is obtained from the two electrical signals produced by the PMT's voltage divider. One signal is a positive-voltage pulse from the last dynode in the multiplier chain and the other signal is a negative-voltage pulse from the anode that collects the charge from the multiplier chain. The dynode pulse is used for the timing signal, and the anode is used for the integrated charge signals. Most timing electronics use negative pulses, so we invert the dynode pulse with a small inductor. This inverted signal is fed into a constant fraction discriminator (CFD). The CFD

produces a fast logic pulse if the voltage of the input signal surpasses a programmable threshold. The logic output of the CFD is then used to start a fast clock. The clock is stopped by the common reference signal. A logical OR of all of the CFD outputs is used to create a gate signal, which controls the charge-to-digital converts, and a trigger signal for the primary trigger logic, which controls the data acquisition computer.

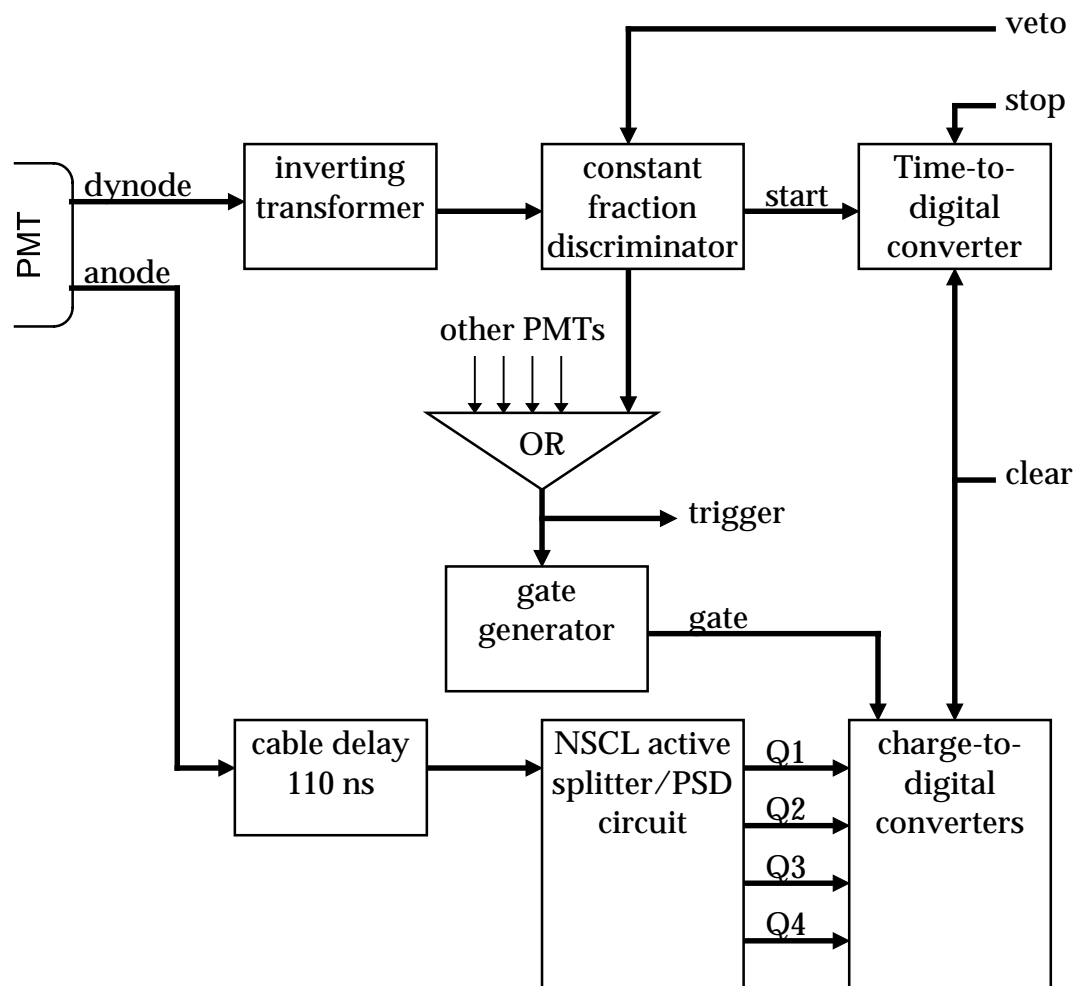


Figure 44 - Basic outline of the processing of the signals from the *Neutron Wall Array*. Q1 through Q4 represent the charge signals: anode, attenuated anode, PSD, and attenuated PSD.

Our traditional method of doing pulse-shape-discrimination³⁰ is shown in the upper part Figure 45. The anode signal is split and fed into two charge-to-

digital converters (QDC). One of the two signals is delayed 30 ns before being fed into the QDC. A gate signal is then timed so that it begins with the start of the delayed signal; the QDC integrates the pulse as long as there is a gate signal. While this method works very well, it is not suited for applications where two or more neutrons must be detected in coincidence. The problem is, if two neutrons arrive at slightly different times, two different gates are required. Unfortunately, most QDC modules have multiple channels controlled by one common gate. A few solutions exist. One solution is to use one QDC module per PMT and only use two channels per module. The high cost of QDC modules makes this solution impractical if a large number of PMTs are involved. Another solution is to use a linear gate module as the input to the QDC, in effect giving each QDC channel its own gate. We prefer not to use this method because of some bad experience we have had with the stability of available linear gates. (This was the method used by Sackett, *et al.*)

While investigating other PSD methods³¹, a suggestion arose for a very simple circuit that would create a pulse proportional to the fast component of anode pulse.³² This pulse could be integrated anytime during the gate period. With this method, we again split the anode pulse into two separate pulses. One of the two pulses is integrated as normal. As long as the gate starts before the pulse, and lasts for approximately 300 ns after the beginning of the pulse, the position of the anode pulse with respect to the gate pulse is arbitrary. The other pulse is used to create the PSD signal. This process is shown in the lower part of Figure 45. The PSD pulse is formed by combining the anode pulse with its reflection from a terminated delay line. The input stages of the Lecroy 2249W QDC have a circuit that prevents the positive part of the pulse from being integrated. Therefore, the integrated charge represents the charge in the first

portion of the pulse. The proportion of the anode pulse that is integrated is controlled by the length of the terminated delay line. A schematic of the process is shown in Figure 45.

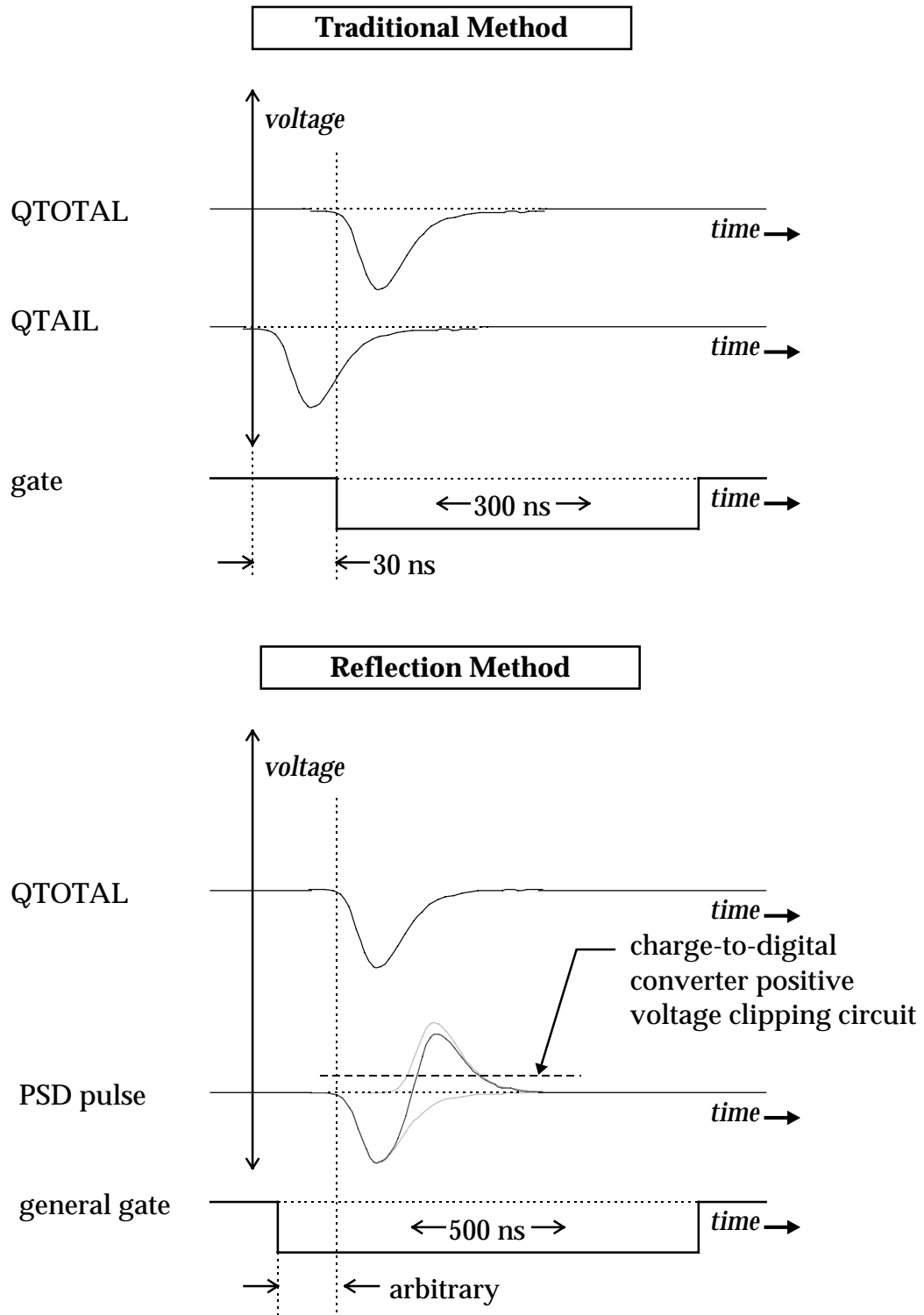


Figure 45 - Pulse shape discrimination methods.



Figure 46 - A simple schematic of the method of producing the PSD signal.

As shown in Figure 46, the reflected pulse could make its way back to the QTOTAL channel of the QDC. To prevent this, and to gain match with the QFAST input, an emitter follower (EF) circuit was inserted before the delay line. Not only does the EF prevent the reflection from entering the whole circuit, it also acts as an active splitter, letting the full charge of the anode be integrated by the QTOTAL QDC channel. Figure 47 shows the exact circuit that we used. A duplicate circuit was used to produce a PSD pulse from an attenuated anode pulse. The 8 ns delay length was found empirically to provide the best neutron/ γ -ray separation.

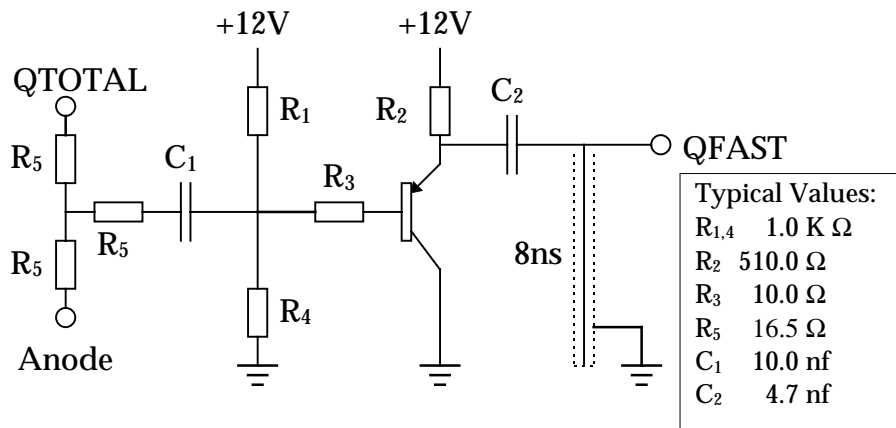


Figure 47 - The circuit used to produce the PSD pulse. The circuit also acts like an active splitter for the anode pulse. The QFAST output is gain matched to the 50 Ω input of the Lecroy 2249W QDC.

The same signal that produces the gate for the QDCs is also used as the Neutron Wall Array trigger for the master trigger logic. The master trigger logic's

job is to coordinate the *Neutron Wall Array* electronics with the rest of the electronics required by the experiment. Such a system is described in section 2.3 and is shown in Figure 12. Typically, the logic is designed to look for a coincidence between the *Neutron Wall Array* trigger and a signal in an auxiliary detector. If such a coincidence is detected, then the data acquisition computer is instructed to read the value of the QDCs and the time-to-digital converts. If the *Neutron Wall Array* triggers, and there is no coincidence with the other detectors in the experiment, then the *Neutron Wall Array* electronics processes a so-called fast clear. This resets all of the QDCs and time-to-digital converts. This is particularly useful because of the very high background counting rate of the wall. With thresholds set to 1 MeV electron equivalent energy, the background counting rate is about 16,000 events per second. By using the fast clear, these events are not processed by the data acquisition computer; that reduces the dead time of the system. Once the computer is activated, a veto signal is issued to all CFDs to prevent events from entering the electronics before the previous event is completely read out. A detailed drawing of the master trigger logic used for the ${}^8\text{Li}(n,\gamma){}^9\text{Li}$ experiment described in PART I is shown in Figure 48. The circled numbers represent timing points; these points are represented on a relative timing diagram shown in Figure 49.

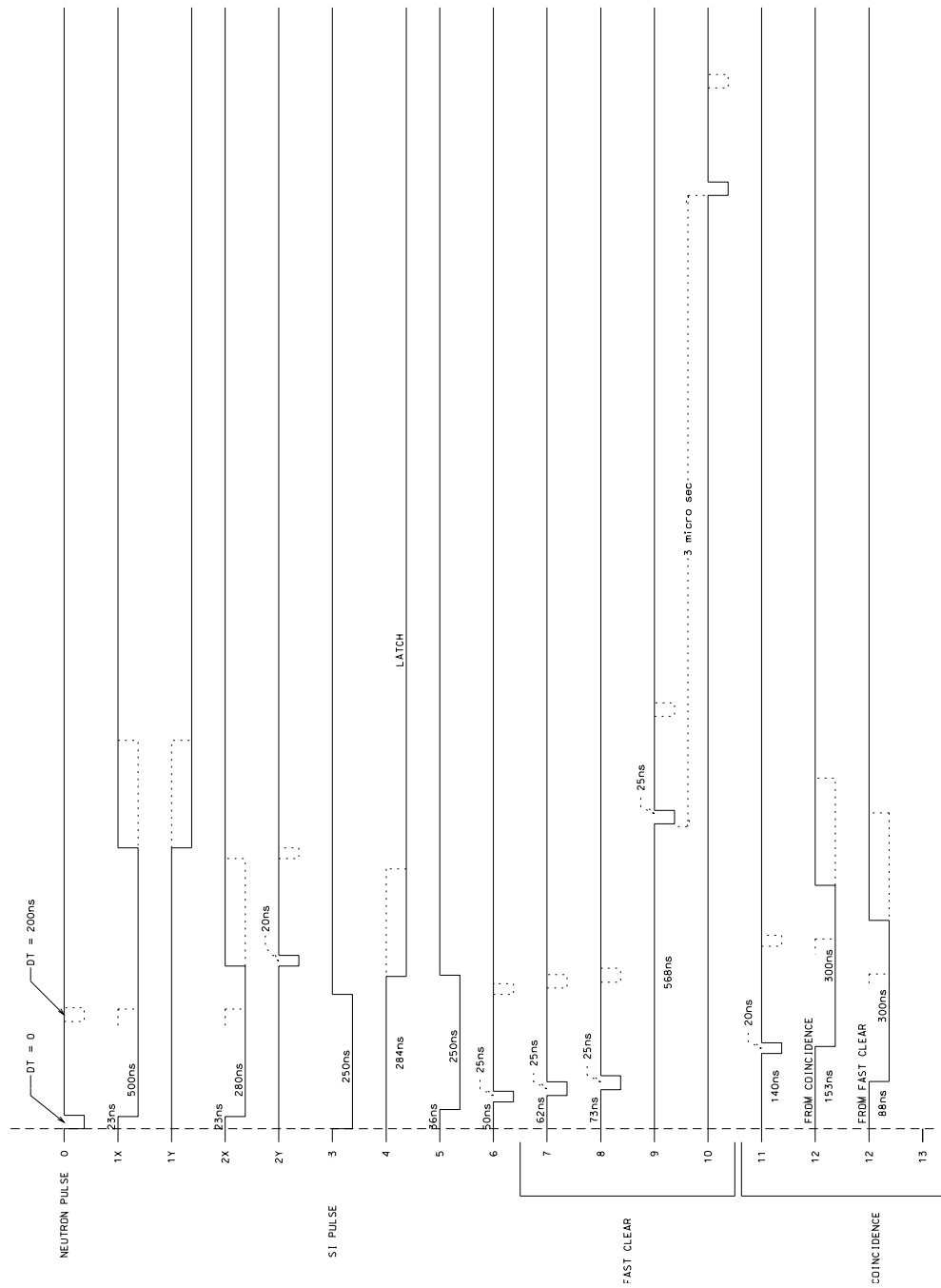


Figure 49 - Timing diagram for the master trigger logic.

9.2 Calibrations

Two particular calibrations must be performed each time the neutron wall is used: a pulse-height to energy calibration, and a time per ADC channel calibration. These calibrations are demonstrated below. Another issue alluded to earlier is the cross-talk analysis when two or more neutrons are to be detected in coincidence. This analysis relies on the pulse-height calibration and is briefly discussed in the last section.

9.2.1 Pulse-Height Calibration

Although TOF is used to determine the neutron's energy, it is often useful to know the energy of the recoil proton. The easiest method to measure the proton's energy is to measure the PMT's pulse height which is proportional to the proton's energy. Unfortunately, the $1/e$ attenuation length of NE-213 is about one and a half meters—comparable to the length of a cell—making the pulse-height value dependent on the distance between the PMT and the scintillation event. In section 2.2 we explain how a position independent pulse-height measurement can be made by taking the square root of the product of the two PMT pulse-heights.

To calibrate the pulse height spectrum we use various γ -ray sources. In the same manner that neutrons are detected through (n,p) scattering, γ -rays are detected through compton scattering. We use three different γ -ray sources for the pulse height calibration: ^{60}Co , ^{228}Th , and $^{12}\text{C}(E_x = 4.44 \text{ MeV})$ in a PuBe source. Figure 50 shows a sample pulse height spectrum for each of the three sources. The energies shown are not the γ -ray energies, but the compton edge energy of the recoil electron. The compton edge energy is associated with the channel of the half-height value of the compton edge. Once the γ -ray calibration is known,

we use an empirical expression relating equivalent light output from recoil protons and recoil electrons.³³ The expression is

$$E_e = a_1 E_p - a_2 \left[1.0 - \exp(-a_3 E_p^{a_4}) \right], \quad (20)$$

where E_e is the electron's kinetic energy, E_p is the proton's kinetic energy, $a_1 = 0.83$, $a_2 = 2.82$, $a_3 = 0.25$, and $a_4 = 0.93$.

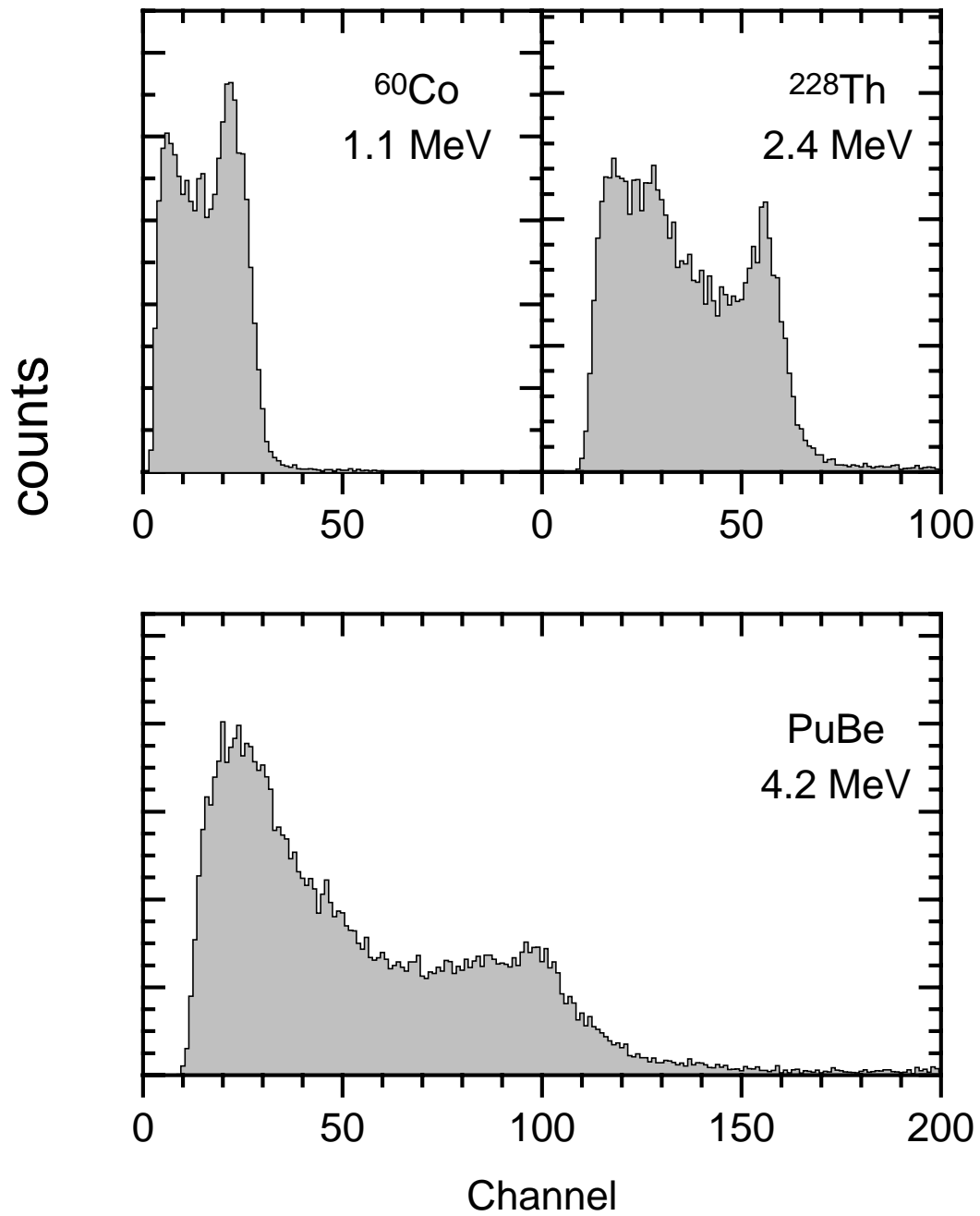


Figure 50 - Sample pulse-height spectra for three different γ -ray sources. The compton edge is used to obtain a calibration of pulse-height to electron equivalent energy. The energies shown are the compton electron energies.

9.2.2 Time Calibrations

It is necessary to calibrate the TFCs used to measure the neutron's TOF. To facilitate the calibration, a fiber optic system has been installed in each array. This system uses an ultraviolet laser to illuminate a bundle of fiber optic cables simultaneously. The bundle is then separated into individual cables that are directed to the center of each cell. The fiber optic cables have been cut to exactly the same length. One extra cable is sent to a small plastic scintillator attached to a fast PMT; this detector provides a constant time reference that is used as the TFC stop signal. (In essence, it replaces the fragment detector used for the TOF measurements). By changing the delay between the reference detector and the input to the TFC's stop, we obtained different peaks in the TFC spectra. One such spectrum is shown in Figure 51, where 5 different laser peaks are present. Knowing the incremental steps added to the delay, we calculate our time-to-channel calibration.

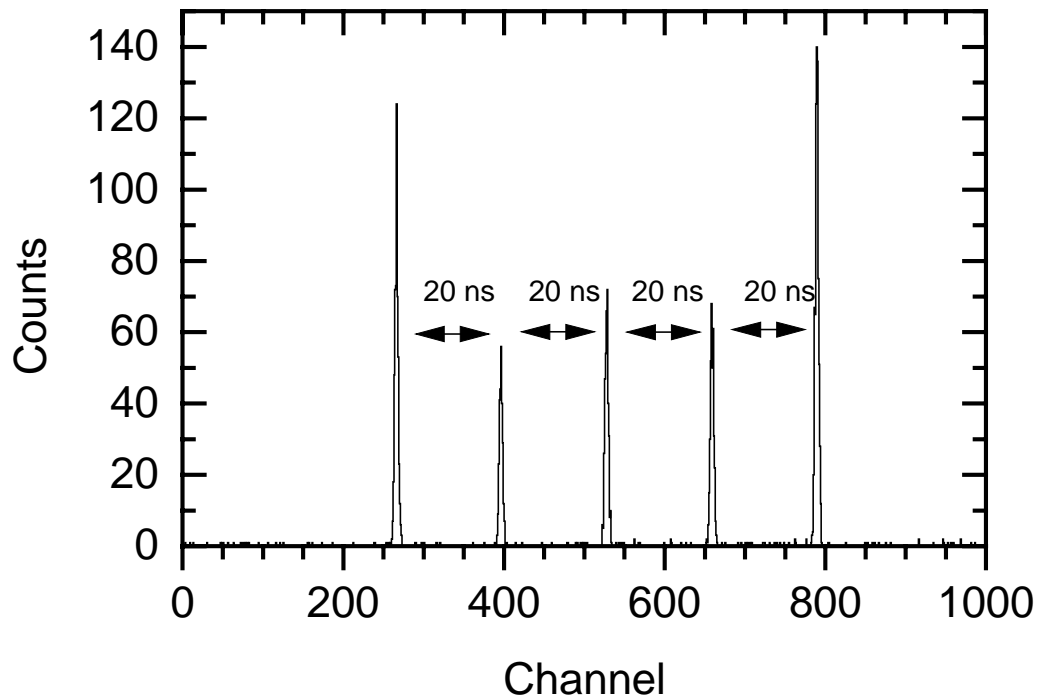


Figure 51 - A laser time calibration for a cell in the *Neutron Wall Array*. The laser pulses are separated by 20 ns.

9.2.3 Cross-Talk

As mentioned earlier, placing a second array behind the first increases the problems of cross-talk and out-scattering. To explain how we attempt to manage these effects, it is useful to look at the main interactions that we can expect between the neutrons and the scintillator material. The scintillator is almost entirely hydrogen and carbon, and Table [reactions] lists the most likely interactions for neutrons in the scintillator. The first two have the largest cross-sections.

Table 5 - Listing of the predominant interactions for a neutron in the scintillator NE-213.

$n + p \rightarrow n + p$
$n + C \rightarrow n + C$
$n + C \rightarrow n' + C - 4.44 \text{ MeV}$
$n + C \rightarrow \text{He} + \text{Be} - 5.71 \text{ MeV}$
$n + C \rightarrow n' + 3\text{He} - 7.26 \text{ MeV}$
$n + C \rightarrow p + B - 12.59 \text{ MeV}$

The (n,p) elastic scattering is the primary source of cross-talk. Figure 52 shows a typical example of a cross talk event. In this scenario a single neutron scatters from a proton in the first wall, making a signal. The neutron does not lose all of its energy and proceeds to the second wall where it scatters from another proton and makes a second signal. To discriminate these events from the real two-neutron events, we subject each two-neutron event to three tests.

1. The light pulse from the first scattered proton implies the proton's energy E_{P1} . From simple kinematics, E_{P1} implies the energy $E_{n'}$ of the scattered neutron and thus the scattering angle θ . If the scattering angle does not correspond to the location of the second pulse, then the event is not cross talk.
2. If the scattered neutron's energy $E_{n'}$, as implied by E_{P1} , does not correspond with the energy as implied by the time-of-flight between the two walls, then the event is not cross-talk.
3. If the second scattered proton's energy E_{P2} is greater than the scattered neutron's energy $E_{n'}$, then the event is not cross-talk.

If the event passes all three test, it may be a cross-talk event. If the first recoil proton P1 does not have sufficient energy to be detected, then the event is no longer considered cross-talk and is considered out-scattering.

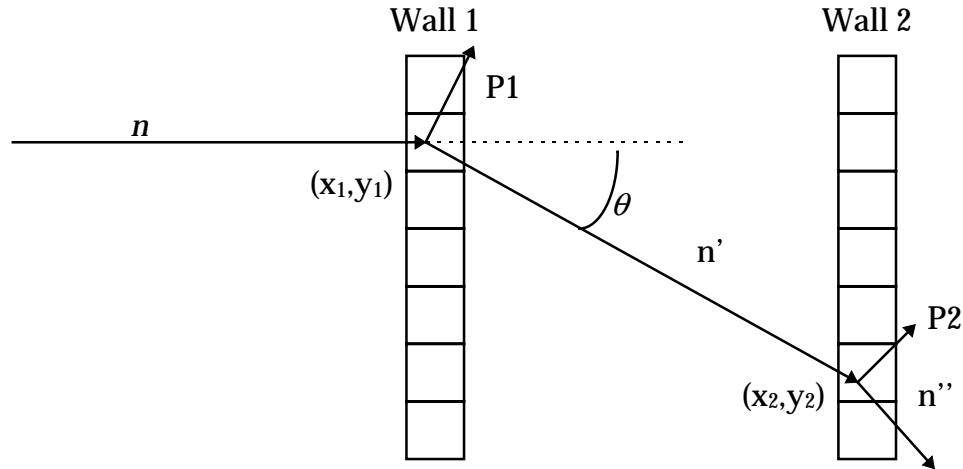


Figure 52 - A typical example of a cross-talk event.

Although most of the recoil protons will be detected, the recoil carbons will be too highly ionizing to ever produce enough light for detection. (as an example, a 40-MeV carbon produces less light than a 1-MeV electron.) Therefore, the carbon in the scintillator effectively becomes non-active material and contributes to out-scattering. There is no way to identify these events, so we must rely on computer modeling to understand the effects. The majority of the out-scattering problem results in a loss of energy and position resolution in the second wall; the results of a monte carlo simulation of two-neutron detection are shown in Figure 53. This simulation assumed one neutron was detected in the first detector wall and the second neutron in the second detector wall; each neutron had an energy of 25 MeV, and the two neutrons had a relative momentum difference of 10 MeV/c. Figure 53 illustrates the effects on the relative momentum measurements caused by the position resolution, the cells' height, and the out-scattering. Although the effects of out-scattering are significant, they are comparable to other intrinsic resolution effects in the detector and thus we feel they are manageable.

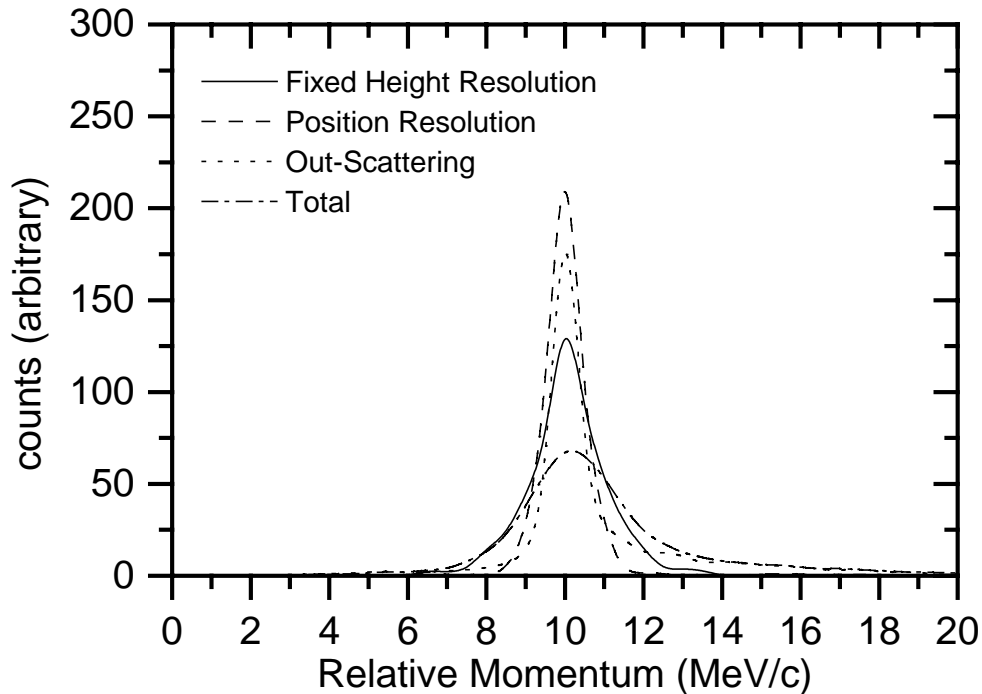


Figure 53 - The results of a monte carlo simulation that models the effects on relative momentum resolution caused by position resolution and out-scattering.

10 The Neutron Wall Array in Recent Experiments

The *Neutron Wall Array* was completed in April of 1995. To test the simulation models developed by Wang *et al.*, we took data from a measurement of the ${}^7\text{Li}(p,n){}^7\text{Be}$ reaction. This reaction was used because it produces only one neutron, whose angular distribution and energy distribution are well known. The simulations model the effects of cross talk and out-scattering, and they can be easily compared to the results from the ${}^7\text{Li}(p,n){}^7\text{Be}$ experiment. A paper describing the model and the results from this experiment are to be published in the near future. In the time since the *Neutron Wall Array* was completed, it has been used in three different experiments; a very brief description of each experiment is given below.

10.1 Measuring the ${}^8\text{Li}(n,\gamma){}^9\text{Li}$ Neutron Capture Cross Section (Zecher et al.)

This first experiment involving the *Neutron Wall Array* was performed at the end of the summer of 1995. This experiment attempted to determine the ${}^8\text{Li}(n,\gamma){}^9\text{Li}$ neutron-capture cross section at astrophysical energies. A direct measurement of this reaction would involve both a radioactive beam and target; therefore, we measured the inverse reaction, ${}^9\text{Li}(\gamma,n){}^8\text{Li}$, where the γ -ray was provided by the coulomb field of a large nucleus. If the inverse reaction is known, it can be related to the reaction of interest by the detailed balance theorem.

This reaction was of astrophysical interest because it plays a crucial role in the formation of $A>12$ isotopes in proposed nucleosynthesis models resulting from an inhomogeneous big bang. The theoretical estimates of the ${}^8\text{Li}(n,\gamma){}^9\text{Li}$ reaction rate varied by greater than an order of magnitude. Unfortunately, we did not have sufficient beam time to determine the neutron-capture cross section, but we were able to set an upper limit to the cross section. This upper limit was consistent with two of the four current theoretical estimates, and seems to rule out two higher estimates. We are submitting a proposal to carry out the experiment again in the near future.

10.2 Two-Neutron Correlations from Heavy Ion Collisions (Gaff et al.)

Following the ${}^8\text{Li}(n,\gamma){}^9\text{Li}$ measurement, the *Neutron Wall Array* was used to measure two-neutron correlation functions from heavy ion collisions. Correlation functions are functions of the relative momentum of two particles emitted from a compound nucleus formed by a central, heavy-ion collision. Two-neutron correlation functions give insight into the space-time extent of the compound nuclei. Similar correlation measurements have been performed using protons,^{34,35,36,37} but some have suggested that the coulomb interaction between

the protons and the residual nucleus will distort the correlation function. By using neutrons, we hope to eliminate this concern. Before this experiment, only a few other attempts had been made to measure two-neutron correlations.^{38,39} Gaff *et al.* expect to improve both the relative momentum resolution and low-momentum threshold of these previous measurements. To date, the analysis of the data from this experiment indicates that the correlation function is very sensitive to cross-talk effects, but it seems possible to correct for the effect.⁴⁰

10.3 Further Halo-Nuclei Structure Experiments (J. Kruse et al., J. Wang et al., Y. Iwata et al.)

Recently, we repeated the $^{11}\text{Li}(\gamma,2n)^9\text{Li}$ experiment that provided the original motivation for constructing the *Neutron Wall Array*. In addition to measuring the coulomb dissociation of ^{11}Li , we also measured the coulomb dissociation of ^6He and ^8He at 25 MeV/nucleon. We are also attempting to apply the same technique that we used in $^8\text{Li}(n,\gamma)^9\text{Li}$ experiment of estimating the nuclear component of the dissociation by measuring the dissociation by targets with a wide range of Z. Apart from using the *Neutron Wall Array* in place of the previous neutron detector array, we have made other substantial improvements to the equipment. In place of the Si-CsI telescope, we now use a C shaped dipole magnet located after the target to sweep the fragments and the unreacted beam away from the *Neutron Wall Array*. This will reduce much of the background created by the unreacted beam in the telescope. The analysis of this experiment has only just begun.

Bibliography

- ¹ R. A. Malaney and G. J. Mathews, *Physics Reports* **229**, 145 (1993).
- ² E. Witten, *Physical Review D* **30**, 272 (1984).
- ³ R. A. Malaney and W. A. Fowler, *Astrophysical Journal* **333**, 14 (1988).
- ⁴ J. H. Applegate, C. J. Hogan, and R. J. Scherrer, *Physical Review D* **35**, 1151 (1987).
- ⁵ R. A. Malaney and W. A. Fowler, in *The Origin and Distribution of the Elements*, edited by G. J. Mathews (Singapore: World Scientific, 1988), p. 76.
- ⁶ G. Baur, C.A. Bertulani and H. Rebel, *Nuclear Physics A***458**, 188 (1986).
- ⁷ R. Sachs, *Nuclear Theory* (Addison-Wesley Publishing Company, Inc., 1953), p. 141.
- ⁸ C. A. Bertulani and G. Baur, *Physics Reports* **163**, 302 (1988).
- ⁹ D. Sackett *et al.*, *Physical Review C* **48**, 118 (1993).
- ¹⁰ T. Motobayashi *et al.*, *Physical Review Letters* **73**, 2680 (1994).
- ¹¹ J. Kiener *et al.*, *Physical Review C* **44**, 2194 (1991).
- ¹² T. Motobayashi *et al.*, *Physics Letters B* **264**, 259 (1991).
- ¹³ L. Heilbronn, A. Galonsky, X. Yang, F. Deák, Á. Kiss, and Z. Seres, *Physical Review C* **40**, 2576 (1989).
- ¹⁴ G. W. Butler, A. M. Poskanzer and D. A. Landis, *Nuclear Instruments and Methods* **89**, 189 (1970).
- ¹⁵ F.S. Goulding, D.A. Landis, J. Cerny and R.H. Pehl, *Nuclear Instruments and Methods* **31**, 1 (1964).
- ¹⁶ P. Bevington, *Data Reduction and Error Analysis for the Physical Sciences* (McGraw-Hill, 1969), p. 56.
- ¹⁷ someone, computer code TOTEFF,

- ¹⁸ C. A. Bertulani and G. Baur, *Physics Reports* **163**, 321 (1988).
- ¹⁹ D. Sackett, Ph.D. dissertation, Michigan State University, 1992.
- ²⁰ F. Ajzenberg-Selove, *Nuclear Physics A***490**, 1 (1988).
- ²¹ Z. Q. Mao and A. E. Champagne, *Nuclear Physics A***522**, 568 (1991).
- ²² P. Descouvemont, *Astrophysical Journal* **405**, 518 (1993).
- ²³ R. A. Malaney and W. A. Fowler, *Astrophysical Journal* **345**, L5 (1989).
- ²⁴ T. Rauscher, J. H. Applegate, J. J. Cowan, F. K. Thielemann, and M. Wiescher, *Astrophysical Journal* **429**, 499 (1994).
- ²⁵ I. Tanihata, H. Hamagaki, O. Hashimoto, Y. Shida, N. Yoshikawa, K. Sugimoto, O. Yamakawa, T. Kobayashi, and N. Takahashi, *Physics Letters* **55**, 2676 (1985).
- ²⁶ G. Knoll, *Radiation Detection and Measurement* (John Wiley & Sons, 1989), chap. 15.
- ²⁷ G. Knoll, *Radiation Detection and Measurement* (John Wiley & Sons, 1989), p. 532.
- ²⁸ C. D. Goodman, J. Rapaport, D. E. Bainum and C. E. Brient, *Nuclear Instruments and Methods* **151**, 125 (1978).
- ²⁹ S. J. Gaff (private communication).
- ³⁰ Kasagi *et al.*,
- ³¹ J. Töke, S. A. Masserant, S. P. Baldwin, B. Lott, W. U. Schröder, and X. Zhao, preprint, 1993.
- ³² D. Carter (private communication).
- ³³ R. A. Cecil, B. D. Anderson, and R. Madey, *Nuclear Instruments and Methods* **161**, 439 (1979).
- ³⁴ W. G. Gong *et al.*, *Physical Review C* **43**, 1804 (1991).
- ³⁵ M.A. Lisa *et al.*, *Physical Review Letters*, **70**, 3709 (1993).
- ³⁶ D. O. Handzy *et al.*, *Physical Review Letters*, **75**, 2916 (1995).
- ³⁷ S. J. Gaff *et al.*, *Physical Review C*, **52**, 2782 (1995).

³⁸ B. Jakobsson *et al.*, Physical Review C, **44**, R1238 (1991).

³⁹ N. Colonna *et al.*, Physical Review Letters, **75**, 4190 (1995).

⁴⁰ S. J. Gaff (private communication).